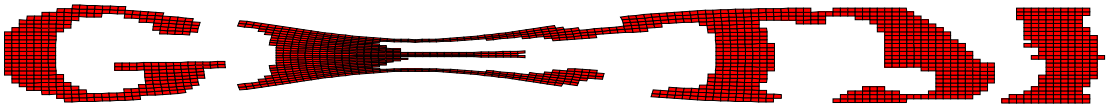

GETM

A General Estuarine Transport Model

Scientific Documentation

Hans Burchard and Karsten Bolding

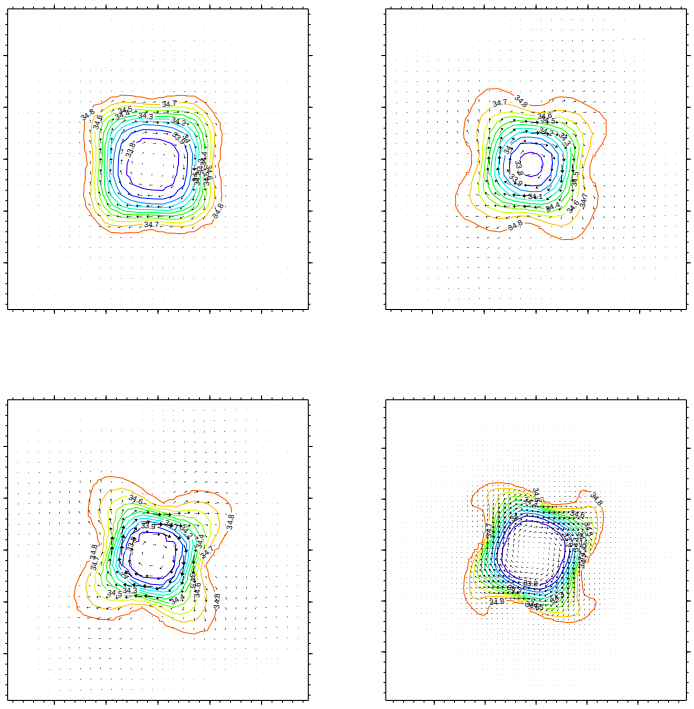

Contents

Chapter 1

Introduction

1.1 GOTM and GETM

It is now about 3 years ago that the General Ocean Turbulence Model GOTM has been published as a Public Domain water column model by *Burchard et al.* [1999]. Since then, a full access to the model source code, numerous data for forcing and validating test cases and extensive scientific and technical documentation is provided through the GOTM home page in the World Wide Web at `http://www.gotm.net`. The physical part of GOTM has been more and more extended such that now a wide range of turbulence parameterisations can be compared in one and the same model environment. During these years, GOTM became a popular water column model all around the world with more than 100 subscribed users. We do strongly believe that this acknowledgement of GOTM as a widespread and well-tested model is a direct consequence of its status as a Public Domain software tool.

A short time after GOTM was published, colleagues started to ask us, whether we had any intentions to extend GOTM towards a three-dimensional model. Their arguments were that a one-dimensional water column model is a nice tool for local boundary layer studies, but the predictability for full-scale (i.e. three-dimensional problems) would be limited. Furthermore, the transfer of new parameterisations in GOTM to three-dimensional models would not be straight-forward, and would require further testing and validation. Our main argument against extending GOTM towards a three-dimensional model was, that people generally have their favourite ocean model and would not move to another model just for having access to a greater choice of turbulence parameterisations. In this situation, the idea was born (and we are grateful to Georg Umgiesser from Venice, Italy for this suggestion) to isolate the turbulence module inside GOTM from the rest of the program in such a way that it can be either called from the basic GOTM model or, through an interface,

from any three-dimensional circulation model. Today, such interfaces exist for the Modular Ocean Model (MOM, Princeton University, New Jersey, interface provided by Encho Demirov, Bologna, Italy), MOHID (Instituto Superior Tecnico, Lisboa, Portugal, interface provided by Manuel Ruiz Villarreal, Hamburg, Germany), and ... GETM (General Estuarine Transport Model), which is the subject of this report. For a short history of GETM, see section 1.2.

Instead of extending GOTM to a three-dimensional model, a prototype three-dimensional model, GETM, has been constructed around GOTM. The authors of this report who made GOTM and GETM, have however been infected by the idea of Public Domain models. Thus, it was clear that the same philosophy as for GOTM would be followed for GETM. This is not least expressed in the model's acronyms sounding similar. The authors are fully aware of the problems additionally posed by a three-dimensional model in comparison to a one-dimensional model. Since a one-dimensional model is in fact two-dimensional (considering time as a dimension) and a three-dimensional model has four dimensions, we expect that all efforts to maintain GETM as a Public Domain tool will be squared in comparison to GOTM. We would thus be happy, if our future users would have the square of the patience they had with GOTM and the square root of the expectations towards us concerning scientific and technical support.

1.2 A short history of GETM

The idea for GETM was born in May 1997 in Arcachon, France during a workshop of the PhaSE project which was sponsored by the European Community in the framework of the MAST-III programme. It was planned to set up an idealised numerical model for the Eastern Scheldt, The Netherlands for simulating the effect of vertical mixing of nutrients on filter feeder growth rates. A discussion between the first author of this report, Peter Herman (NIOO, Yerseke, The Netherlands) and Walter Eifler (JRC Ispra, Italy) had the result that the associated processes were inherently three-dimensional (in space), and thus, only a three-dimensional model could give satisfying answers. Now the question arose, which numerical model to use. An old wadden sea model by *Burchard* [1995] including a two-equation turbulence model was written in z-coordinates with fixed geopotential layers (which could be added or removed for rising and sinking sea surface elevation, respectively) had proven to be too noisy for the applications in mind. Furthermore, the step-like bottom approximation typical for such models did not seem to be sufficient. Other Public Domain models did not allow for drying and flooding of inter-tidal flats, such as the Princeton Ocean Model (POM). There was thus the need for a new model.

Most of the ingredients were however already there. The first author of this report had already written a k-ε turbulence model, see *Burchard and Baumert* [1995], the forerunner of GOTM. A two-dimensional code for general vertical coordinates had been written as well, see *Burchard and Petersen* [1997]. And the first author of this report had already learned a lot about mode splitting models from Jean-Marie Beckers (University of Liege, Belgium). Back from Arcachon in Ispra, Italy at the Joint Research Centre of the European Community, the model was basically written during six weeks, after which an idealised tidal simulation for the Sylt-Rømø Bight in the wadden sea area between Germany and Denmark could be successfully simulated, see *Burchard* [1998] and also section 6.1 of this report. By that time this model had the little attractive name *MUDFLAT* which at least well accounted for the models ability to dry and flood inter-tidal flats. At the end of the PhaSE project in 1999, the idealised simulation of mussel growth in the Eastern Scheldt could be finished (not yet published, pers. comm. Francois Lamy and Peter Herman).

In May 1998 the second author of this report joined the development of *MUDFLAT*. He first fully rewrote the model from a one-file FORTRAN77 code to a modular FORTRAN90/95 code, made the interface to GOTM (such that the original k-ε model was not used any more), integrated the netCDF-library into the model, and prepared the parallelisation of the model. And a new name was created, GETM, General Estuarine Transport Model. As already in GOTM, the word "General" does not imply that the model is general, but indicates the motivation to make it more and more general.

At that time, GETM has actually been applied for simulating currents inside the Mururoa atoll in the Pacific Ocean, see *Mathieu et al.* [2001].

During the year 2001, GETM was then extended by the authors of this report to be a fully baroclinic model with transport of active and passive tracers, calculation of density, internal pressure gradient and stratification, surface heat and momentum fluxes and so forth. During a stay of the first author at the Université Catholique de Louvain, Institut d'Astronomie et de Géophysique George Lemaître, Belgium (we are grateful to Eric Deleersnijder for this invitation and many discussions) the high-order advection schemes have been written. During another invitation to Belgium, this time to the GHER at the Université de Liège, the first author had the opportunity to discuss numerical details of GETM with Jean-Marie Beckers, who originally motivated us to use the mode splitting technique.

The typical challenging application in mind of the authors was always a simulation of the tidal Elbe, where baroclinicity and drying and flooding of inter-tidal flats play an important role. Furthermore, the tidal Elbe is long, narrow and bended, such that the use of Cartesian coordinates would require an indexing of the horizontal fields, see e.g. *Duwe* [1988]. Thus, the use of curvi-linear coordinates which follow

the course of the river has already been considered for a long time. However, the extensions just listed above, give the model also the ability to simulate shelf sea processes in fully baroclinic mode, such that the name General Estuarine Transport Model is already a bit too restrictive.
The present report is documenting the physical and numerical status of GETM in early 2002.

1.3 List of characteristic GETM features

In the following, a short list of some characteristic GETM features is given:

- **Physics**
  - 3D primitive equations for u, v, T, S, C
  - Hydrostatic approximation
  - Free surface
  - Boussinesq approximation
  - Drying and flooding, simplyfied physics over mudflats
  - Eddy viscosity assumption
  - Turbulence closure models from GOTM:
    - Zero-, one- and two-equation models
    - Various algebraic second-moment closures
    - Some simple internal wave parameterisations
- **Transformations**
  - General vertical coordinates
  - Orthogonal curvilinear coordinates in horizontal plain
- **Numerics**
  - Finite-volume, finite-difference discretisation on C-grid
  - Mode splitting into barotropic and baroclinic mode
  - Directional-split advection with high-order TVD schemes
  - Various internal pressure gradient formulations
  - Quadratic bed friction

- **Computing**
  - Code written in FORTRAN 90/95
  - Modular code structure
  - Code prepared for parallel computing
  - Input/Output in netCDF format
  - PROTEX source code documentation
- **Miscellaneous**
  - Public Domain model published under GNU Public Licence

In the following table, some major characteristics of a number of numerical models are compared:

	Vertical discretisation	Horizontal discretisation	Barotropic time-stepping	High-order turbulence closures	Drying/Flooding	Public Domain
POM	s	CU	MSP	Y	N	Y
MOM	z	CA	MSP	Y	N	Y
HAMSOM	z	CA	IMP	N	N	Y
MOHID	s	CA	ADI	Y	Y	Y
SCRUM	s	CU	MSP	Y	N	Y
POL3DB	s	CA	MSP	Y	N	Y
GHER-M	σ	CA	MSP	Y	N	Y
COHERENS	σ	CA	MSP	Y	N	Y
TRIM-3D	z	CA	IMP	N	Y	N
MIKE-3	z	CA	ADI	Y	N	N
TELEMAC-3D	σ	FE	IMP	Y	Y	N
ECOM	s	CU	IMP	Y	Y	N
TRIWAQ	s	CU	ADI	Y	Y	N
GETM	s	CU	MSP	Y	Y	Y

where the following abbreviations have been used:
CU: curvi-linear;
CA: Cartesian;
FE: Finite elements
MSP: mode splitting;
ADI: alternate directions implicit;
IMP: implicit
The model acronyms have the following meanings:
POM: Princeton Ocean Model, Princeton University, Princeton, New Jersey, see *Blumberg and Mellor* [1987]; **MOM**: Modular Ocean Model, Geophysical Fluid Dynamics Laboratory, Princeton, New Jersey, see *Bryan* [1969], *Cox* [1984] and *Rosati and Miyakoda* [1988]; **HAMSOM**: Hamburg Shelf and Ocean Model, Institute for Oceanography, University of Hamburg, Germany, see *Backhaus* [1985] and *Pohlmann* [1996]; **MOHID**: Modelo Hidrodinámico, MARETEC group, Instituto Superior Tecnico, Universidade Tecnica de Lisboa, Portugal, see *Martins et al.* [1998]; **SCRUM**: S-coordinate Rudgers University Model, Rutgers University, New Jersey, see *Song and Haidvogel* [1994]; **POL3DB**: Proudman Oceanographic Laboratory Three-Dimensional B grid model, Birkenhead, United Kingdom, see *Holt and James* [2001]; **GHER-M**: the GeoHydrodynamics and Environment Research Laboratory Model, University of Liège, Belgium, see *Beckers* [1995]; **COHERENS**: Coupled hydrodynamical-ecological model for regional and shelf seas, European Commission, see *Luyten et al.* [1999]; **TRIM-3D**: Universitá degli Studi di Trento, see *Casulli and Cheng* [1992]; **MIKE-3**: Danish Hydraulic Institute, Hørsholm, Denmark, see `http://www.dhisoftware.com`; **TELEMAC-3D**: Laboratoire National d'Hydraulique, Electricité de France; **ECOM**: HydroQual, see `http://www.hydroqual.com/Models/models.htm`; **TRIWAQ**: Rijkswaterstraat, The Hague, The Netherlands, see *Lander et al.* [1994].
From the above comparison, it can be concluded that MOHID and GETM are the only three-dimensional Public Domain Models with high-order turbulence closures and drying and flooding of intertidal flats.

1.4 Summary and structure of this report

This report is structured as follows:
First, in chapter 2, the physical equations for momentum and tracers are given in Cartesian coordinate notation. It is shown, how the drying and flooding is accounted for already on this level of modelling. Lateral and vertical boundary conditions are given. Furthermore, the physical link to the turbulence models from GOTM is explained. The latter is the most characteristic physical difference to many other

ocean models, which are generally equipped with a smaller choice of turbulence parameterisations.

In chapter 3, the discretisation is prepared by introducing general vertical coordinates. Based on this, the layer-integrated equations are derived. Furthermore, the curvi-linear orthogonal transformation is carried out, of which Cartesian coordinates and spherical coordinates are special cases. These two features, general vertical coordinates and curvi-linear coordinates, have recently been implemented into several other ocean models (e.g. the Princeton Ocean Model (POM) works with general vertical coordinates since recently and with curvi-linear coordinates since many years, and the S-Coordinate Rutgers University Model (SCRUM) is built up upon these two features).

In the most extensive chapter 4, the discretisation of the layer-integrated model equations is discussed in detail. In contrast to the physical formulation of the equations, the layer-integration and the numerics do strongly discriminate between various three-dimensional ocean models. The characteristic numerical features of GETM are the mode splitting, the high-order advection schemes (which can also be applied to momentum and in the near future also to turbulent quantities) and the treatment of drying and flooding of inter-tidal flats. For some terms, a choice among several discretisation methods is given, such as for the Coriolis rotation, the internal pressure gradient and the advection algorithms.

In sections 5 and 6, a number of idealised and realistic applications are given. First (section 5.1), the advantages of the curvi-linear coordinates in comparison to the Cartesian coordinates are shown by means of simple, vertically integrated steady-state simulations of flow through bended and constricted channels. Then (section 5.2), the classical two-dimensional friction-less lock exchange experiment is carried out with several advection schemes. Furthermore (section 5.3), an estuarine test case is presented by Manuel Ruiz Villarreal (Institute for Oceanography, University of Hamburg, Germany). In this two-dimensional simulation in the xz domain, a saltwedge moves back and forth with the tide and induces an estuarine turbidity maximum at the tip of the saltwedge. Finally (section 5.4), the three-dimensional so-called NOMADS freshwater eddy case is simulated. In this test case, the development of baroclinic instabilities is shown for various momentum and tracer advection schemes and two-different spatial resolutions.

As realistic applications, tidal currents in the wadden sea area of the Sylt-Rømø Bight between Denmark and Germany, wind-driven circulation in Lake Constance, Germany, and the dynamics of the North Sea are simulated. The wadden sea simulation (see section 6.1) is the classical test case with the aid of which already the forerunner of GETM, MUDFLAT has been developed. Here, currents and turbulence for two different discretisations of the momentum advection terms are shown

as surface plots, Hovmueller diagrams (t-s plots) and cross-sections. The Lake Constance simulation (see section 6.2) has been carried out for demonstrating the models ability to reproduce currents and stratification with general vertical coordinates over steep bathymetry. We would like to acknowledge Lars Umlauf (EPFL, Lausanne, Switzerland) for suggesting this test case and providing the bathymetry. Finally, the North Sea simulation (see section 6.3) shows the ability of GETM to carry out numerically stable simulations with reasonable results also for larger domains such as shelf seas. The presented annual simulation is fully baroclinic with prognostic temperature and salinity calculation under consideration of tidal forcing.
Finally, a list of all symbols used in this report are listed in the appendix (chapter 7) and the references are given.

Chapter 2

Physics

2.1 Hydrodynamic equations

2.1.1 Three-dimensional momentum equations

For geophysical coastal sea and ocean dynamics, usually the three-dimensional hydrostatic equations of motion with the Boussinesq approximation and the eddy viscosity assumption are used (*Bryan* [1969], *Cox* [1984], *Blumberg and Mellor* [1987], *Haidvogel and Beckmann* [1999], *Kantha and Clayson* [2000b]). In the flux form, the dynamic equations of motion for the horizontal velocity components can be written in Cartesian coordinates as:

$$\begin{aligned}
&\partial_t u + \partial_z(uw) - \partial_z\left((\nu_t+\nu)\partial_z u\right) \\
&\quad +\alpha\Big(\partial_x(u^2) + \partial_y(uv) - \partial_x\left(2A_h^M\partial_x u\right) - \partial_y\left(A_h^M(\partial_y u + \partial_x v)\right) \\
&\quad -fv - \int_z^\zeta \partial_x b\, dz'\Big) = -g\partial_x\zeta,
\end{aligned} \tag{2.1}$$

$$\begin{aligned}
&\partial_t v + \partial_z(vw) - \partial_z\left((\nu_t+\nu)\partial_z v\right) \\
&\quad +\alpha\Big(\partial_x(vu) + \partial_y(v^2) - \partial_y\left(2A_h^M\partial_y v\right) - \partial_x\left(A_h^M(\partial_y u + \partial_x v)\right) \\
&\quad +fu - \int_z^\zeta \partial_x b\, dz'\Big) = -g\partial_y\zeta.
\end{aligned} \tag{2.2}$$

The vertical velocity equation reduces to the so-called continuity equation:

$$\partial_x u + \partial_y v + \partial_z w = 0. \tag{2.3}$$

Here, u, v and w are the ensemble averaged velocity components with respect to the x, y and z direction, respectively. The vertical coordinate z ranges from the bottom $-H(x,y)$ to the surface $\zeta(t,x,y)$ with t denoting time. ν_t is the vertical eddy viscosity, ν the kinematic viscosity, f the Coriolis parameter, and g is the gravitational acceleration. The horizontal mixing is parameterised by terms containing the horizontal eddy viscosity A_h^M, see *Blumberg and Mellor* [1987]. The buoyancy b is defined as

$$b = -g\frac{\rho - \rho_0}{\rho_0} \tag{2.4}$$

with the density ρ and a reference density ρ_0. The last term on the left hand sides of equations (2.1) and (2.2) are the internal (due to density gradients) and the terms on the right hand sides are the external (due to surface slopes) pressure gradients. In the latter, the deviation of surface density from reference density is neglected (see *Burchard and Petersen* [1997]). The derivation of equations (2.1) - (2.3) has been shown in numerous publications, see e.g. *Pedlosky* [1987], *Haidvogel and Beckmann* [1999], *Burchard* [2001c].
In hydrostatic 3D models, the vertical velocity is calculated by means of equation (2.3) velocity equation. Due to this, mass conservation and free surface elevation can easily be obtained.
Drying and flooding of mud-flats is already incorporated in the physical equations by multiplying some terms with the non-dimensional number α which equals unity in regions where a critical water depth D_{crit} is exceeded and approaches zero when the water depth D tends to a minimum value D_{min}:

$$\alpha = \min\left\{1, \frac{D - D_{min}}{D_{crit} - D_{min}}\right\}. \tag{2.5}$$

Thus, $\alpha = 1$ for $D \geq D_{crit}$, such that the usual momentum equation results except for very shallow water, where simplified physics are considered with a balance between tendency, friction and external pressure gradient. In a typical wadden sea application, D_{crit} is of the order of 0.1 m and $D_{\min}$ of the order of 0.02 m (see *Burchard* [1998]).

2.1.2 Kinematic boundary conditions and surface elevation equation

At the surface and at the bottom, kinematic boundary conditions result from the requirement that the particles at the boundaries are moving along these boundaries:

$$w = \partial_t \zeta + u\partial_x \zeta + v\partial_y \zeta \qquad \text{for } z = \zeta, \tag{2.6}$$

$$w = -u\partial_x H - v\partial_y H \qquad \text{for } z = -H. \tag{2.7}$$

2.1.3 Dynamic boundary conditions

At the bottom boundaries, no-slip conditions are prescribed for the horizontal velocity components:

$$u = 0, \quad v = 0. \tag{2.8}$$

With (2.7), also $w = 0$ holds at the bottom. It should be noted already here, that the bottom boundary condition (2.8) is generally not directly used in numerical ocean models, since the near-bottom values of the horizontal velocity components are not located at the bed, but half a grid box above it. Instead, a logarithmic velocity profile is assumed in the bottom layer, leading to a quadratic friction law, see section 4.5.
At the surface, the dynamic boundary conditions read:

$$\begin{aligned} (\nu_t + \nu)\partial_z u &= \alpha \tau_s^x, \\ (\nu_t + \nu)\partial_z v &= \alpha \tau_s^y, \end{aligned} \tag{2.9}$$

The surface stresses (normalised by the reference density) τ_s^x and τ_s^y are calculated as functions of wind speed, wind direction, surface roughness etc. Also here, the drying parameter α is included in order to provide an easy handling of drying and flooding.

2.1.4 Lateral boundary conditions

Let G denote the lateral boundary of the model domain with the closed land boundary G^c and the open boundary G^o such that $G^c \cup G^o = G$ and $G^c \cap G^o = \emptyset$. Let further $\vec{u} = (u, v)$ denote the horizontal velocity vector and $\vec{u}_n = (-v, u)$ its normal vector. At closed boundaries, the flow must be parallel to the boundary:

$$\vec{u}_n \cdot \vec{\nabla} G^c = 0 \tag{2.10}$$

with $\vec{\nabla} = (\partial_x, \partial_y)$ being the gradient operator.
For an eastern or a western closed boundary with $\vec{\nabla} G^c = (0, 1)$ this has the consequence that $u = 0$ and, equivalently, for a southern or a northern closed boundary with $\vec{\nabla} G^c = (1, 0)$ this has the consequence that $v = 0$.
At open boundaries, the velocity gradients across the boundary vanish:

$$\vec{\nabla}_n u \cdot \vec{\nabla} G^o = 0, \quad \vec{\nabla}_n v \cdot \vec{\nabla} G^o = 0, \tag{2.11}$$

with $\vec{\nabla}_n = (-\partial_y, \partial_x)$ being the operator normal to the gradient operator.
For an eastern or a western open boundary with this has the consequence that $\partial_x u = \partial_x v = 0$ and, equivalently, for a southern or a northern open boundary this has the consequence that $\partial_y u = \partial_y v = 0$.
At so-called forced open boundaries, the sea surface elevation ζ is prescribed. At passive open boundaries, it is assumed that the curvature of the surface elevation normal to the boundary is zero, with the consequence that the spatial derivatives of the surface slopes normal to the boundaries vanish.

2.1.5 Vertically integrated mode

In order to provide the splitting of the model into an internal and an external mode, the continuity equation and the momentum equations are vertically integrated. The vertical integral of the continuity equation together with the kinematic boundary conditions (2.6) and (2.7) gives the sea surface elevation equation:

$$\partial_t \zeta = -\partial_x U - \partial_y V. \tag{2.12}$$

with

$$U = \int_{-H}^{\zeta} u\, dz, \qquad V = \int_{-H}^{\zeta} v\, dz. \tag{2.13}$$

Integrating the momentum equations (2.1) and (2.2) vertically results in:

$$\begin{aligned} &\partial_t U + \tau_b^x + \alpha \Bigg(\int_{-H}^{\zeta} \left(\partial_x u^2 + \partial_y (uv) \right) dz \\ &-\tau_s^x - \int_{-H}^{\zeta} \left(\partial_x \left(2A_h^M \partial_x u \right) - \partial_y \left(A_h^M (\partial_y u + \partial_x v) \right) \right) dz \\ &-fV - \int_{-H}^{\zeta} \int_{z}^{\zeta} \partial_x b \, dz' \, dz \Bigg) = -gD\partial_x \zeta \end{aligned} \tag{2.14}$$

and

$$\begin{aligned} &\partial_t V + \tau_b^y + \alpha \Bigg(\int_{-H}^{\zeta} \left(\partial_x (uv) + \partial_y v^2 \right) \right) dz \\ &-\tau_s^y - \int_{-H}^{\zeta} \left(\partial_y \left(2A_h^M \partial_y v \right) - \partial_x \left(A_h^M (\partial_y u + \partial_x v) \right) \right) dz \\ &+fU - \int_{-H}^{\zeta} \int_{z}^{\zeta} \partial_y b \, dz' \, dz \Bigg) = -gD\partial_y \zeta. \end{aligned} \tag{2.15}$$

Here, τ_b^x and τ_b^y are bottom stresses. Their calculation is discussed in section 4.5. As a first preparation for the mode splitting, these integrals of the momentum equations can be formally rewritten as

$$\begin{aligned} &\partial_t U + \frac{R}{D^2} U \sqrt{U^2 + V^2} + S_F^x + \alpha \Bigg(\partial_x \left(\frac{U^2}{D} \right) + \partial_y \left(\frac{UV}{D} \right) \\ &-\tau_s^x - \partial_x \left(2A_h^M D \partial_x \left(\frac{U}{D} \right) \right) - \partial_y \left(A_h^M D \left(\partial_y \left(\frac{U}{D} \right) + \partial_x \left(\frac{V}{D} \right) \right) \right) \\ &-fV + S_A^x - S_D^x + S_B^x \Bigg) = -gD\partial_x \zeta \end{aligned} \tag{2.16}$$

and

$$\partial_t V + \frac{R}{D^2} V\sqrt{U^2+V^2} + S_F^y + \alpha\Bigg(\partial_x \frac{UV}{D} + \partial_y \frac{V^2}{D} - \tau_s^y - \partial_y\left(2A_h^M D\partial_y\left(\frac{V}{D}\right)\right) - \partial_x\left(A_h^M D\left(\partial_y\left(\frac{U}{D}\right) + \partial_x\left(\frac{V}{D}\right)\right)\right) + fU + S_A^y - S_D^y + S_B^y\Bigg) = -gD\partial_y\zeta \tag{2.17}$$

with the so-called slow terms for bottom friction

$$S_F^x = \tau_b^x - \frac{R}{D^2} U\sqrt{U^2+V^2}, \tag{2.18}$$

$$S_F^y = \tau_b^y - \frac{R}{D^2} V\sqrt{U^2+V^2}, \tag{2.19}$$

horizontal advection

$$S_A^x = \int_{-H}^{\zeta} \left(\partial_x u^2 + \partial_y(uv)\right)\, dz - \partial_x\left(\frac{U^2}{D}\right) - \partial_y\left(\frac{UV}{D}\right), \tag{2.20}$$

$$S_A^y = \int_{-H}^{\zeta} \left(\partial_x(uv) + \partial_y v^2\right)\, dz - \partial_x\left(\frac{UV}{D}\right) - \partial_y\left(fracV^2D\right), \tag{2.21}$$

horizontal diffusion

$$S_D^x = \int_{-H}^{\zeta} \left(\partial_x\left(2A_h^M\partial_x u\right) - \partial_y\left(A_h^M(\partial_y u + \partial_x v)\right)\right) dz - \partial_x\left(2A_h^M D\partial_x\left(\frac{U}{D}\right)\right) - \partial_y\left(A_h^M D\left(\partial_y\left(\frac{U}{D}\right) + \partial_x\left(\frac{V}{D}\right)\right)\right), \tag{2.22}$$

$$
\begin{aligned}
S_D^y = &\int_{-H}^{\zeta} \left(\partial_y \left(2A_h^M \partial_y v \right) - \partial_x \left(A_h^M (\partial_y u + \partial_x v) \right) \right) dz \\
&-\partial_y \left(2A_h^M D \partial_y \left(\frac{V}{D} \right) \right) - \partial_x \left(A_h^M D \left(\partial_y \left(\frac{U}{D} \right) + \partial_x \left(\frac{V}{D} \right) \right) \right),
\end{aligned}
\tag{2.23}
$$

and internal pressure gradients

$$
S_B^x = -\int_{-H}^{\zeta} \int_{z}^{\zeta} \partial_x b \, dz' \, dz \tag{2.24}
$$

and

$$
S_B^y = -\int_{-H}^{\zeta} \int_{z}^{\zeta} \partial_y b \, dz' \, dz. \tag{2.25}
$$

The drag coefficient R for the external mode is calculated as (this logarithmic dependence of the bottom drag from the water depth and the bottom roughness parameter z_b^0 is motivated in section 4.5):

$$
R = \left(\frac{\kappa}{\ln \left(\frac{\frac{D}{2} + z_0^b}{z_0^b} \right)} \right)^2. \tag{2.26}
$$

2.2 Tracer equations

The conservation equations for tracers c^i with $1 \leq i \leq N_c$ (with N_c being the number of tracers), which can e.g. be temperature, salinity, nutrients, phytoplankton, zooplankton, suspended matter, chemical concentrations etc. is given as:

$$
\begin{aligned}
&\partial_t c^i + \partial_x (u c^i) + \partial_y (v c^i) + \partial_z ((w + w_s^i) c^i) - \partial_z (\nu_t' \partial_z c^i) \\
&-\partial_x (A_h^T \partial_x c^i) - \partial_y (A_h^T \partial_y c^i) = Q^i.
\end{aligned}
\tag{2.27}
$$

Here, ν_t' denotes the vertical eddy diffusivity and A_h^T the horizontal diffusivity. Vertical migration of concentration with migration velocity w_s^i (positive for upward

motion) is considered as well. This could be i.e. settling of suspended matter or active migration of phytoplankton. Q^i denotes all internal sources and sinks of the tracer c^i. This might e.g. be for the temperature equation the heating of water due to absorption of solar radiation in the water column.
The coupling between the concentration equation and the momentum equations is due to an algebraic equation of state:

$$\rho = \rho(c^1, c^2, \ldots, c^N, p_0) \tag{2.28}$$

with $p_0 = g\rho_0(\zeta - z)$ being the hydrostatic reference pressure.
Surface of bottom boundary conditions for tracers are usually given by prescribed fluxes:

$$\nu_t' \partial_z c^i = F_s^i \qquad \text{for } z = \zeta \tag{2.29}$$

and

$$\nu_t' \partial_z c^i = -F_b^i \qquad \text{for } z = -H, \tag{2.30}$$

with surface and bottom fluxes F_s^n and F_b^n directed into the domain, respectively.
At open lateral boundaries, the tracers c^n are prescribed for the horizontal velocity normal to the open boundary flowing into the domain. In case of outflow, a zero-gradient condition is used.
The two most important tracer equations which are hard-coded in GETM are the transport equations for potential temperature T in °C and salinity S in psu (practical salinity units):

$$\begin{aligned} &\partial_t T + \partial_x(uT) + \partial_y(vT) + \partial_z(wT) - \partial_z(\nu_t' \partial_z T) \\ &\quad -\partial_x(A_h^T \partial_x T) - \partial_y(A_h^T \partial_y T) = \frac{\partial_z I}{c_p' \rho_0}, \end{aligned} \tag{2.31}$$

$$\begin{aligned} &\partial_t S + \partial_x(uS) + \partial_y(vS) + \partial_z(wS) - \partial_z(\nu_t' \partial_z S) \\ &\quad -\partial_x(A_h^T \partial_x S) - \partial_y(A_h^T \partial_y S) = 0. \end{aligned} \tag{2.32}$$

On the right hand side of the temperature equation (2.31) is a source term for absorption of solar radiation with the solar radiation at depth z, I, and the specific heat capacity of water, c'_p. According to *Paulson and Simpson* [1977] the radiation I in the upper water column may be parameterised by

$$I(z) = I_0 \left(a e^{-\eta_1 z} + (1-a) e^{-\eta_2 z} \right). \tag{2.33}$$

Here, I_0 is the albedo corrected radiation normal to the sea surface. The weighting parameter a and the attenuation lengths for the longer and the shorter fraction of the short-wave radiation, η_1 and η_2, respectively, depend on the turbidity of the water. *Jerlov* [1968] defined 6 different classes of water from which *Paulson and Simpson* [1977] calculated weighting parameter a and attenuation coefficients η_1 and η_2.
At the surface, flux boundary conditions for T and S have to be prescribed. For the potential temperature, it is of the following form:

$$\nu'_t \partial_z T = \frac{Q_s + Q_l + Q_b}{c'_p \rho_0}, \qquad \text{for } z = \zeta, \tag{2.34}$$

with the sensible heat flux, Q_s, the latent heat flux, Q_l and the long wave back radiation, Q_b. Here, the *Kondo* [1975] bulk formulae have been used for calculating the momentum and temperature surface fluxes due to air-sea interactions. In the presence of sea ice, these air-sea fluxes have to be considerably changed, see e.g. *Kantha and Clayson* [2000b]. Since there is no sea-ice model coupled to GETM presently, the surface heat flux is limited to positive values, when the sea surface temperature T_s reaches the freezing point

$$T_f = -0.0575\, S_s + 1.710523 \cdot 10^{-3}\, S_s^{1.5} - 2.154996 \cdot 10^{-4}\, S_s^2 \approx -0.0575\, S_s \tag{2.35}$$

with the sea surface salinity S_s, see e.g. *Kantha and Clayson* [2000a]:

$$Q_{surf} = \begin{cases} Q_s + Q_l + Q_b, & \text{for } T_s > T_f, \\ \max\{0, Q_s + Q_l + Q_b\}, & \text{else.} \end{cases} \tag{2.36}$$

For the surface freshwater flux, which defines the salinity flux, the difference between evaporation Q_E (from bulk formulae) and precipitation Q_P (from observations or atmospheric models) is calculated:

$$\nu_t' \partial_z S = \frac{S(Q_E - Q_P)}{\rho_0(0)}, \qquad \text{for } z = \zeta, \tag{2.37}$$

where $\rho_0(0)$ is the density of freshwater at sea surface temperature. In the presence of sea-ice, the calculation of freshwater flux is more complex, see e.g. *Large et al.* [1994]. However, for many short term calculations, the freshwater flux can often be neglected compared to the surface heat flux.
Heat and salinity fluxes at the bottom are set to zero.

2.3 Vertical turbulent exchange

The eddy viscosity ν_t (for momentum) and eddy diffusivity ν_t' (for tracers) need to be parameterised by means of turbulence models. Such models may range from simple algebraic prescription of profiles of ν_t and ν_t' (see *Perels and Karelse* [1982]), via zero-, one, or two-equation models (see e.g. *Luyten et al.* [1996]) to full Reynolds stress closure models (see e.g. *Launder et al.* [1975]). In GETM, a compromise between accuracy and computational effort is made in such a way, that usually two-equation models are used.
The turbulence module of the Public Domain water column model GOTM (General Ocean Turbulence Model, see `http://www.gotm.net`) which has been developed by *Burchard et al.* [1999] is implemented into GETM. This allows for great flexibility in the choice of the turbulence model and guarantees that a well-tested state-of-the-art turbulence model is always at hand inside GETM.
The features of GOTM have been reported in a number of publications, see *Burchard and Bolding* [2001], *Burchard* [2001a] and *Burchard and Deleersnijder* [2001] and the citations therein. Various comparative calculations with in-situ turbulence measurements have been carried out with GOTM, which gives some confidence into the model, see e.g. *Bolding et al.* [2000], *Burchard et al.* [2001], *Simpson et al.* [2001] and *Stips et al.* [2001].
GOTM has various options for turbulence models, but only some of them have been proven to give reasonable results for vertical exchange. The research for improving turbulence models is still ongoing. Presently, better parameterisations for surface wave activity and internal wave activity are under development.
So far, the best experience inside GOTM has been made with k-ε (see *Launder and Spalding* [1972], *Rodi* [1980]) and Mellor-Yamada (*Mellor and Yamada* [1974] and *Mellor and Yamada* [1982] two-equation models:
The basic form of the k-ε model is the following (see *Burchard* [2001c]):

$$\partial_t k - \partial_z \left(\left(\nu + \frac{\nu_t}{\sigma_k} \right) \partial_z k \right) = P + B - \varepsilon, \tag{2.38}$$

$$\partial_t \varepsilon - \partial_z \left(\left(\nu + \frac{\nu_t}{\sigma_\varepsilon} \right) \partial_z \varepsilon \right) = \frac{\varepsilon}{k} (c_{1\varepsilon} P + c_{3\varepsilon} B - c_{2\varepsilon} \varepsilon), \tag{2.39}$$

with the equation for turbulent kinetic energy, (2.38), and for its dissipation rate ε, (2.39). σ_k and σ_ε denote turbulent Schmidt numbers for vertical diffusion of k and ε, respectively, and P and B are shear and buoyancy production, respectively with:

$$P = \nu_t \left((\partial_z u)^2 + (\partial_z v)^2 \right), \qquad B = -\nu_t' \partial_z b, \tag{2.40}$$

and $c_{1\varepsilon}$, $c_{2\varepsilon}$, and $c_{3\varepsilon}$ are empirical parameters.
The Mellor-Yamada two-equation model (see *Mellor and Yamada* [1982]) uses a slightly different equation for k and a transport equation for the quantity kL with the macro length scale L instead of an ε-equation:

$$\partial_t k - \partial_z \left(S_q \sqrt{2k} L \partial_z k \right) = P + B - \varepsilon, \tag{2.41}$$

$$\partial_t (kL) - \partial_z \left(S_l \sqrt{2k} L \partial_z (kL) \right) = \frac{L}{2} \left[E_1 P + E_3 B - \left(1 + E_2 \left(\frac{L}{L_z} \right)^2 \right) \varepsilon \right]. \tag{2.42}$$

Here, S_q, S_l, E_1, E_2, and E_3 are empirical parameters, and L_z is an empirical length scale related to the distance from surface and bottom.
Suitable bottom and surface boundary conditions for k, ε and kL can be derived from the law of the wall, although modifications are needed near the surface due to breaking of surface waves (see *Craig and Banner* [1994], *Craig* [1996], *Burchard* [2001b]).
The three turbulent parameter k, ε and L are interrelated through:

$$L = c_L \frac{k^{3/2}}{\varepsilon} \tag{2.43}$$

with the empirical parameter c_L.
From k and ε, the eddy viscosity and diffusivity can finally be calculated by the following relation:

$$\nu_t = c_\mu \frac{k^2}{\varepsilon}, \qquad \nu'_t = c'_\mu \frac{k^2}{\varepsilon}. \tag{2.44}$$

Here, c_μ and c'_μ are so-called stability functions usually depending on shear, stratification and turbulent time scale, $\tau = k/\varepsilon$.
Various sets of stability functions, which contain second-moment closure assumptions have been suggested. The most successful in terms of comparison to laboratory and field data seems to be the closure introduced by *Canuto et al.* [2001].
Recently, *Umlauf and Burchard* [2001] suggested a generic two-equation model with the TKE equation (2.38) and a length scale related transport equation for a variable $k^n \varepsilon^m$, see also *Burchard* [2001c]. The advantage of such a model is the higher number of degrees of freedom. For well mixed flow with $B = 0$ for example, in addition to $c_{\varepsilon 1}$, $c_{\varepsilon 2}$, σ_k, σ_ε, and c^0_μ now also n and m can be calibrated in such a way that idealised physical situations can be reproduced. Here, c^0_μ denotes the value of c_μ for $P = \varepsilon$ and $B = 0$. This new generic model will be included into one of the next releases of GOTM, such that it can be used in combination with GETM as well.
The turbulence model is coupled to the hydrodynamic model via the turbulence production terms P and B as input and the eddy viscosity and diffusivity ν_t and ν'_t as output. Furthermore, surface and bottom roughness lengths are needed for the boundary conditions inside the turbulence model. Finally, the three-dimensional model needs to store two quantities out of k, ε and L since GOTM is a one-dimensional model which has to read in the "old" values of k, ε and L for each horizontal position.

Chapter 3

Transformations

3.1 Layer integration

3.1.1 General vertical coordinates

As a preparation of the discretisation, the physical space is vertically divided into N layers. This is done by introducing internal surfaces z_k, $k = 1, \ldots, N-1$ which do not intersect, each depending on the horizontal position (x, y) and time t. Let

$$-H(x,y) = z_0(x,y) < z_1(x,y,t) < \cdots < z_{N-1}(x,y,t) < z_N(x,y,t) = \zeta(x,y,t) \tag{3.1}$$

define the local layer depths h_k with

$$h_k = z_k - z_{k-1}. \tag{3.2}$$

for $1 \leq k \leq N$. For simplicity, the argument (x, y, t) is omitted in most of the cases. The most simple layer distribution is given by the so-called σ transformation (see *Phillips* [1957] for a first application in meteorology and *Freeman et al.* [1972] for a first application in hydrodynamics) with

$$\sigma_k = \frac{k}{N} - 1 \tag{3.3}$$

and

$$z_k = D\sigma_k \tag{3.4}$$

for $0 \leq k \leq N$.
The σ-coordinates can also be refined towards the surface and the bed:

$$\beta_k = \frac{\tanh\left((d_l + d_u)(1 + \sigma_k) - d_l\right) + \tanh(d_l)}{\tanh(d_l) + \tanh(d_u)} - 1, \qquad k = 0, \ldots, N \tag{3.5}$$

such that z-levels are obtained as follows:

$$z_k = D\beta_k \tag{3.6}$$

for $0 \leq k \leq N$.
The grid is refined towards the surface for $d_u > 0$ and refined towards the bottom for $d_l > 0$. When both, d_u and d_l are larger than zero, then refinement towards surface and bed is obtained. For $d_u = d_l = 0$ the σ-transformation (3.3) with $\beta_k = \sigma_k$ is retained. Figure 3.1 shows four examples for vertical layer distributions obtained with the σ-transformation.
Due to the fact that all layer thicknesses are proportional to the water depth, the equidistant and also the non-equidistant σ-transformations, (3.3) and (3.5), have however one striking disadvantage. In order to sufficiently resolve the mixed layer also in deep water, many layers have to be located near the surface. The same holds for the bottom boundary layer. This problem of σ-coordinates has been discussed by several authors (see e.g. *Deleersnijder and Ruddick* [1992], *de Kok* [1992], *Gerdes* [1993], *Song and Haidvogel* [1994], *Burchard and Petersen* [1997]) who suggested methods for generalised vertical coordinates not resulting in layer thicknesses not proportional to the water depth.
The generalised vertical coordinate introduced here is a generalisation of the so-called mixed-layer transformation suggested by *Burchard and Petersen* [1997]. It is a hybrid coordinate which interpolates between the equidistant and the non-equidistant σ-transformations given by (3.3) and (3.5). The weight for the interpolation depends on the ratio of a critical water depth D_γ (below which equidistant σ-coordinates are used) and the actual water depth:

$$z_k = D\left(\alpha_\gamma \sigma_k + (1 - \alpha_\gamma)\beta_k\right) \tag{3.7}$$

with

$$\alpha_\gamma = \min\left(\frac{(\beta_k - \beta_{k-1}) - \frac{D_\gamma}{D}(\sigma_k - \sigma_{k-1})}{(\beta_k - \beta_{k-1}) - (\sigma_k - \sigma_{k-1})}, 1\right). \tag{3.8}$$

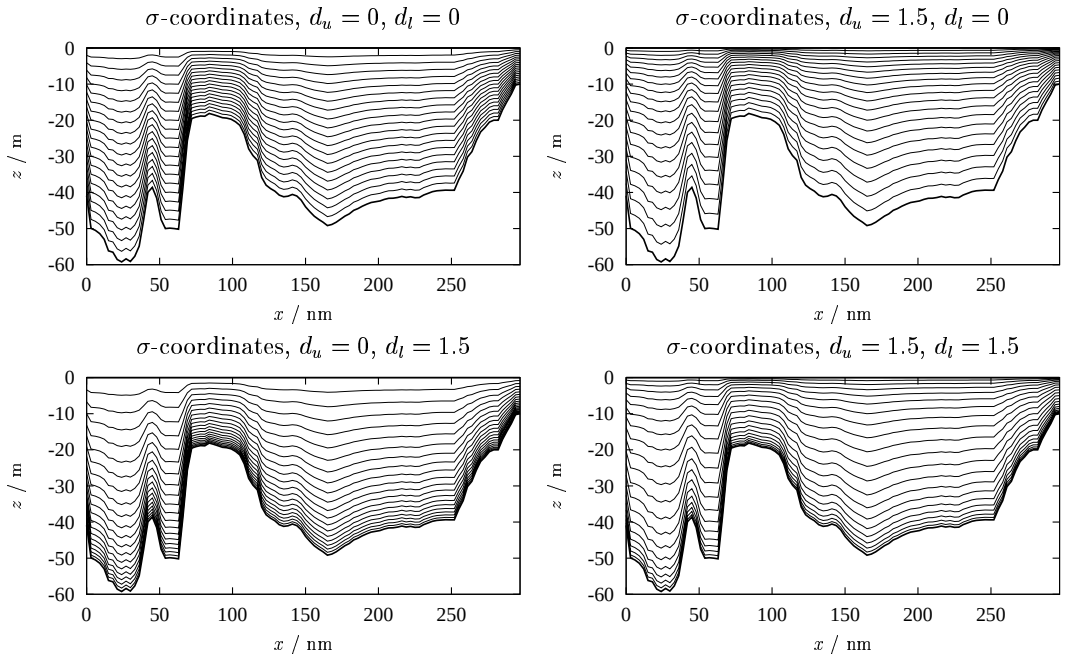

Figure 3.1: σ-transformation with four different zooming options. The plots show the vertical layer distribution for a cross section through the North Sea from Scarborough in England to Esbjerg in Denmark. The shallow area at about $x = 100$ nm is the Doggerbank.

and σ_k from (3.3) and β_k from (3.5).

For inserting $k = N$ in (3.8) and $d_l = 0$ and $d_u > 0$ in (3.5), the mixed layer transformation of *Burchard and Petersen* [1997] is retained, see the upper two panels in figure 3.2. Depending on the values for D_γ and d_u, some near-surface layer thicknesses will be constant in time and space, allowing for a good vertical resolution in the surface mixed layer.

The same is obtained for the bottom with the following settings: $k = 1$, $d_l > 0$ and $d_u = 0$, see the lower two panels in figure 3.2. This is recommended for reproducing sedimentation dynamics and other benthic processes. For $d_l = d_u > 0$ and $k = 1$ or $k = N$ a number of layers near the surface and near the bottom can be fixed to constant thickness. Intermediate states are obtained by intermediate settings, see figure 3.3. Some pathological settings are also possible, such as $k = 1$, $d_l = 1.5$ and $d_u = 5$, see figure 3.4.

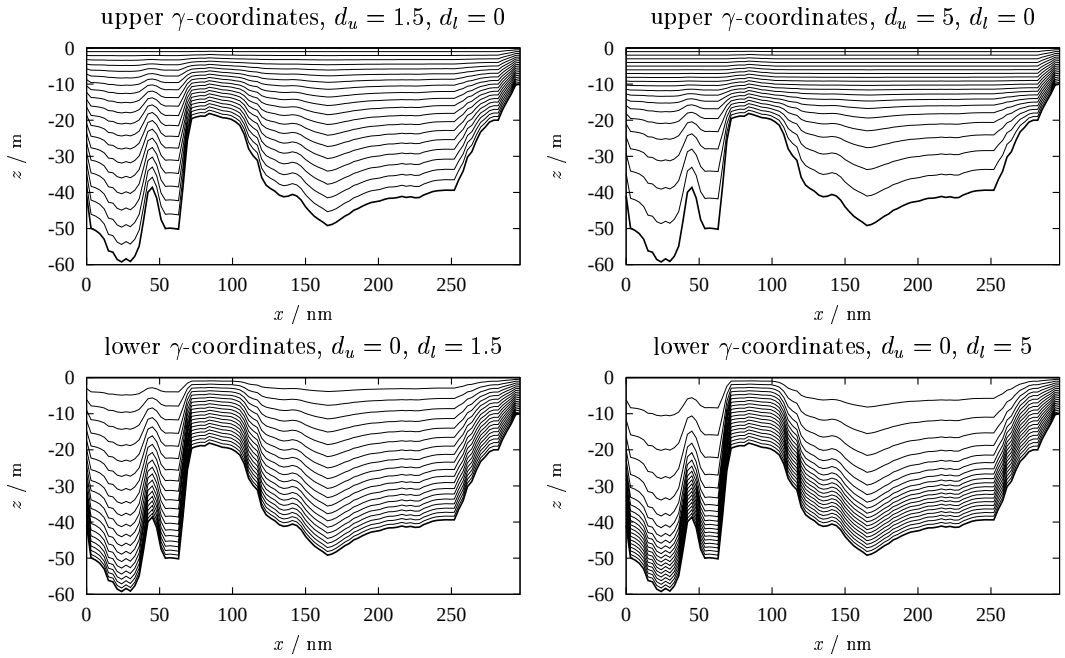

Figure 3.2: Boundary layer transformation (or γ transformation) with concentration of layers in the surface mixed layer (upper two panels) and with concentration of layers in the bottom mixed layer (lower two panels). The critical depth D_γ is here set to 20 m, such that at all shallower depths the equidistant σ-transformation is used. The same underlying bathymetry as in figure 3.1 has been used.

3.1.2 Layer-integrated equations

There are two different ways to derive the layer-integrated equations. *Burchard and Petersen* [1997] transform first the equations into general vertical coordinate form (see *Deleersnijder and Ruddick* [1992]) and afterwards integrate the transformed equations over constant intervals in the transformed space. *Lander et al.* [1994] integrate the equations in the Cartesian space over surfaces z_k by considering the Leibniz rule

$$\int_{z_{k-1}}^{z_k} \partial_x f \, dz = \partial_x \int_{z_{k-1}}^{z_k} f \, dz - f(z_k)\partial_x z_k + f(z_{k-1})\partial_x z_{k-1} \tag{3.9}$$

for any function f. For the vertical staggering of the layer notation see figure 4.4. More details about the layer integration are given in *Burchard and Petersen* [1997].

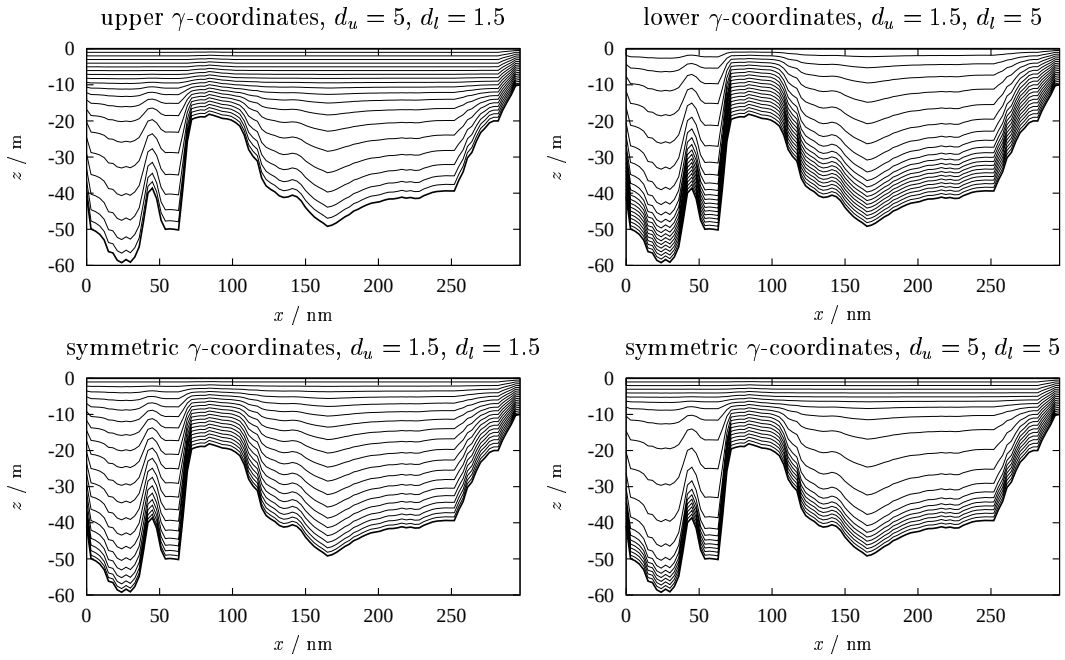

Figure 3.3: Boundary layer transformation (or γ transformation) with concentration of layers in both, the surface mixed layer and the bottom mixed layer. Four different realisations are shown. The critical depth D_γ is here set to 20 m, such that at all shallower depths the equidistant σ-transformation is used. The same underlying bathymetry as in figure 3.1 has been used.

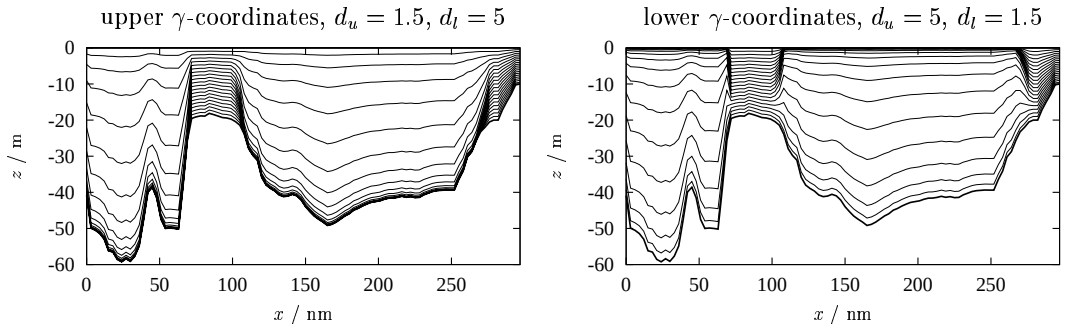

Figure 3.4: Two pathological examples for the boundary layer transformation. The critical depth D_γ is here set to 20 m, such that at all shallower depths the equidistant σ-transformation is used. The same underlying bathymetry as in figure 3.1 has been used.

With the further definitions of layer integrated transport,

$$p_k := \int_{z_{k-1}}^{z_k} u\, dz, \qquad q_k := \int_{z_{k-1}}^{z_k} v\, dz, \tag{3.10}$$

layer mean velocities,

$$u_k := \frac{p_k}{h_k}, \qquad v_k := \frac{q_k}{h_k}, \tag{3.11}$$

and layer averaged tracer concentrations and buoyancy,

$$c_k^i := \frac{1}{h_k}\int_{z_{k-1}}^{z_k} c^i\, dz, \qquad b_k := \frac{1}{h_k}\int_{z_{k-1}}^{z_k} b\, dz, \tag{3.12}$$

and the grid related vertical velocity,

$$\bar{w}_k := (w - u\partial_x z - v\partial_y z)_{z=z_k}, \tag{3.13}$$

the continuity equation (2.3) has the layer-integrated form:

$$\partial_t h_k + \partial_x p_k + \partial_y q_k + \bar{w}_k - \bar{w}_{k-1} = 0. \tag{3.14}$$

It should be noted that the grid related velocity is located on the layer interfaces. After this, the layer-integrated momentum equations read as:

$$\begin{aligned}
&\partial_t p_k + \bar{w}_k\tilde{u}_k - \bar{w}_{k-1}\tilde{u}_{k-1} - \tau_k^x + \tau_{k-1}^x \\
&\quad +\alpha\Big\{ \partial_x(u_k p_k) + \partial_y(v_k p_k) \\
&\quad -\partial_x\left(2A_k^M h_k \partial_x u_k\right) - \partial_y\left(A_k^M h_k(\partial_y u_k + \partial_x v_k)\right) - f q_k \\
&\quad -h_k\left(\frac{1}{2}h_N(\partial_x^* b)_N + \sum_{j=k}^{N-1}\frac{1}{2}(h_j + h_{j+1})(\partial_x^* b)_j\right)\Big\} = -g h_k \partial_x \zeta,
\end{aligned} \tag{3.15}$$

$$
\begin{aligned}
&\partial_t q_k + \bar{w}_k \tilde{v}_k - \bar{w}_{k-1}\tilde{v}_{k-1} - \tau^y_k + \tau^y_{k-1} \\
&+\alpha \Big\{ \partial_x(u_k q_k) + \partial_y(v_k q_k) \\
&-\partial_y \left(2A^M_k h_k \partial_y v_k\right) - \partial_x \left(A^M_k h_k (\partial_y u_k + \partial_x v_k)\right) + f p_k \\
&-h_k \left(\frac{1}{2} h_N (\partial^*_y b)_N + \sum_{j=k}^{N-1} \frac{1}{2}(h_j + h_{j+1})(\partial^*_y b)_j \right) \Big\} = -g h_k \partial_y \zeta
\end{aligned}
\tag{3.16}
$$

with suitably chosen advective horizontal velocities $\tilde{u}_k$ and $\tilde{v}_k$ (see section 4.7), the shear stresses

$$\tau^x_k = \left(\nu_t \partial_z u\right)_k , \tag{3.17}$$

and

$$\tau^y_k = \left(\nu_t \partial_z v\right)_k , \tag{3.18}$$

and the horizontal buoyancy gradients

$$(\partial^*_x b)_k = \frac{1}{2}(\partial_x b_{k+1} + \partial_x b_k) - \partial_x z_k \frac{b_{k+1} - b_k}{\frac{1}{2}(h_{k+1} + h_k)} \tag{3.19}$$

and

$$(\partial^*_y b)_k = \frac{1}{2}(\partial_y b_{k+1} + \partial_y b_k) - \partial_y z_k \frac{b_{k+1} - b_k}{\frac{1}{2}(h_{k+1} + h_k)}. \tag{3.20}$$

The layer integration of the pressure gradient force is discussed in detail by *Burchard* [1996] and *Burchard and Petersen* [1997].
A conservative formulation can be derived for the recalculation of the physical vertical velocity w which is convenient in the discrete space if w is evaluated at the layer centres (see *Deleersnijder and Ruddick* [1992]):

$$w_k = \frac{1}{h_k}\left(\partial_t(h_k z_{k-1/2}) + \partial_x(p_k z_{k-1/2}) + \partial_y(q_k z_{k-1/2}) + \bar{w}_k z_k - \bar{w}_{k-1} z_{k-1}\right). \tag{3.21}$$

It should be mentioned that w only needs to be evaluated for post-processing reasons. For the layer-integrated tracer concentrations, we obtain the following expression:

$$\begin{aligned}&\partial_t(h_k c_k^i) + \partial_x(p_k c_k^i) + \partial_y(q_k c_k^i) + (\bar{w}_k + w_k^s)\tilde{c}_k^i - (\bar{w}_{k-1} + w_{k-1}^s)\tilde{c}_{k-1}^i \\ &\quad -(\nu_t' \partial_z c^i)_k + (\nu_t' \partial_z c^i)_{k-1} - \partial_x\left(A_k^T h_k \partial_x c_k^i\right) - \partial_y\left(A_k^T h_k \partial_y c_k^i\right) = Q_k^i.\end{aligned} \tag{3.22}$$

It should be noted that the "horizontal" diffusion does no longer occur along geopotential surfaces but along horizontal coordinate lines. The properly transformed formulation would include some cross-diagonal terms which may lead to numerical instabilities due to violation of monotonicity. For an in-depth discussion of this problem, see *Beckers et al.* [1998] and *Beckers et al.* [2000].

3.2 Horizontal curvilinear coordinates

In this section, the layer-integrated equations from section 3.1 are transformed to horizontal orthogonal curvilinear coordinates. Similarly to general coordinates in the vertical, these allow for much more flexibility when optimising horizontal grids to coast-lines and bathymetry. Furthermore, this type of coordinates system includes spherical coordinates as a special case. The derivation of the transformed equations is carried out here according to *Haidvogel and Beckmann* [1999], see also *Arakawa and Lamb* [1977].
A rectangular domain with non-dimensional side lengths and with local Cartesian coordinates $\mathcal{X}$ and $\mathcal{Y}$ is mapped to a physical domain with four corners in such a way that the local coordinates of the physical space, (ξ_x, ξ_y) are orthogonal to each others everywhere:

$$\mathcal{X} \to \xi_x, \quad \mathcal{Y} \to \xi_y. \tag{3.23}$$

The infinitesimal increments in the physical space, $d\,\xi_x$ and $d\,\xi_y$ are related to the infinitesimal increments in the transformed space, $d\,\mathcal{X}$ and $d\,\mathcal{Y}$ by so-called metric coefficients $m(x, y)$ and $n(x, y)$:

$$d\,\xi_x = \left(\frac{1}{m}\right) d\,\mathcal{X}, \quad d\,\xi_y = \left(\frac{1}{n}\right) d\,\mathcal{Y}. \tag{3.24}$$

These metric coefficients have the physical unit of $[\mathrm{m}^{-1}]$. With $m = n$ =const, Cartesian coordinates are retained, and with

$$m = \frac{1}{r_E \cos\phi}, \quad n = \frac{1}{r_E}, \tag{3.25}$$

spherical coordinates with $\mathcal{X} = \lambda$ and $\mathcal{Y} = \phi$ are retained (with the Earth's radius r_E, longitude λ and latitude ϕ).
With these notations, the layer-integrated equations (3.14), (3.15), and (3.16) given in section 3.1 can be formulated as follows:

Continuity equation:

$$\partial_t \left(\frac{h_k}{mn}\right) + \partial_{\mathcal{X}} \left(\frac{p_k}{n}\right) + \partial_{\mathcal{Y}} \left(\frac{q_k}{m}\right) + \frac{\bar{w}_k - \bar{w}_{k-1}}{mn} = 0. \tag{3.26}$$

Momentum in ξ_x direction:

$$\begin{aligned}
&\partial_t \left(\frac{p_k}{mn}\right) + \frac{\bar{w}_k \tilde{u}_k - \bar{w}_{k-1}\tilde{u}_{k-1}}{mn} - \frac{\tau_k^{\mathcal{X}} - \tau_{k-1}^{\mathcal{X}}}{mn} \\
&+\alpha \Bigg\{ \partial_{\mathcal{X}} \left(\frac{u_k p_k}{n}\right) + \partial_{\mathcal{Y}} \left(\frac{v_k p_k}{m}\right) - q_k \left(\frac{f}{mn} + v_k \partial_{\mathcal{X}} \left(\frac{1}{n}\right) - u_k \partial_{\mathcal{Y}} \left(\frac{1}{m}\right)\right) \\
&-\partial_{\mathcal{X}} \left(\frac{2A_k^M h_k}{n} m \partial_{\mathcal{X}} u_k\right) - \partial_{\mathcal{Y}} \left(\frac{A_k^M h_k}{m}(n\partial_{\mathcal{Y}} u_k + m\partial_{\mathcal{X}} v_k)\right) \\
&-\frac{h_k}{n}\left(\frac{1}{2} h_N (\partial_{\mathcal{X}}^* b)_N + \sum_{j=k}^{N-1} \frac{1}{2}(h_j + h_{j+1})(\partial_{\mathcal{X}}^* b)_j\right) \Bigg\} = -g \frac{h_k}{n} \partial_{\mathcal{X}} \zeta.
\end{aligned} \tag{3.27}$$

Momentum in ξ_y direction:

$$\begin{aligned}
&\partial_t\left(\frac{q_k}{mn}\right)+\frac{\bar{w}_k\tilde{v}_k-\bar{w}_{k-1}\tilde{v}_{k-1}}{mn}-\frac{\tau^{\mathcal{Y}}_k-\tau^{\mathcal{Y}}_{k-1}}{mn}\\
&+\alpha\Bigg\{\partial_{\mathcal{X}}\left(\frac{u_kq_k}{n}\right)+\partial_{\mathcal{Y}}\left(\frac{v_kq_k}{m}\right)+p_k\left(\frac{f}{mn}+v_k\partial_{\mathcal{X}}\left(\frac{1}{n}\right)-u_k\partial_{\mathcal{Y}}\left(\frac{1}{m}\right)\right)\\
&-\partial_{\mathcal{Y}}\left(\frac{2A^M_kh_k}{m}n\partial_{\mathcal{Y}}v_k\right)-\partial_{\mathcal{X}}\left(\frac{A^M_kh_k}{n}(n\partial_{\mathcal{Y}}u_k+m\partial_{\mathcal{X}}v_k)\right)\\
&-\frac{h_k}{m}\left(\frac{1}{2}h_N(\partial^*_{\mathcal{Y}}b)_N+\sum_{j=k}^{N-1}\frac{1}{2}(h_j+h_{j+1})(\partial^*_{\mathcal{Y}}b)_j\right)\Bigg\}=-g\frac{h_k}{m}\partial_{\mathcal{Y}}\zeta.
\end{aligned}\tag{3.28}$$

In (3.27) and (3.28), the velocity and momentum components u_k and p_k are now pointing into the ξ_x-direction and v_k and q_k are pointing into the ξ_y-direction. The stresses $\tau^{\mathcal{X}}_k$ and $\tau^{\mathcal{Y}}_k$ are related to these directions as well. In order to account for this rotation of the velocity and momentum vectors, the rotational terms due to the Coriolis rotation are extended by terms related to the gradients of the metric coefficients. This rotation is here not considered for the horizontal diffusion terms in order not to unnecessarily complicate the equations. Instead we use the simplified formulation by *Kantha and Clayson* [2000b], who argue that it does not make sense to use complex formulations for minor processes with highly empirical parameterisations. Finally, the tracer equation is of the following form after the transformation to curvilinear coordinates:

$$\begin{aligned}
&\partial_t\left(\frac{h_kc^i_k}{mn}\right)+\partial_{\mathcal{X}}\left(\frac{p_kc^i_k}{n}\right)+\partial_{\mathcal{Y}}\left(\frac{q_kc^i_k}{m}\right)+\frac{\bar{w}_k\tilde{c}^i_k-\bar{w}_{k-1}\tilde{c}^i_{k-1}}{mn}\\
&-\frac{(\nu'_t\partial_zc^i)_k-(\nu'_t\partial_zc^i)_{k-1}}{mn}\\
&-\partial_{\mathcal{X}}\left(\frac{A^T_kh_k}{n}m\partial_{\mathcal{X}}c^i_k\right)-\partial_{\mathcal{Y}}\left(\frac{A^T_kh_k}{m}n\partial_{\mathcal{Y}}c^i_k\right)=\frac{Q^i_k}{mn}.
\end{aligned}\tag{3.29}$$

Chapter 4

Discretisation

4.1 Mode splitting

The external system consisting of the surface elevation equation (2.12) and the transport equations (2.16) and (2.17) underlies a strict time step constraint if the discretisation is carried out explicitly:

$$\Delta t < \left[\frac{1}{2}\left(\frac{1}{\Delta x}+\frac{1}{\Delta y}\right)\sqrt{2gD}\right]^{-1}. \tag{4.1}$$

In contrast to that, the time step of the internal system is only depending on the Courant number for advection,

$$\Delta t < \min\left\{\frac{\Delta x}{u_{\max}}, \frac{\Delta y}{v_{\max}}\right\}, \tag{4.2}$$

which in the case of sub-critical flow is a much weaker constraint. In order not to punish the whole model with a small time step resulting from the external system, two different approaches of mode splitting have been developed in the past.
The first approach, in which the external mode is calculated implicitly, has been proposed by *Madala and Piacsek* [1977]. This method is numerically stable (if advection is absent) for unconditionally long time steps. The temporal approximation is of second order if semi-implicit treatment is chosen. In such models, the external and internal mode are generally calculated with the same time steps (see e.g. *Backhaus* [1985]). The introduction of interactions terms like (2.18) - (2.25) is thus not necessary in such models.

Another approach is to use different time steps for the internal (macro times steps Δt) and the external mode (micro time steps Δt_m). One of the first free surface models which has adopted this method is the Princeton Ocean Model (POM), see *Blumberg and Mellor* [1987]. This method has the disadvantage that interaction terms are needed for the external mode and that the consistency between internal and external mode is difficult to obtain. The advantage of this method is that the free surface elevation is temporally well resolved which is a major requirement for models including flooding and drying. That is the reason why this method is adopted here.
The micro time step Δt_m has to be an integer fraction M of the macro time step Δt. Δt_m is limited by the speed of the surface waves (4.1), Δt is limited by the current speed (4.2). The time stepping principle is shown in figure 4.1. The vertically integrated transports are averaged over each macro time step:

$$\bar{U}_{i,j}^{n+1/2} = \frac{1}{M} \sum_{l=n+0.5/M}^{n+(M-0.5)/M} U_{i,j}^{l} \tag{4.3}$$

and

$$\bar{V}_{i,j}^{n+1/2} = \frac{1}{M} \sum_{l=n+0.5/M}^{n+(M-0.5)/M} V_{i,j}^{l} \tag{4.4}$$

such that

$$\frac{\zeta_{i,j}^{n+1} - \zeta_{i,j}^{n}}{\Delta t} = -\frac{\bar{U}_{i,j}^{n+1/2} - \bar{U}_{i-1,j}^{n+1/2}}{\Delta x} - \frac{\bar{V}_{i,j}^{n+1/2} - \bar{V}_{i,j-1}^{n+1/2}}{\Delta y}. \tag{4.5}$$

4.2 General vertical diffusion equation

In the following, the discretisation of a simple diffusion equation

$$\partial_t X - \partial_z(\nu \partial_z X) = Q \tag{4.6}$$

will be shown for a general physical quantity X which could be momentum u or v or a tracer or turbulent quantity. Q denotes all source terms which will be discretised on the "old" time level. After layer integration, (4.6) is of the form

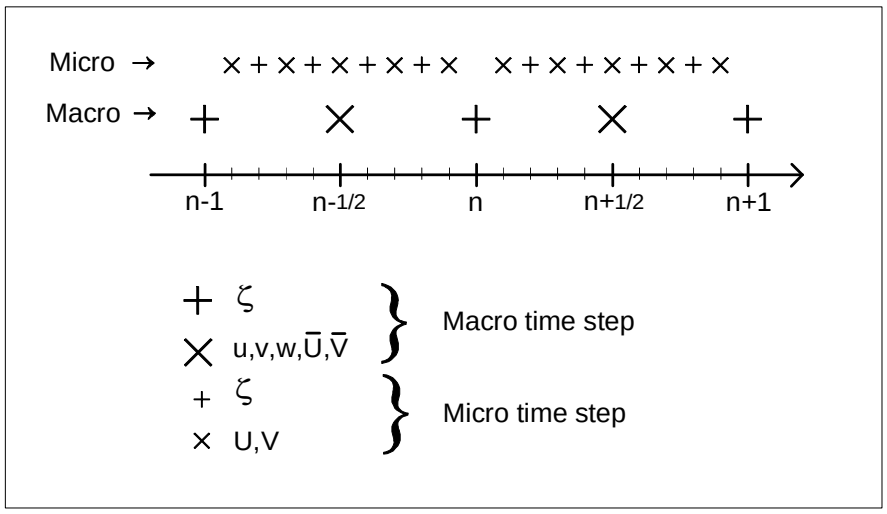

Figure 4.1: Sketch explaining the organisation of the time stepping.

$$\partial_t(h_k X_k) - (\nu \partial_z X)\Big|_k + (\nu \partial_z X)\Big|_{k-1} = h_k Q_k \tag{4.7}$$

where X_k and Q_k denote layer averages of X and Q, respectively[1].
with the Neumann-type boundary conditions

$$\nu \partial_z X = F_s \qquad \text{for } z = \zeta, \tag{4.8}$$

and

$$\nu \partial_z X = -F_b \qquad \text{for } z = -H, \tag{4.9}$$

the semi-implicit discretisation is for a mean flow quantity such as momentum or tracers of the following form:

[1]With time-varying depth some extra terms would appear due to the Leibniz rule (3.9). These would however be compensated by advective terms which are here contained in the source term Q for simplicity.

$$\frac{h_N^{n+1}X_N^{n+1} - h_N^n X_N^n}{\Delta t} - F_s + \nu_{N-1}^n \frac{X_N^{n+\sigma} - X_{N-1}^{n+\sigma}}{\frac{1}{2}(h_N^{n+\sigma} + h_{N-1}^{n+\sigma})} = h_N^n Q_N^n, \tag{4.10}$$

$$\begin{aligned} &\frac{h_k^{n+1}X_k^{n+1} - h_k^n X_k^n}{\Delta t} - \nu_k^n \frac{X_{k+1}^{n+\sigma} - X_k^{n+\sigma}}{\frac{1}{2}(h_{k+1}^{n+\sigma} + h_k^{n+\sigma})} \\ &\quad + \nu_{k-1}^n \frac{X_k^{n+\sigma} - X_{k-1}^{n+\sigma}}{\frac{1}{2}(h_k^{n+\sigma} + h_{k-1}^{n+\sigma})} = h_k^n Q_k^n \qquad \text{for } 1 < k < N, \end{aligned} \tag{4.11}$$

$$\frac{h_1^{n+1}X_1^{n+1} - h_1^n X_1^n}{\Delta t} - \nu_1^n \frac{X_2^{n+\sigma} - X_1^{n+\sigma}}{\frac{1}{2}(h_2^{n+\sigma} + h_1^{n+\sigma})} - F_b = h_1^n Q_1^n, \tag{4.12}$$

with

$$X_k^{n+\sigma} = \sigma X_k^{n+1} + (1-\sigma) X_k^n \tag{4.13}$$

and

$$h_k^{n+\sigma} = \sigma h_k^{n+1} + (1-\sigma) h_k^n. \tag{4.14}$$

Upper indices denote time levels (n for "old" and $n+1$ for "new") and lower indices denote the vertical discrete location. Horizontal indices (i, j) are omitted for simplicity. Thus, for $\sigma = 0$ a fully explicit, for $\sigma = 1$ a fully implicit and for $\sigma = 0.5$ the Crank-Nicholson second-order in time scheme is obtained.
This semi-implicit differencing leads for each transport equation to a system of linear equations with the following tri-diagonal matrix:

$$\begin{aligned} &-X_{N-1}^{n+1} \frac{\sigma \Delta t\, \nu_{N-1}^n}{\frac{1}{2}(h_N^{n+\sigma} + h_{N-1}^{n+\sigma})} \\ &+X_N^{n+1} \left(h_N^{n+1} + \frac{\sigma \Delta t\, \nu_{N-1}^n}{\frac{1}{2}(h_N^{n+\sigma} + h_{N-1}^{n+\sigma})} \right) = \\ &\quad X_{N-1}^n \frac{(1-\sigma)\Delta t\, \nu_{N-1}^n}{\frac{1}{2}(h_N^{n+\sigma} + h_{N-1}^{n+\sigma})} \\ &\quad +X_N^n \left(h_N^n - \frac{(1-\sigma)\Delta t\, \nu_{N-1}^n}{\frac{1}{2}(h_N^{n+\sigma} + h_{N-1}^{n+\sigma})} \right) + \Delta t\, F_s + \Delta t\, h_N^n Q_N^n \end{aligned} \tag{4.15}$$

$$
\begin{aligned}
&-X_{k-1}^{n+1}\frac{\sigma\Delta t\,\nu_{k-1}^{n}}{\frac{1}{2}(h_k^{n+\sigma}+h_{k-1}^{n+\sigma})}\\
&+X_k^{n+1}\left(h_k^{n+1}+\frac{\sigma\Delta t\,\nu_{k-1}^{n}}{\frac{1}{2}(h_k^{n+\sigma}+h_{k-1}^{n+\sigma})}+\frac{\sigma\Delta t\,\nu_k^{n}}{\frac{1}{2}(h_{k+1}^{n+\sigma}+h_k^{n+\sigma})}\right)\\
&-X_{k+1}^{n+1}\frac{\sigma\Delta t\,\nu_k^{n}}{\frac{1}{2}(h_{k+1}^{n+\sigma}+h_k^{n+\sigma})}=\\
&\qquad X_{k-1}^{n}\frac{(1-\sigma)\Delta t\,\nu_{k-1}^{n}}{\frac{1}{2}(h_k^{n+\sigma}+h_{k-1}^{n+\sigma})}\\
&\qquad +X_k^{n}\left(h_k^{n}-\frac{(1-\sigma)\Delta t\,\nu_{k-1}^{n}}{\frac{1}{2}(h_k^{n+\sigma}+h_{k-1}^{n+\sigma})}-\frac{(1-\sigma)\Delta t\,\nu_k^{n}}{\frac{1}{2}(h_{k+1}^{n+\sigma}+h_k^{n+\sigma})}\right)\\
&\qquad +X_{k+1}^{n}\frac{(1-\sigma)\Delta t\,\nu_k^{n}}{\frac{1}{2}(h_{k+1}^{n+\sigma}+h_k^{n+\sigma})}+\Delta t\,h_k^{n}Q_k^{n}\qquad\text{for } 1<k<N,
\end{aligned}
\tag{4.16}
$$

$$
\begin{aligned}
&X_1^{n+1}\left(h_1^{n+1}+\frac{\sigma\Delta t\,\nu_1^{n}}{\frac{1}{2}(h_2^{n+\sigma}+h_1^{n+\sigma})}\right)\\
&-X_2^{n+1}\frac{\sigma\Delta t\,\nu_1^{n}}{\frac{1}{2}(h_2^{n+\sigma}+h_1^{n+\sigma})}=\\
&\qquad X_1^{n}\left(h_1^{n}-\frac{(1-\sigma)\Delta t\,\nu_1^{n}}{\frac{1}{2}(h_2^{n+\sigma}+h_1^{n+\sigma})}\right)\\
&\qquad +X_2^{n}\frac{(1-\sigma)\Delta t\,\nu_1^{n}}{\frac{1}{2}(h_2^{n+\sigma}+h_1^{n+\sigma})}+\Delta t\,F_b+\Delta t\,h_1^{n}Q_1^{n},
\end{aligned}
\tag{4.17}
$$

which is solved by means of the simplified Gaussian elimination, see e.g. *Samarskij* [1984].

It should be noted that the source term Q is often treated quasi-implicitly, following a suggestion made by *Patankar* [1980] (see also *Deleersnijder et al.* [1997]). This is

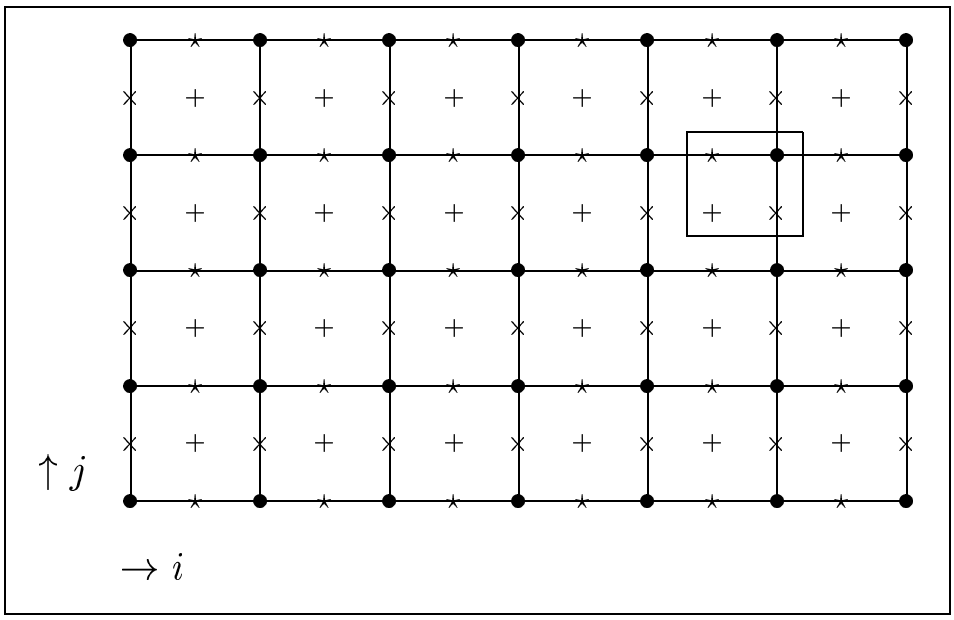

Figure 4.2: Layout of the model horizontal model grid in Cartesian coordinates. Shown are the reference boxes for the T-points. The following symbols are used: $+$: T-points; $\times$: U-points; $\star$: V-points; $\bullet$: X-points. The inserted box denotes grid points with the same index (i, j).

done in order to guarantee positive discrete solutions for physically positive quantities such as concentrations or turbulent quantities. For details of this numerical scheme, which used for positive quantities in GETM, see also *Burchard* [2001c].

4.3 Spatial discretisation

For the spatial discretisation, a staggered C-grid is used, see *Arakawa and Lamb* [1977]. The grid consists of prism-shaped finite volumes with the edges aligned with coordinates. The reference grid for the tracer points (from now on denoted by T-points) is shown in figures 4.2 and 4.4. The velocity points are located such that the corresponding velocity components are centralised on the surfaces of the T-point reference box, the u-velocity points (from now on U-points) at the western and eastern surfaces, the v-velocity points (from now on V-points) at the southern and northern surfaces and the w-velocity points (from now on W-points) at the lower and upper surfaces. The indexing is carried out with i-indices in eastern ($\mathcal{X}$-) direction, with j-indices in northern ($\mathcal{Y}$-) direction and with k-indices in upward (z-)

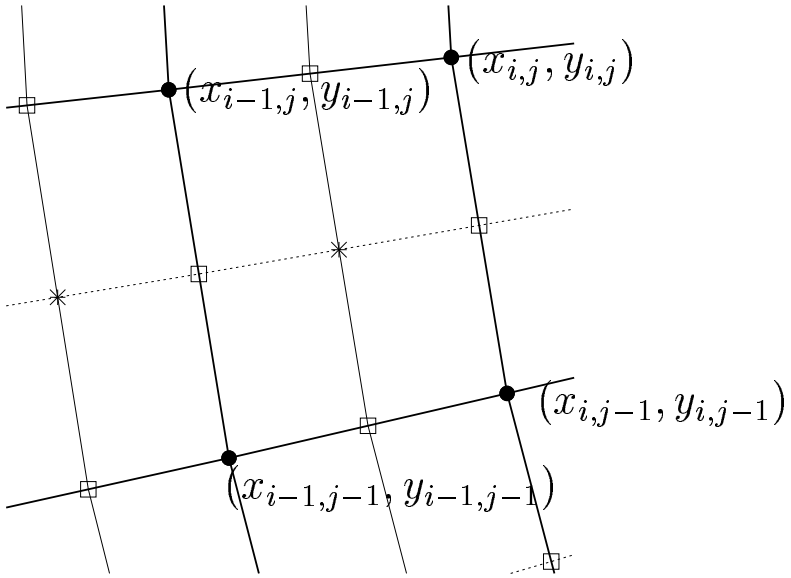

Figure 4.3: Grid layout and indexing of corner points for curvilinear grids.

direction, such that each grid point is identified by a triple (i, j, k). A T-point and the corresponding eastern U-point, the northern V-point and the above W-point have always the same index, see figures 4.2 and 4.4. The different grid points cover the following index ranges:

$$\begin{array}{lllll} \text{T-points:} & 1 \le i \le i_{\max}, & 1 \le j \le j_{\max}, & 1 \le k \le k_{\max} \\ \text{U-points:} & 0 \le i \le i_{\max}, & 1 \le j \le j_{\max}, & 1 \le k \le k_{\max} \\ \text{V-points:} & 1 \le i \le i_{\max}, & 0 \le j \le j_{\max}, & 1 \le k \le k_{\max} \\ \text{W-points:} & 1 \le i \le i_{\max}, & 1 \le j \le j_{\max}, & 0 \le k \le k_{\max} \end{array} \tag{4.18}$$

On the T-points, all tracers such as temperature T, salinity S, the general tracers c^i and the density are located. All turbulent quantities such as eddy viscosity ν_t and eddy diffusivity ν_t' are located on the W-points.

For curvilinear grids, several arrays for spatial increments Δx and Δy have to be defined:

$$
\begin{aligned}
\Delta x^c_{i,j} &= \left|\left|\tfrac{1}{2}(X_{i,j-1} + X_{i,j} - X_{i-1,j-1} - X_{i-1,j})\right|\right| \\
\Delta x^u_{i,j} &= \left|\left|\tfrac{1}{4}(X_{i+1,j-1} + X_{i+1,j} - X_{i-1,j-1} - X_{i-1,j})\right|\right| \\
\Delta x^v_{i,j} &= ||X_{i,j} - X_{i-1,j}|| \\
\Delta x^+_{i,j} &= \left|\left|\tfrac{1}{2}(X_{i+1,j} - X_{i-1,j})\right|\right| \\
\Delta y^c_{i,j} &= \left|\left|\tfrac{1}{2}(X_{i-1,j} + X_{i,j} - X_{i-1,j-1} - X_{i,j-1})\right|\right| \\
\Delta y^u_{i,j} &= ||X_{i,j} - X_{i,j-1}|| \\
\Delta y^v_{i,j} &= \left|\left|\tfrac{1}{4}(X_{i-1,j+1} + X_{i,j+1} - X_{i-1,j-1} - X_{i,j-1})\right|\right| \\
\Delta y^+_{i,j} &= \left|\left|\tfrac{1}{2}(X_{i,j+1} - X_{i,j-1})\right|\right|
\end{aligned}
\tag{4.19}
$$

where $||X_{i,j} - X_{i-1,j}|| = ((x_{i,j} - x_{i-1,j})^2 + (y_{i,j} - y_{i-1,j})^2)^{1/2}$. The superscripts $c, u, v, +$ in (4.19) indicate whether a Δx or Δy is centrered at a T-, U-, V-, or X-point, respectively. For the locations of the corner points $X_{i,j} = (x_{i,j}, y_{i,j})$, see figure 4.3.

4.4 Lateral boundary conditions

Usually, a land mask is defined on the horizontal numerical grid. This mask is denoted by a^z for T-points, a^u for U-points and a^v for V-points with a^z, a^u, and a^v being integer fields. A T-point is either a land point ($a^z = 0$) or a water point ($a^z > 0$). All U- and V-points surrounding a land point are defined as closed boundary and masked out: $a^u = 0$ and $a^v = 0$. The velocities on such closed boundaries are always set to 0.
Open boundaries are defined by $a^z > 1$ for T-points. Forced boundary points are marked by $a^z = 2$ and passive boundary points by $a^z = 3$. All other T-points are characterised by $a^z = 1$. For velocity points, three different types are defined at the open boundaries. U-points are classified by $a^u = 3$ if both the T-points east and west are open boundary points and by $a^u = 2$ if one adjacent T-point is an open boundary point and the other an open water point with $a^z = 1$. The same is carried out for V-points: They are classified by $a^v = 3$ if both the T-points south and north are open boundary points and by $a^v = 2$ if one adjacent T-point is an open boundary

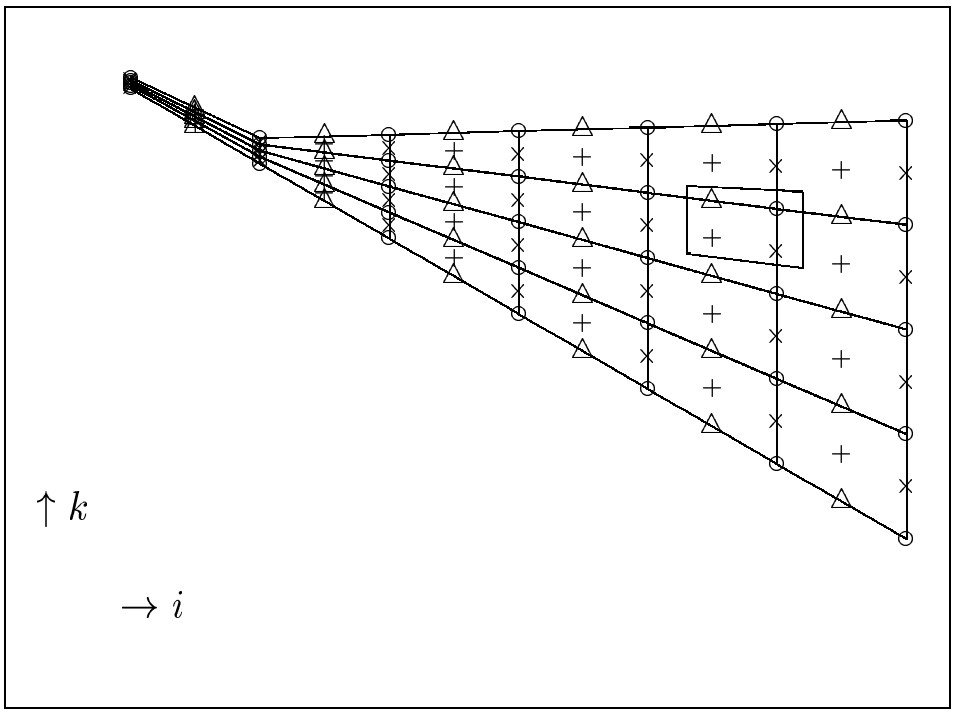

Figure 4.4: Layout of the model vertical model grid through the U-points. Shown are the reference boxes for the T-points. The following symbols are used: +: T-points; ×: U-points; △: W-points; ∘: X^u-points. The inserted box denotes grid points with the same index (i, k). The grid in the (j, k)-plane through the V-points is equivalent.

point and the other an open water point with $a^z = 1$. U-points which are adjacent to T-points with $a^z = 2$ and which are not denoted by $a^u = 2$ or $a^u = 3$ are the external U-points and are denoted by $a^u = 4$. The same holds for V-points: Those which are adjacent to T-points with $a^z = 2$ and which are not denoted by $a^v = 2$ or $a^v = 3$ are the external V-points and are denoted by $a^v = 4$.

For a simple example of grid point classification, see figure 4.5.

When the barotropic boundary forcing is carried out by means of prescribed surface elevations only, then the surface elevation ζ is prescribed in all T-points with $a^z = 2$. For passive boundary conditions ($a^z = 3$), where the curvature of the surface elevation is zero normal to the boundary, the surface slope is simply extrapolated to the boundary points. For a boundary point (i, j) at the western boundary this results e.g. in the following calculation for the boundary point:

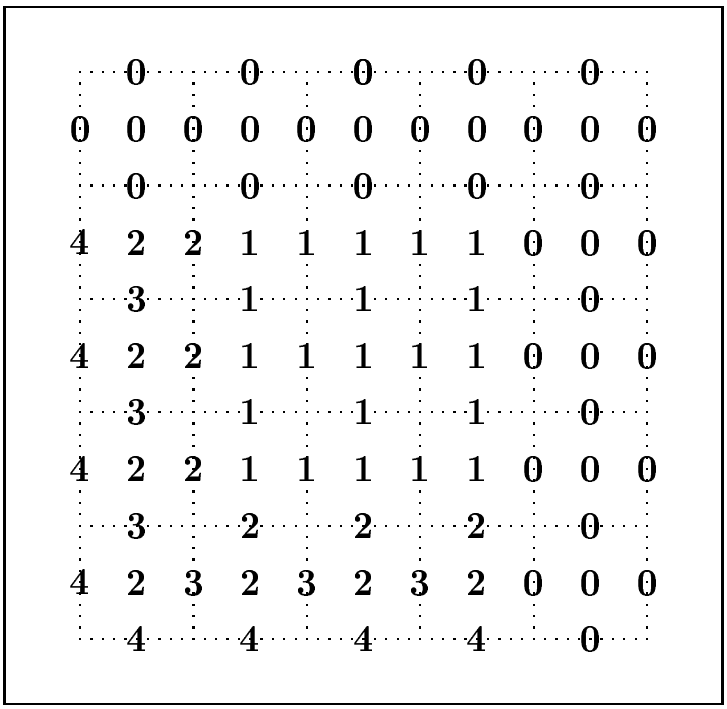

Figure 4.5: Classification of grid points for a simple 5×5 configuration ($i_{\max} = j_{\max} = 5$). On the locations for T-, U- and V-points, the values of a^z, a^u, and a^v, respectively, are written. The northern and eastern boundaries are closed and the western and southern boundaries are open and forced.

$$\zeta_{i,j} = \zeta_{i+1,j} + (\zeta_{i+1,j} - \zeta_{i+2,j}) = 2\zeta_{i+1,j} - \zeta_{i+2,j}. \tag{4.20}$$

4.5 Bed friction

As already mentioned earlier in section 2.1.3, caution is needed when discretising the bottom boundary conditions for momentum, (2.8). They are an example for a physical condition which has to be modified for the numerical discretisation, since the discrete velocity point nearest to the bottom is half a grid box away from the point where the boundary condition is defined. Furthermore, due to the logarithmic law, high velocity gradients are typical near the bed. Simply setting the discrete bottom velocity to zero, would therefore lead to large discretisation errors. Instead, a flux condition using bottom stresses is derived from the law of the wall, see e.g.

Burchard [2001c].
For the determination of the normalised bottom stresses

$$\frac{\tau_b^x}{\rho_0} = u_*^{bx} u_*^b, \tag{4.21}$$

$$\frac{\tau_b^y}{\rho_0} = u_*^{by} u_*^b \tag{4.22}$$

with the friction velocities $u_*^b = \sqrt{\tau_b/\rho_0}$ with $\tau_b = \sqrt{(\tau_b^x)^2 + (\tau_b^y)^2}$, assumptions about the structure of velocity inside the discrete bottom layer have to be made. We use here the logarithmic profile

$$\frac{u(z')}{u_*} = \frac{1}{\kappa} \ln\left(\frac{z' + z_0^b}{z_0^b}\right), \tag{4.23}$$

with the bottom roughness length z_0^b, the von Kármán constant $\kappa = 0.4$ and the distance from the bed, z'. Therefore, estimates for the velocities in the centre of the bottom layer can be achieved by:

$$u_b = \frac{u_*^{bx}}{\kappa} \ln\left(\frac{0.5h_1 + z_0^b}{z_0^b}\right), \tag{4.24}$$

$$v_b = \frac{u_*^{by}}{\kappa} \ln\left(\frac{0.5h_1 + z_0^b}{z_0^b}\right). \tag{4.25}$$

For $h_1 \to 0$, the original Dirichlet-type no-slip boundary conditions (2.8) are retained. Another possibility would be to specify the bottom velocities u_b and v_b such that they are equal to the layer-averaged log-law velocities (see *Baumert et al.* [1989], *Baumert and Radach* [1992]). The calculation of this is however slightly more time consuming and does not lead to a higher accuracy.
The roughness length at the bottom, z_0^b has to be defined. This is done here as follows (see e.g. *Kagan* [1995]):

$$z_0^b = 0.1 \frac{\nu}{u_*^b} + 0.03 h_0^b. \tag{4.26}$$

with the molecular viscosity ν, the friction velocity u_*^b and the height of the bottom roughness elements, h_0^b. The formula (4.26) interpolates between the limits of completely smooth ($h_0^b = 0$) and completely rough bottom ($h_0^b \gg \nu/u_*^b$). Since u_*^b is a function of the roughness length itself, equations (4.24), (4.25) and (4.26) are implicit and have to be iterated. In GETM, generally, two iterations per time step are used.

4.6 Continuity equation

The continuity equation in curvilinear coordinates must be discretised as follows:

$$\begin{aligned}\frac{\hat{h}_{i,j,k} - h_{i,j,k}}{\Delta t} = \\ -\frac{p_{i,j,k}\Delta y^u_{i,j} - p_{i-1,j,k}\Delta y^u_{i-1,j}}{\Delta x^c_{i,j}\Delta y^c_{i,j}} - \frac{q_{i,j,k}\Delta x^v_{i,j} - q_{i,j-1,k}\Delta x^v_{i,j-1}}{\Delta x^c_{i,j}\Delta y^c_{i,j}} \\ -w_{i,j,k} + w_{i,j,k-1}\end{aligned} \tag{4.27}$$

The discrete equation (4.27) will be used for the calculation of the grid-related vertical velocity $w_{i,j,k}$ for $k = 1, \ldots, N$ with $w_{i,j,0} = 0$.
The surface elevation equation (vertical sum of (3.26)) is then discretised in the following way:

$$\frac{\hat{\zeta}_{i,j} - \zeta_{i,j}}{\Delta t} = -\frac{U_{i,j}\Delta y^u_{i,j} - U_{i-1,j}\Delta y^u_{i-1,j}}{\Delta x^c_{i,j}\Delta y^c_{i,j}} - \frac{V_{i,j}\Delta x^v_{i,j} - V_{i,j-1}\Delta x^v_{i,j-1}}{\Delta x^c_{i,j}\Delta y^c_{i,j}} \tag{4.28}$$

4.7 Momentum and tracer advection and diffusion

4.7.1 Momentum advection

For the discretisation of the momentum advection terms, two conceptionally different methods have been implemented in GETM. The first is the straight-forward multidimensional advection scheme, which is here realised as the first-order upwind scheme, see section 4.7.1.1.

In order to make use of the higher-order directional-split methods for tracers (see section 4.7.5), an alternative method is implemented, in which the complete advection step is first made, and then the resulting advection terms, which are needed for the calculation of the slow terms, see equations (2.20) and (2.21)) are calculated from this (see section 4.7.1.2).

4.7.1.1 Multidimensional approach

The advective terms in the momentum equation are discretised in a momentum-conservative form. This is carried out here for the advective terms in the u-equation (3.27) and the v-equation (3.28) (after multiplying these equations with mn).
First advection term in (3.27):

$$\left(mn\,\partial_{\mathcal{X}}\left(\frac{u_k p_k}{n}\right)\right)_{i,j,k} \approx \frac{\frac{1}{2}(p_{i+1,j,k}+p_{i,j,k})\tilde{u}_{i+1,j,k}\Delta y^c_{i+1,j} - \frac{1}{2}(p_{i,j,k}+p_{i-1,j,k})\tilde{u}_{i,j,k}\Delta y^c_{i,j}}{\Delta x^u_{i,j}\Delta y^u_{i,j}} \tag{4.29}$$

For an upwind scheme, the inter-facial velocities which are defined on T-points are here calculated as:

$$\tilde{u}_{i,j,k} = \begin{cases} u_{i-1,j,k} & \text{for } \frac{1}{2}(p_{i,j,k}+p_{i-1,j,k}) > 0 \\ u_{i,j,k} & \text{else.} \end{cases} \tag{4.30}$$

Second advection term in (3.27):

$$\left(mn\,\partial_{\mathcal{Y}}y\left(\frac{v_k p_k}{m}\right)\right)_{i,j,k} \approx \frac{\frac{1}{2}(q_{i+1,j,k}+q_{i,j,k})\tilde{u}_{i,j,k}\Delta x^+_{i,j} - \frac{1}{2}(q_{i+1,j-1,k}+q_{i,j-1,k})\tilde{u}_{i,j-1,k}\Delta x^+_{i,j-1}}{\Delta x^u_{i,j}\Delta y^u_{i,j}} \tag{4.31}$$

For an upwind scheme, the inter-facial velocities which are defined on X-points are here calculated as:

$$\tilde{u}_{i,j,k} = \begin{cases} u_{i,j,k} & \text{for } \frac{1}{2}(q_{i+1,j,k}+q_{i,j,k}) > 0 \\ u_{i,j+1,k} & \text{else.} \end{cases} \tag{4.32}$$

First advection term in (3.28):

$$\left(mn\,\partial_{\mathcal{X}}\left(\frac{v_k q_k}{n}\right)\right)_{i,j,k} \approx \frac{\frac{1}{2}(p_{i,j+1,k}+p_{i,j,k})\tilde{v}_{i,j,k}\Delta y^{+}_{i,j} - \frac{1}{2}(p_{i-1,j+1,k}+p_{i-1,j,k})\tilde{v}_{i-1,j,k}\Delta y^{+}_{i-1,j}}{\Delta x^{v}_{i,j}\Delta y^{v}_{i,j}} \tag{4.33}$$

For an upwind scheme, the interfacial velocities which are defined on X-points are here calculated as:

$$\tilde{v}_{i,j,k} = \begin{cases} v_{i,j,k} & \text{for } \frac{1}{2}(p_{i+1,j,k}+p_{i,j,k}) > 0 \\ v_{i+1,j,k} & \text{else.} \end{cases} \tag{4.34}$$

Second advection term in (3.28):

$$\left(mn\,\partial_{\mathcal{Y}}\left(\frac{v_k q_k}{m}\right)\right)_{i,j,k} \approx \frac{\frac{1}{2}(q_{i,j+1,k}+q_{i,j,k})\tilde{v}_{i,j+1,k}\Delta x^{c}_{i,j+1} - \frac{1}{2}(q_{i,j,k}+q_{i,j-1,k})\tilde{v}_{i,j,k}\Delta x^{c}_{i,j}}{\Delta x^{v}_{i,j}\Delta y^{v}_{i,j}} \tag{4.35}$$

For an upwind scheme, the interfacial velocities which are defined on T-points are here calculated as:

$$\tilde{v}_{i,j,k} = \begin{cases} v_{i,j-1,k} & \text{for } \frac{1}{2}(q_{i,j,k}+q_{i,j-1,k}) > 0 \\ v_{i,j,k} & \text{else.} \end{cases} \tag{4.36}$$

The same schemes for horizontal advection are used for the vertically integrated advection terms in equations (2.16) and (2.17), the slow advection terms S^x_A and S^y_A and their transformations to curvilinear coordinates.
The vertical advection terms in equations (3.27) and (3.28) can be discretised in an upstream scheme as well.
Vertical advective flux in (3.27):

$$(\bar{w}_k\tilde{u}_k)_{i,j} \approx \frac{1}{2}(w_{i+1,j,k}+w_{i,j,k})\tilde{u}_{i,j,k} \tag{4.37}$$

with

$$\tilde{u}_{i,j,k} = \begin{cases} u_{i,j,k} & \text{for } \frac{1}{2}(w_{i+1,j,k} + w_{i,j,k}) > 0, \\ u_{i,j,k+1} & \text{else.} \end{cases} \tag{4.38}$$

Vertical advective flux in (3.28):

$$(\bar{w}_k \tilde{v}_k)_{i,j} \approx \frac{1}{2}(w_{i,j+1,k} + w_{i,j,k})\tilde{v}_{i,j,k} \tag{4.39}$$

with

$$\tilde{v}_{i,j,k} = \begin{cases} v_{i,j,k} & \text{for } \frac{1}{2}(w_{i,j+1,k} + w_{i,j,k}) > 0, \\ v_{i,j,k+1} & \text{else.} \end{cases} \tag{4.40}$$

4.7.1.2 Directional-split approach

Multidimensional treatment of advective terms in three-dimensional models is often quite unhandy, especially when higher-order advection schemes are needed. On the other hand, directional-split methods (which update the advected fields in each directional step and then "forget" the advection terms) as discussed in section 4.7.5, cannot directly be used for momentum advection when the models are based on mode splitting as e.g. GETM. The reason for this is that the three-dimensional advection terms are also needed for calculating the slow terms of the barotropic (external) mode, see equations (2.20) and (2.21).
The procedure suggested here is as follows. First, the pure momentum advection equations are formally solved with the directional-split method described in section 4.7.5:

$$\partial_t p_k + \partial_x(u_k p_k) + \partial_y(v_k p_k) + \bar{w}_k \tilde{u}_k - \bar{w}_{k-1}\tilde{u}_{k-1} = 0, \tag{4.41}$$

$$\partial_t q_k + \partial_x(u_k q_k) + \partial_y(v_k q_k) + \bar{w}_k \tilde{v}_k - \bar{w}_{k-1}\tilde{v}_{k-1} = 0. \tag{4.42}$$

The new solutions $\hat{p}_{i,j,k}$ and $\hat{q}_{i,j,k}$ are however not further used, but instead the resulting advective terms $-(\hat{p}_{i,j,k} - p_{i,j,k})/\Delta t$ and $-(\hat{q}_{i,j,k} - q_{i,j,k})/\Delta t$ are later applied to the momentum equations (together with other processes such as horizontal diffusion, pressure gradients, etc.) and also used for the calculation of the slow terms in (2.20) and (2.21).

With this method, all higher-order directional-split advection schemes are now available for the momentum advection. The advective fluxes needed for this have to be averaged from the conservative advective fluxes resulting from the continuity equation (4.27). Continuity will still be retained due to the linearity of the continuity equation.

4.7.2 Horizontal momentum diffusion

The horizontal diffusion terms are discretised in momentum-conserving form as well. For simplicity, this shown here for these terms as they appear in equations (3.27) and (3.28), i.e. without multiplying them by mn.
First horizontal diffusion term in (3.27):

$$\partial_{\mathcal{X}} \left(\frac{2A_M h_k}{n} m \partial_{\mathcal{X}} u_k \right)_{i,j,k} \approx$$

$$2A^M_{i+1,j,k} \Delta y^c_{i+1,j} h^c_{i+1,j,k} \frac{u_{i+1,j,k} - u_{i,j,k}}{\Delta x^c_{i+1,j}} - 2A^M_{i,j,k} \Delta y^c_{i,j} h^c_{i,j,k} \frac{u_{i,j,k} - u_{i-1,j,k}}{\Delta x^c_{i,j}} \tag{4.43}$$

Second horizontal diffusion term in (3.27):

$$\begin{aligned}
&\partial_{\mathcal{Y}} \left(\frac{A_M h_k}{m} (n \partial_{\mathcal{Y}} u_k + m \partial_{\mathcal{X}} v_k) \right)_{i,j,k} \approx \\
&\quad \frac{1}{4} \left(A^M_{i+1,j+1,k} + A^M_{i,j+1,k} + A^M_{i,j,k} + A^M_{i+1,j,k} \right) h^+_{i,j,k} \Delta x^+_{i,j} \\
&\quad \times \left(\frac{u_{i,j+1,k} - u_{i,j,k}}{\Delta y^+_{i,j}} - \frac{v_{i+1,j,k} - v_{i,j,k}}{\Delta x^+_{i,j}} \right) \\
&\quad -\frac{1}{4} \left(A^M_{i+1,j,k} + A^M_{i,j,k} + A^M_{i,j-1,k} + A^M_{i+1,j-1,k} \right) h^+_{i,j-1,k} \Delta x^+_{i,j-1} \\
&\quad \times \left(\frac{u_{i,j,k} - u_{i,j-1,k}}{\Delta y^+_{i,j-1}} - \frac{v_{i+1,j-1,k} - v_{i,j-1,k}}{\Delta x^+_{i,j-1}} \right)
\end{aligned} \tag{4.44}$$

First horizontal diffusion term in (3.28):

$$\partial_{\mathcal{Y}}\left(\frac{2A_M h_k}{m} n \partial_{\mathcal{Y}} v_k\right)_{i,j,k} \approx$$

$$2A^M_{i,j+1,k}\Delta x^c_{i,j+1} h^c_{i,j+1,k} \frac{v_{i,j+1,k} - v_{i,j,k}}{\Delta y^c_{i,j+1}} - 2A^M_{i,j,k}\Delta x^c_{i,j} h^c_{i,j,k} \frac{v_{i,j,k} - v_{i,j-1,k}}{\Delta y^c_{i,j}} \tag{4.45}$$

Second horizontal diffusion term in (3.28):

$$\begin{aligned}
&\partial_{\mathcal{X}}\left(\frac{A_M h_k}{n}(n\partial_{\mathcal{Y}} u_k + m\partial_{\mathcal{X}} v_k)\right)_{i,j,k} \approx \\
&\frac{1}{4}\left(A^M_{i+1,j+1,k} + A^M_{i,j+1,k} + A^M_{i,j,k} + A^M_{i+1,j,k}\right) h^+_{i,j,k}\Delta x^+_{i,j} \\
&\times\left(\frac{u_{i,j+1,k} - u_{i,j,k}}{\Delta y^+_{i,j}} - \frac{v_{i+1,j,k} - v_{i,j,k}}{\Delta x^+_{i,j}}\right) \\
&-\frac{1}{4}\left(A^M_{i,j+1,k} + A^M_{i-1,j+1,k} + A^M_{i-1,j,k} + A^M_{i,j,k}\right) h^+_{i-1,j,k}\Delta x^+_{i-1,j} \\
&\times\left(\frac{u_{i-1,j+1,k} - u_{i-1,j,k}}{\Delta y^+_{i-1,j}} - \frac{v_{i,j,k} - v_{i-1,j,k}}{\Delta x^+_{i-1,j}}\right)
\end{aligned} \tag{4.46}$$

It is assumed here that the horizontal momentum diffusivities $A^M_{i,j,k}$ are located on the T-points.

4.7.3 Tracer advection

After multiplying (3.29) with mn, the advective terms in this equation are discretised as follows.
First advection term in (3.29):

$$\left(mn\,\partial_{\mathcal{X}}\left(\frac{p_k c_k}{n}\right)\right)_{i,j} \approx \frac{p_{i,j,k}\tilde{c}_{i,j,k}\Delta y^u_{i,j} - p_{i-1,j,k}\tilde{c}_{i-1,j,k}\Delta y^u_{i-1,j}}{\Delta x^c_{i,j}\Delta y^c_{i,j}} \tag{4.47}$$

Second advection term in (3.29):

$$\left(mn\,\partial_{\mathcal{Y}}\left(\frac{q_k c_k}{m}\right)\right)_{i,j} \approx \frac{q_{i,j,k}\tilde{c}_{i,j,k}\Delta y^v_{i,j} - q_{i,j-1,k}\tilde{c}_{i,j-1,k}\Delta y^v_{i,j-1}}{\Delta x^c_{i,j}\Delta y^c_{i,j}} \tag{4.48}$$

Vertical advective fluxes in (3.29):

$$\left(\bar{w}_k \tilde{c}_k\right)_{i,j} \approx w_{i,j,k}) \tilde{c}_{i,j,k}. \tag{4.49}$$

The interfacial concentrations $\tilde{c}_{i,j,k}$ are calculated according to upwind or higher order directional split schemes, which are discussed in detail in section 4.7.5.

4.7.4 Horizontal tracer diffusion

As for the horizontal momentum diffusion (see section 4.7.2, also here, the discretisation of the diffusion terms is shown here without multiplication with mn. Thus the diffusion terms in equation (3.29) are discretised as follows:
First horizontal diffusion term in (3.29):

$$\left(\partial_{\mathcal{X}} \left(\frac{A_k^T h_k}{n} m \partial_{\mathcal{X}} c_k\right)\right)_{i,j,k} \approx$$

$$\frac{1}{2}\left(A^T_{i+1,j,k} + A^T_{i,j,k}\right) h^u_{i,j,k} \Delta y^u_{i,j} \frac{c_{i+1,j,k} - c_{i,j,k}}{\Delta x^u_{i,j}} \tag{4.50}$$

$$-\frac{1}{2}\left(A^T_{i,j,k} + A^T_{i-1,j,k}\right) h^u_{i-1,j,k} \Delta y^u_{i-1,j} \frac{c_{i,j,k} - c_{i-1,j,k}}{\Delta x^u_{i-1,j}}$$

Second horizontal diffusion term in (3.29):

$$\left(\partial_{\mathcal{Y}} \left(\frac{A_k^T h_k}{m} n \partial_{\mathcal{Y}} c_k\right)\right)_{i,j,k} \approx$$

$$\frac{1}{2}\left(A^T_{i,j+1,k} + A^T_{i,j,k}\right) h^v_{i,j,k} \Delta x^v_{i,j} \frac{c_{i,j+1,k} - c_{i,j,k}}{\Delta y^v_{i,j}} \tag{4.51}$$

$$-\frac{1}{2}\left(A^T_{i,j,k} + A^T_{i,j-1,k}\right) h^v_{i,j-1,k} \Delta x^v_{i,j-1} \frac{c_{i,j,k} - c_{i,j-1,k}}{\Delta y^v_{i,j-1}}$$

4.7.5 Higher order advection schemes

For the advection of an active tracer such as temperature, salinity or any physically passive tracer such as oxygen concentration, the following properties are required to properly reproduce dynamics of such tracers:

- **Local mass conservation:** This is guaranteed by using the conservative formulation of the advective terms, see equation (2.27) and equations (4.52) and (4.69) below.
- **Positivity:** This property means that positive quantities stay positive during the advection operation. This is fulfilled when the numerical solution after each time step is within the range of the numerical solution before the time step. Total Variation Diminishing schemes have this property.
- **Low numerical diffusion:** The only linear and positive advection scheme is the first-order upwind scheme, which is known for high numerical diffusion which might smooth out all interesting details of the numerical solution and can therefore not be recommended for ocean models.
- **Low numerical dispersion:** Higher order linear models show numerical dispersion which leads to unphysical overshoots and undershoots relative to the physical solution. Thus positivity is easily violated.

During the last 20 years Total Variation Diminishing (TVD) advection schemes have been developed, which are now state-of-the-art in various ocean models. In the following, a numerical scheme is presented which is easy to implement in ocean models and which fulfils the requirements mentioned above. The idea for this implementation is adopted from *Pietrzak* [1998] who suggested the use of a directional split method applying a one-dimensional advection scheme alternately in all spatial directions. Here, some second-order and a third-order in space scheme with a slope limiter will be tested for simple one-dimensional test cases (see section 4.7.5.1), two-dimensional solid-body rotation (see section 4.7.5.2), a two-dimensional distortion test (see section 4.7.5.3). For a lock exchange test (see section 5.2) and for the advection of tracers through curvilinear coordinate grids, see section 5.1.3.
These high-order schemes should also be applied to the advection of momentum and turbulent quantities such as the turbulent kinetic energy, k, and the turbulent dissipation rate, ε. Since the continuity equation (3.14) as well as its discretised form (4.27) are linear, the conservative reference boxes can in principle be referred to any quantity by simply interpolating the transports around the reference box. For the momentum, this has been already implemented into GETM. Tests are performed in section 5.4 for a freshwater eddy and in section 6.1 for tidal currents in the Sylt-Rømø Bight. High-order momentum advection is further used for the Lake Constance simulation in section 6.2.
High-order advection for turbulent quantities will be implemented into GETM soon. One task would then be to point out scenarios in which the consideration of this additional process is relevant. It should be noted that advection of turbulent quantities

is generally neglected in three-dimensional modelling (for an exception see *Delhez et al.* [1999] who show that advection of turbulent quantities is not important in a shelf sea model).

4.7.5.1 One-dimensional experiments

In one spatial dimension, a general advection equation reads as

$$\partial_t \Psi + \partial_x (u\Psi) = 0 \tag{4.52}$$

with a tracer Ψ, and the velocity u which is here supposed to constant. It can be immediately seen that in this case, the analytical solution can be formulated as

$$\Psi(x,t) = \Psi(x - ut, 0) \tag{4.53}$$

for any tracer Ψ. For equidistant grid spacing, the discretisation of (4.52) is carried out using the following scheme:

$$\Psi_i^{n+1/2} = \Psi_i^n - \frac{\Delta t}{\Delta x}(F_{i+1/2}^n - F_{i-1/2}^n) \tag{4.54}$$

with the fluxes $F_{i+1/2}^n$ calculated in a upstream-biased way:

$$F_{i+1/2}^n = \frac{1}{\Delta t}\int_{x_{i+1/2}-u\Delta x}^{x_{i+1/2}} \Psi(x')\,dx'. \tag{4.55}$$

Since Ψ is known only on the discrete points x_i, it has to be interpolated between these points in order to carry out the integration in (4.55). For each interval $[x_{i-1/2}, x_{i+1/2}]$ this is done by deriving the polynomial $\tilde{\Psi}_i$ with

$$\int_{x_{i-1/2+k}}^{x_{i+1/2+k}} \tilde{\Psi}_i(x')\,dx' = \Psi_{i+k}, \quad k = -1, 0, 1, \tag{4.56}$$

see e.g. *Leonard* [1979] and *Pietrzak* [1998]. This polynomial scheme is of third-order accuracy in space and will here be denoted by P_2. The resulting scheme can be formulated in the following way:

$$F_{i+1/2} = \begin{cases} u_{i+1/2}\left(\Psi_i + \frac{1}{2}\Phi^+_{i+1/2}(1-|c_{i+1/2}|)(\Psi_{i+1}-\Psi_i)\right) & \text{for } u_{i+1/2} > 0, \\ u_{i+1/2}\left(\Psi_{i+1} + \frac{1}{2}\Phi^-_{i+1/2}(1-|c_{i+1/2}|)(\Psi_i-\Psi_{i+1})\right) & \text{else,} \end{cases} \tag{4.57}$$

with the Courant number $c_{i+1/2} = u_{i+1/2}\Delta t/\Delta x$ and

$$\Phi^+_{i+1/2} = \alpha_{i+1/2} + \beta_{i+1/2} r^+_{i+1/2}, \quad \Phi^-_{i+1/2} = \alpha_{i+1/2} + \beta_{i+1/2} r^-_{i+1/2}, \tag{4.58}$$

where

$$\alpha_{i+1/2} = \frac{1}{2} + \frac{1}{6}(1-2|c_{i+1/2}|), \quad \beta_{i+1/2} = \frac{1}{2} - \frac{1}{6}(1-2|c_{i+1/2}|), \tag{4.59}$$

and

$$r^+_{i+1/2} = \frac{\Psi_i - \Psi_{i-1}}{\Psi_{i+1} - \Psi_i}, \quad r^+_{i+1/2} = \frac{\Psi_{i+2} - \Psi_{i+1}}{\Psi_{i+1} - \Psi_i}. \tag{4.60}$$

It should be noted that by formulation (4.57) the P_2 scheme is cast into the so-called Lax-Wendroff form, which would be recovered for $\Phi^+_{i+1/2} = \Phi^-_{i+1/2} = 1$.
In order to obtain a monotonic and positive scheme, the factors $\Phi^+_{i+1/2}$ are limited in the following way:

$$\Phi^+_{i+1/2} \to \max\left[0, \min\left(\Phi^+_{i+1/2}, \frac{2}{1-|c_{i+1/2}|}, \frac{2r^+_{i+1/2}}{|c_{i+1/2}|}\right)\right], \tag{4.61}$$

and, equivalently, for $\Phi^-_{i+1/2}$. This so-called PDM-limiter has been described in detail by *Leonard* [1991], who named the PDM-limited P_2 scheme also ULTIMATE QUICKEST (quadratic upstream interpolation for convective kinematics with estimated stream terms).
A non-equidistant version of the P_2 scheme is also derived and tested here. Since this version can not easily be transformed into the Lax-Wendroff form, it will not be used together with the PDM limiter given by relation (4.61).

Some simpler limiters which do not exploit the third-order polynomial properties of the discretisation (4.57) have been listed by *Zalezak* [1987]. Among those are the MUSCL scheme by *van Leer* [1979],

$$\Phi^+_{i+1/2} \to \max\left[0, \min\left(2, 2r^+_{i+1/2}, \frac{1+r^+_{i+1/2}}{2}\right)\right], \tag{4.62}$$

and the Superbee scheme by *Roe* [1985],

$$\Phi^+_{i+1/2} \to \max\left[0, \min(1, 2r^+_{i+1/2}), \min(r^+_{i+1/2}, 2)\right]. \tag{4.63}$$

These two are included into the tests here, because they do in contrast to the P_2-PDM scheme not require substantially more computational effort on non-equidistant grids.
In the following, these schemes are tested by means of a simple one-dimensional test case with constant velocity. A periodic domain with length $L = 100$ m and velocity $u = 1\ \mathrm{m\,s^{-1}}$ is discretised in two ways, one equidistant and one non-equidistant method:

1. with time steps $\Delta t = 0.5$ s, 0.25 s and 0.125 s and spatial increments of $\Delta x = 100$ m, 50 m and 25 m, respectively, resulting for all cases in a Courant number of $c = 0.5$,

2. with time steps $\Delta t = 0.25$ s, 0.125 s and 0.0625 s and a non-equidistant grid-spacing given by

$$\Delta x_i = \frac{1.1 - \exp\left[-\left(1 - \frac{2i}{N}\right)^2\right]}{\sum_{i=1}^{N} \Delta x_i}, \tag{4.64}$$

   see figure 4.6 with $N = i_{\max} = j_{\max}$ being the number of horizontal grid boxes. This gives a maximum Courant number of $c = 0.88$ and the ratio of the smallest Δx_i to the largest Δx_i is 0.14.

The runtime is in all cases $T = 1200$ s, resulting in six complete revolutions through the periodic domain. With, (4.53), $\Psi(x, 0) = \Psi(x, T)$ for all initial distributions Ψ. Figure 4.7 shows initial and final values for two different initial distributions of Ψ, a rectangular distribution and a Gaussian bell distribution with the limited and

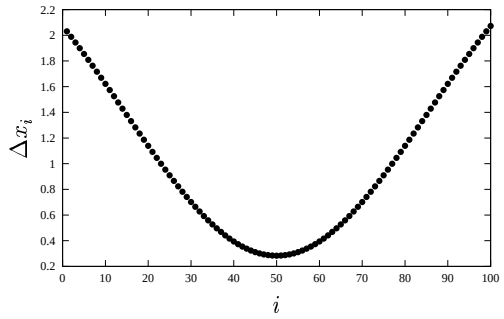

Figure 4.6: Non-equidistant grid spacing for the one-dimensional advection experiments.

the unlimited P_2 scheme for $\Delta x = 1$ m. The unlimited scheme has been advected with the equidistant and the non-equidistant grid, the limited scheme only with the equidistant grid. For the rectangular initial distribution, the unlimited scheme clearly shows the typical over- and undershoots which are removed when using the limited scheme. For the Gaussian bell case, no over- and undershoots are visible also for the unlimited scheme (but undershoots exist, see table 4.2), and the limited scheme underestimates the maximum slightly more than the unlimited scheme. On the non-equidistant grid, the accuracy of the P_2 scheme is considerably reduced.
Figure 4.8 shows some results for the MUSCL and Superbee limiters. Also here, no over- or undershoots appear. The Superbee limiter tends to increase smooth slopes, whereas the MUSCL limiter shows some numerical diffusion. The overall accuracy of the two schemes is however comparable, see tables 4.1 and 4.2. As expected, the performance of the schemes is reduced for non-equidistant grid-spacing.
It should be mentioned that the P_2-PDM scheme belongs to the class of so-called total variation diminishing (TVD) schemes with the total variation TV being defined as:

$$TV(\Psi^n) = \sum_{i=1}^{N} |\Psi i + 1^n - \Psi_i^n|. \tag{4.65}$$

The TVD property is thus defined as

$$TV(\Psi^{N+1}) \leq TV(\Psi^n). \tag{4.66}$$

In tables 4.1 and 4.2, some statistics of the unlimited and the limited scheme are shown for the three different spatial resolutions given above. The order of approximation of the schemes, $\mathcal{O}$ have been estimated empirically by the relation:

$$\mathcal{O}(\Delta x) \log_2 \left(\frac{L_2(\Delta x)}{L_2(\Delta x/2)} \right) \tag{4.67}$$

with the L_2 error defined as

$$L_2 = \sqrt{\sum_{i=1}^{N} \left(\Psi(i\Delta x, T) - \Psi_i^T\right)^2} \tag{4.68}$$

with Ψ_i^T representing the numerical solution at $t = T$. It can be seen that the unlimited and limited P_2 schemes are about third-order accurate for the Gaussian bell case and of lower than first order fort the rectangular case. The latter can be explained by the fact that the numerical scheme is not in the convergence range due to the fact that the analytical solution is not continuous.
It is interesting to note that the Superbee scheme which tend to over-emphasise smooth gradients is close to first order only for the Gaussian bell test case (see table 4.2) whereas the MUSCL limiter is (as expected) close to second order.

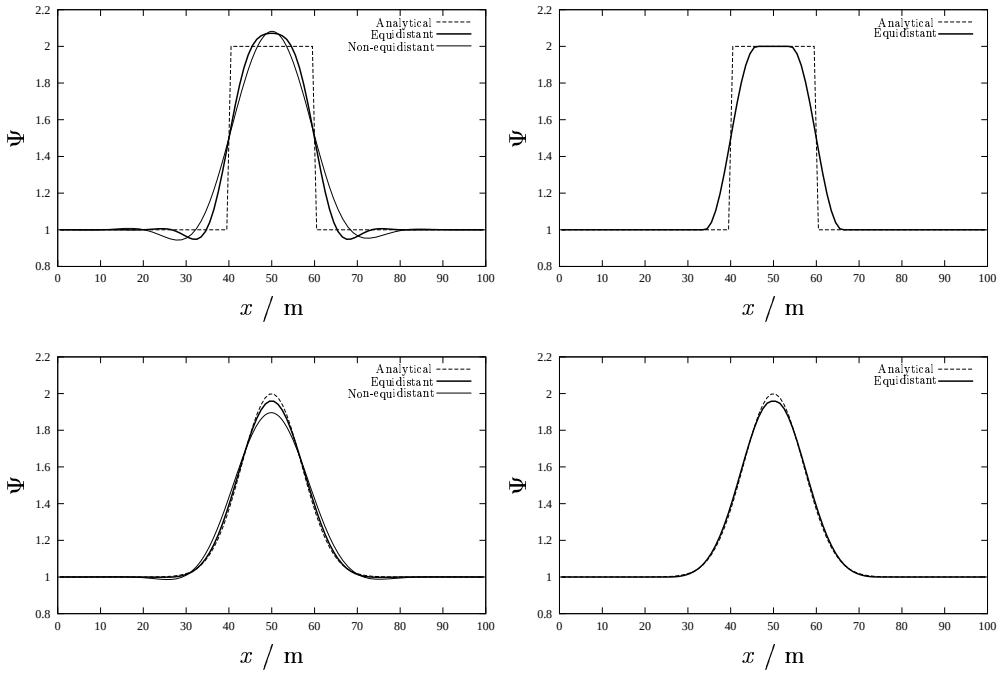

Figure 4.7: One-dimensional advection scheme test showing the analytical solution (dashed line) and the numerical approximation (bold line) after 6 revolutions through a periodic domain of length $L = 100$ m with $\Delta x = 1$ m and an advection speed of u m s^{-1}. The Courant number was $c = 0.5$ for the equidistant grid-spacing and the maximum Courant number was $c = 0.88$ for the non-equidistant grid-spacing. Upper panels: rectangular initial distribution; lower panels: Gaussian initial distribution. The two left panels show results obtained with the unlimited P_2 scheme, the left two panels show results for the P_2-PDM scheme.

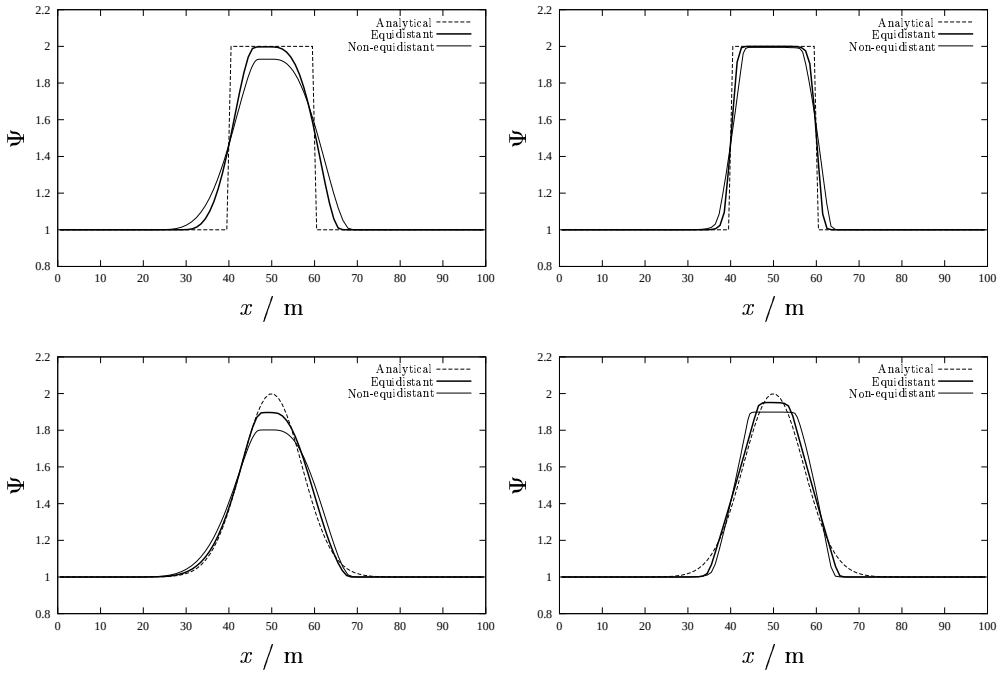

Figure 4.8: One-dimensional advection scheme test showing the analytical solution (dashed line) and the numerical approximation (bold line) after 6 revolutions through a periodic domain of length $L = 100$ m with $\Delta x = 1$ m and an advection speed of u m s^{-1}. The Courant number was $c = 0.5$ for the equidistant grid-spacing and the maximum Courant number was $c = 0.88$ for the non-equidistant grid-spacing. Upper panels: rectangular initial distribution; lower panels: Gaussian initial distribution. The two left panels show results obtained with the MUSCL limiter, the left two panels with the Superbee limiter.

Scheme	N	Min	Max	TV/TV$_0$	L_2 error	$\mathcal{O}$
P_2, eq.	100	0.945	2.071	1.185	0.1207	–
P_2, eq.	200	0.948	2.052	1.230	0.0926	0.382
P_2, eq.	400	0.948	2.052	1.234	0.0715	0.373
P_2, non-eq.	100	0.944	2.082	1.197	0.1654	–
P_2, non-eq.	200	0.943	2.056	1.175	0.1313	0.333
P_2, non-eq.	400	0.943	2.057	1.231	0.1004	0.387
MUSCL, non-eq.	100	1.000	1.930	0.930	0.1750	–
MUSCL, non-eq.	200	1.000	2.000	1.000	0.1355	0.369
MUSCL, non-eq.	400	1.000	2.000	1.000	0.1060	0.354
MUSCL, eq.	100	1.000	2.000	1.000	0.1163	–
MUSCL, eq.	200	1.000	2.000	1.000	0.0898	0.366
MUSCL, eq.	400	1.000	2.000	1.000	0.0693	0.374
Superbee, eq.	100	1.000	2.000	1.000	0.0706	–
Superbee, eq.	200	1.000	2.000	1.000	0.0499	0.500
Superbee, eq.	400	1.000	2.000	1.000	0.0353	0.499
Superbee, non-eq.	100	1.000	1.995	0.995	0.1155	–
Superbee, non-eq.	200	1.000	2.000	1.000	0.0836	0.466
Superbee, non-eq.	400	1.000	2.000	1.000	0.0600	0.479
P_2-PDM	100	1.000	2.000	1.000	0.1157	–
P_2-PDM	200	1.000	2.000	1.000	0.0894	0.372
P_2-PDM	400	1.000	2.000	1.000	0.0697	0.359

Table 4.1: Absolute minima (Min) and maxima (Max), total variation of final profile normalised by initial total variation (TV/TV$_0$), L_2 error and empirically estimated order of approximation for the unlimited P_2 scheme, the MUSCL and Superbee limiters and the limited P_2-PDM scheme for the one-dimensional rectangle test case.

Scheme	N	Min	Max	TV/TV$_0$	L_2 error	$\mathcal{O}$
P_2, eq.	100	0.9995	1.9692	0.9727	0.008998	–
P_2, eq.	200	1.0000	1.9953	0.9959	0.001252	2.845
P_2, eq.	400	1.0000	1.9993	0.9997	0.000159	2.977
P_2, non-eq.	100	0.9862	1.8958	0.9234	0.050936	–
P_2, non-eq.	200	1.0000	1.9797	0.9800	0.009489	2.424
P_2, non-eq.	400	1.0000	1.9972	0.9972	0.001294	2.874
MUSCL, eq.	100	1.0000	1.9176	0.9199	0.017673	–
MUSCL, eq.	200	1.0000	1.9741	0.9747	0.003821	2.210
MUSCL, eq.	400	1.0000	1.9918	0.9920	0.000918	1.963
MUSCL, non-eq.	100	1.0000	1.8020	0.8018	0.087883	–
MUSCL, non-eq.	200	1.0000	1.9274	0.9274	0.029930	1.554
MUSCL, non-eq.	400	1.0000	1.9758	0.9758	0.009787	1.613
Superbee, eq.	100	1.0000	1.9544	0.9568	0.025891	–
Superbee, eq.	200	1.0000	1.9919	0.9925	0.013184	0.974
Superbee, eq.	400	1.0000	1.9987	0.9988	0.005833	1.176
Superbee, non-eq.	100	1.0000	1.8991	0.8992	0.069613	–
Superbee, non-eq.	200	1.0000	1.9706	0.9707	0.026591	0.974
Superbee, non-eq.	400	1.0000	1.9960	0.9960	0.013753	1.176
P_2-PDM	100	1.0000	1.9585	0.9609	0.010188	–
P_2-PDM	200	1.0000	1.9917	0.9923	0.001425	2.838
P_2-PDM	400	1.0000	1.9982	0.9984	0.000198	2.850

Table 4.2: Absolute minima (Min) and maxima (Max), total variation of final profile normalised by initial total variation (TV/TV$_0$), L_2 error and empirically estimated order of approximation for the unlimited P_2 scheme, the MUSCL and Superbee limiters and the limited P_2-PDM scheme for the one-dimensional Gaussian bell test case.

4.7.5.2 Two-dimensional solid-body rotation

Here it is shown, how the above described unlimited and limited P_2 schemes and the MUSCL and Superbee schemes can be used for numerically solving a two-dimensional problem:

$$\partial_t \Psi + \partial_x(u\Psi) + \partial_y(v\Psi) = 0 \tag{4.69}$$

For constant and non-divergent flow, a simple split scheme is applied alternately in the x- and in the y-direction:

$$\Psi_{i,j}^{n+1/2} = \Psi_{i,j}^{n} - \frac{\Delta t}{\Delta x}(F_{i+1/2,j}^{n} - F_{i-1/2,j}^{n}), \tag{4.70}$$

$$\Psi_{i,j}^{n+1} = \Psi_{i,j}^{n+1/2} - \frac{\Delta t}{\Delta y}(F_{i,j+1/2}^{n} - F_{i,j-1/2}^{n}) \tag{4.71}$$

The fluxes $F_{i+1/2,j}^{n}$ and $F_{i,j+1/2}^{n}$ have been calculated according to the schemes described in section 4.7.5.1. It has been assumed here that the flow is non-divergent in each direction (for the more general, divergent case, see section 4.7.5.3),

$$u_{i,j} - u_{i-1,j} = 0, \quad v_{i,j} - v_{i,j-1} = 0. \tag{4.72}$$

Following *Pietrzak* [1998], the test case investigated here is a solid-body rotation on a square domain of size $L_x = L_y = 100$ m given by th velocity field

$$u = -\omega(y - y_0), \quad v = \omega(x - x_0) \tag{4.73}$$

with $(x_0, y_0) = (50\text{ m}, 50\text{ m})$ and the angular velocity $\omega = 0.1\text{ s}^{-1}$. With temporal and spatial resolutions of $\Delta t = 0.1$ s, 0.05 s and 0.025 s and $\Delta x = \Delta y = 1$ m, 0.5 m and 0.25 m, respectively, the maximum Courant number is about $c = 0.7$. The two initial fields, a cube and a Gaussian bell are shown in figure 4.9. One full revolution is finished after $t = T = 20\pi$ s. The numerical results for $\Delta x = \Delta y = 1$ m are graphically displayed in figures 4.10 and 4.11 for the unlimited and the limited P_2 scheme. Some statistics are given in tables 4.3 and 4.4. In comparison to the one-dimensional case, some striking differences occur: The limited schemes are not any longer TVD, although still monotone. The loss of the TVD property has been formulated by *Goodman and LeVeque* [1985] as a theorem:

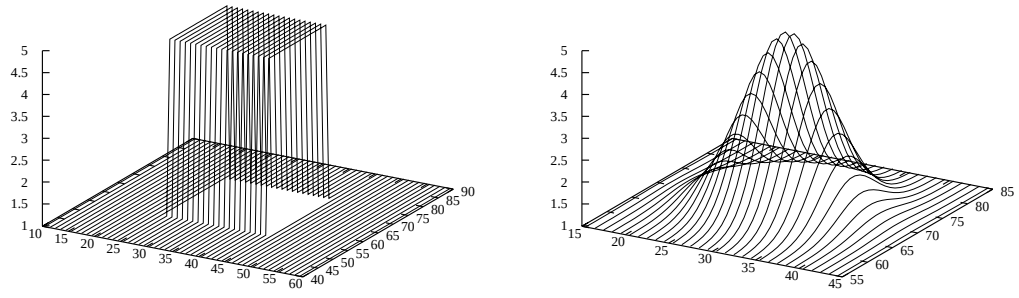

Figure 4.9: Initial conditions for solid-body rotation test. Left: cube; right: Gaussian bell.

> Except in certain trivial cases, any method that is TVD in two space dimensions is at most first order accurate.

This has the implication, that higher order schemes cannot be TVD. The order of the schemes is again empirically assessed for this two-dimensional case, see tables 4.3 and 4.4. For the continuous Gaussian bell case, the empirical order is about 2 when stepping from $\Delta x = 1$ m to $\Delta x = 0.5$ m which could be explained by the splitting applied. It is however obscure, why the accuracy decreases rapidly to below 1 when stepping from $\Delta x = 0.5$ m to $\Delta x = 0.25$ m. This has to be further investigated.
A pseudo-two-dimensional scheme is obtained, when the calculation of the fluxes $F_{i,j-1/2}$ and $F_{i,j+1/2}$ in the discrete advection equation (4.71) would not be based on the intermediate concentrations $\Psi_{i,j}^{n+1/2}$ but on the old concentrations $\Psi_{i,j}^{n}$. The consequences of such a method for the P_2-PDM scheme are shown in figure 4.14. The visible distortions are due to the missing cross-diagonal terms and can only be avoided by using fully two-dimensional schemes such as the UTOPIA scheme discussed in section 4.7.5.3.

4.7.5.3 Two-dimensional linear distortion

In contrast to section 4.7.5.1, here the divergence is non-zero in each individual dimension. This has the consequence that an intermediate amplification factor is needed which is generally not unity. Thus a continuity equation is calculated in parallel to the advection equation. This amplification factor which can be regarded as a height or depth will be denoted by D and is multiplied on the concentration in order to achieve full concentration conservation:

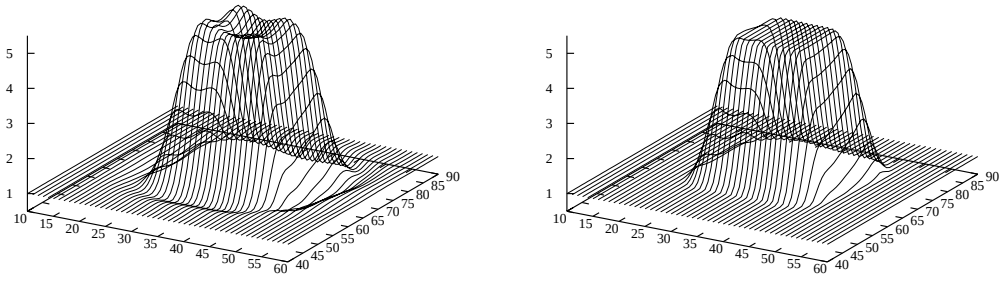

Figure 4.10: Cube resulting after one solid-body rotation with $\Delta x = \Delta y = 1$ m and a Courant number of $c = 0.5$. Left: unlimited P_2 scheme; right: limited P_2-PDM scheme.

$$\partial_t(D\Psi) + \partial_x(uD\Psi) + \partial_y(vD\Psi) = 0 \tag{4.74}$$

$$\partial_t D + \partial_x(uD) + \partial_y(vD) = 0 \tag{4.75}$$

For the set of equations consisting of (4.74) and (4.75), four numerical schemes are suggested:

1.: The split scheme according to *Pietrzak* [1998]:

$$D_{i,j}^{n+1/2}\Psi_{i,j}^{n+1/2} = D_{i,j}^{n}\Psi_{i,j}^{n} - \frac{\Delta t}{\Delta x}(D_{i+1/2,j}^{n}F_{i+1/2,j}^{n} - D_{i-1/2,j}^{n}F_{i-1/2,j}^{n}) \tag{4.76}$$

$$D_{i,j}^{n+1}\Psi_{i,j}^{n+1} = D_{i,j}^{n+1/2}\Psi_{i,j}^{n+1/2} - \frac{\Delta t}{\Delta y}(D_{i,j+1/2}^{n}F_{i,j+1/2}^{n} - D_{i,j-1/2}^{n}F_{i,j-1/2}^{n}) \tag{4.77}$$

with

$$D_{i,j}^{n+1/2} = D_{i,j}^{n} - \frac{\Delta t}{\Delta x}(U_{i+1/2,j}^{n} - U_{i-1/2,j}^{n}) \tag{4.78}$$

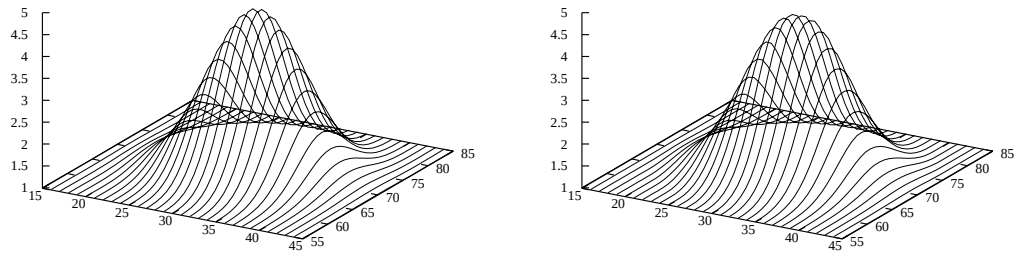

Figure 4.11: Gaussian bell resulting after one solid-body rotation with $\Delta x = \Delta y = 1$ m and a Courant number of $c = 0.5$. Left: unlimited P_2 scheme; right: limited P_2-PDM scheme.

and thus

$$D_{i,j}^{n+1} = D_{i,j}^{n+1/2} - \frac{\Delta t}{\Delta y}(V_{i,j+1/2}^{n} - V_{i,j-1/2}^{n}). \tag{4.79}$$

with

$$U_{i+1/2,j}^{n} = D_{i+1/2,j}^{n} u_{i+1/2,j}^{n} \tag{4.80}$$

and

$$V_{i,j+1/2}^{n} = D_{i,j+1/2}^{n} v_{i,j+1/2}^{n} \tag{4.81}$$

Here, $D_{i,j}^{n+1/2}$ denotes intermediate amplification factors or depths. With this method 1., it could be strongly deviating from the old and new depth (and for certain cases even be negative or zero). This feature of this method could possibly spoil some good properties of the underlying one-dimensional advection scheme. Thus an alternative method is suggested here, which we call the "Modified Campin correction", because it is motivated by an idea of Jean-Michel Campin (Massachusetts Institute of Technology).

2.: "Modified Campin correction", a directional split scheme:

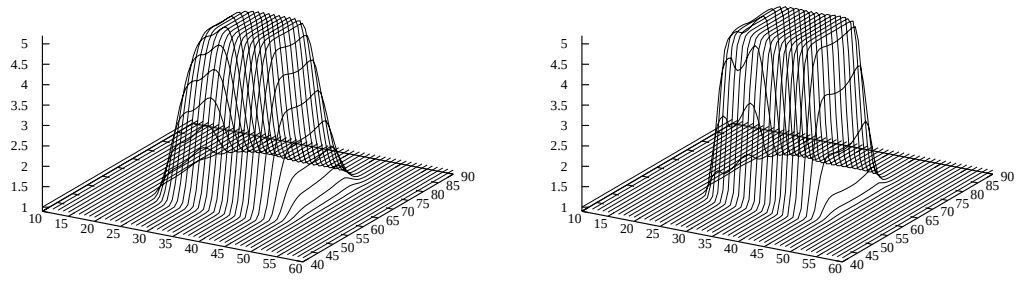

Figure 4.12: Cube resulting after one solid-body rotation with $\Delta x = \Delta y = 1$ m and a Courant number of $c = 0.5$. Left: MUSCL-limiter; right: Superbee limiter.

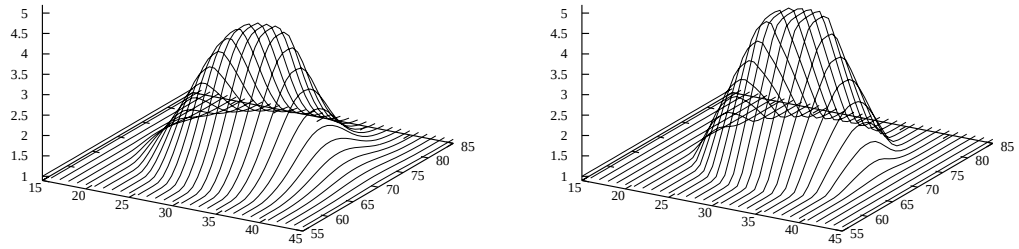

Figure 4.13: Gaussian bell resulting after one solid-body rotation with $\Delta x = \Delta y = 1$ m and a Courant number of $c = 0.5$. Left: MUSCL-limiter; right: Superbee limiter.

$$D_{i,j}^{n+1/2}\Psi_{i,j}^{n+1/2} = D_{i,j}^{n}\Psi_{i,j}^{n} - \frac{\Delta t}{\Delta x}(D_{i+1/2,j}^{n}F_{i+1/2,j}^{n} - D_{i-1/2,j}^{n}F_{i-1/2,j}^{n})$$
$$+\frac{1}{2}\Psi_{i,j}^{n}\left(\frac{\Delta t}{\Delta x}\left(U_{i+1/2,j}^{n} - U_{i-1/2,j}^{n}\right) - \frac{\Delta t}{\Delta y}\left(V_{i,j+1/2}^{n} - V_{i,j-1/2}^{n}\right)\right) \tag{4.82}$$

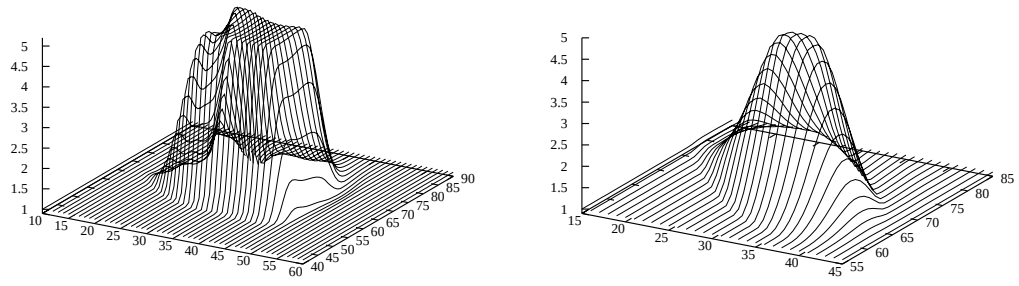

Figure 4.14: Pseudo-two-dimensional P_2-PDM scheme: Cube (left) and Gaussian bell (right) resulting after one solid-body rotation with $\Delta x = \Delta y = 1$ m and a Courant number of $c = 0.5$.

Scheme	N	Min	Max	TV/TV$_0$	TV$_{\max}$/TV$_0$	L_2 error	$\mathcal{O}$
P_2	100	0.395	5.871	1.2771	1.6331	0.240092	–
P_2	200	0.389	5.868	1.2665	1.6785	0.186427	0.365
P_2	400	0.386	5.867	1.2578	1.7074	0.144827	0.364
MUSCL	100	1.000	5.000	1.0315	1.3003	0.246704	–
MUSCL	200	1.000	5.000	1.0251	1.3456	0.190325	0.374
MUSCL	400	1.000	5.000	1.0172	1.3731	0.147447	0.368
Superbee	100	1.000	5.000	1.0538	1.3093	0.182077	–
Superbee	200	1.000	5.000	1.0395	1.3528	0.129787	0.488
Superbee	400	1.000	5.000	1.0276	1.3784	0.093277	0.477
P_2-PDM	100	1.000	5.000	1.0311	1.3117	0.236535	–
P_2-PDM	200	1.000	5.000	1.0224	1.3536	0.182141	0.377
P_2-PDM	400	1.000	5.000	1.0148	1.3783	0.140810	0.371

Table 4.3: Absolute minima (Min) and maxima (Max), total variation of final profile normalised by initial total variation (TV/TV$_0$), L_2 error and empirically estimated order of approximation for the unlimited P_2 scheme, the MUSCL and Superbee schemes and the P_2-PDM scheme for the three-dimensional cube test case.

Scheme	N	Min_{fin}	Max_{fin}	TV/TV_0	$\text{TV}_{\max}/\text{TV}_0$	L_2 error	$\mathcal{O}$
P_2	100	0.9929	4.6206	0.97343	1.00582	0.020165	–
P_2	200	1.0000	4.9370	0.99529	1.00149	0.005408	1.899
P_2	400	1.0000	4.9919	0.99960	1.00037	0.004535	0.254
MUSCL	100	1.0000	4.1797	0.92944	1.00019	0.035405	–
MUSCL	200	1.0000	4.7206	0.98336	1.00005	0.007696	2.202
MUSCL	400	1.0000	4.9074	0.99649	1.00001	0.003808	1.015
Superbee	100	1.0000	4.5053	0.99336	1.00421	0.040727	–
Superbee	200	1.0000	4.8977	1.01584	1.01584	0.017234	1.241
Superbee	400	1.0000	4.9806	1.00984	1.00984	0.007985	1.110
P_2-PDM	100	1.000	4.4755	0.95588	1.00044	0.023478	–
P_2-PDM	200	1.000	4.8759	0.99214	1.00011	0.005782	2.022
P_2-PDM	400	1.000	4.9704	0.99878	1.00011	0.004556	0.344

Table 4.4: Absolute minima (Min) and maxima (Max), total variation of final profile normalised by initial total variation (TV/TV_0), L_2 error and empirically estimated order of approximation for the unlimited P_2 scheme, the MUSCL and Superbee schemes and the P_2-PDM scheme for the three-dimensional Gaussian bell test case.

$$D_{i,j}^{n+1}\Psi_{i,j}^{n+1} = D_{i,j}^{n+1/2}\Psi_{i,j}^{n+1/2} - \frac{\Delta t}{\Delta y}(D_{i,j+1/2}^{n}F_{i,j+1/2}^{n} - D_{i,j-1/2}^{n}F_{i,j-1/2}^{n}) \\ -\frac{1}{2}\Psi_{i,j}^{n}\left(\frac{\Delta t}{\Delta x}\left(U_{i+1/2,j}^{n} - U_{i-1/2,j}^{n}\right) - \frac{\Delta t}{\Delta y}\left(V_{i,j+1/2}^{n} - V_{i,j-1/2}^{n}\right)\right) \tag{4.83}$$

with

$$D_{i,j}^{n+1/2} = \frac{1}{2}\left(D_{i,j}^{n+1} + D_{i,j}^{n}\right) \tag{4.84}$$

Thus the intermediate layer height is the mean of the "old" and the "new" ones. The next scheme is a generalisation of the above mentioned "Campin correction" which has been originally designed for large-scale z-coordinate ocean models at small Courant numbers (pers. comm. Eric Deleersnijder).

3.: "Generalised Campin correction", a directional split scheme:

$$
\begin{aligned}
&D_{i,j}^{n+1/2}\Psi_{i,j}^{n+1/2} - \Psi_{i,j}^{n}(D_{i,j}^{n+1/2} - D_{i,j}^{n}) \\
&\quad = D_{i,j}^{n}\Psi_{i,j}^{n} - \frac{\Delta t}{\Delta x}(D_{i+1/2,j}^{n}F_{i+1/2,j}^{n} - D_{i-1/2,j}^{n}F_{i-1/2,j}^{n}) \\
&\qquad + \Psi_{i,j}^{n}\frac{\Delta t}{\Delta x}\left(U_{i+1/2,j}^{n} - U_{i-1/2,j}^{n}\right)
\end{aligned}
\tag{4.85}
$$

$$
\begin{aligned}
&D_{i,j}^{n+1}\Psi_{i,j}^{n+1} - \Psi_{i,j}^{n}(D_{i,j}^{n+1} - D_{i,j}^{n+1/2}) \\
&\quad = D_{i,j}^{n+1/2}\Psi_{i,j}^{n+1/2} - \frac{\Delta t}{\Delta y}(D_{i,j+1/2}^{n}F_{i,j+1/2}^{n} - D_{i,j-1/2}^{n}F_{i,j-1/2}^{n}) \\
&\qquad + \Psi_{i,j}^{n}\frac{\Delta t}{\Delta y}\left(V_{i,j+1/2}^{n} - V_{i,j-1/2}^{n}\right)
\end{aligned}
\tag{4.86}
$$

Here, $D_{i,j}^{n+1/2}$ is in principle an arbitrary height, but for properly accounting for the case $D_{i,j}^{n+1} = D_{i,j}^{n}$ we choose here again (4.84).
Finally, a fully two-dimensional scheme is used which does not need the computation of intermediate layer thicknesses.

4.: Fully two-dimensional scheme:

$$
\begin{aligned}
&D_{i,j}^{n+1}\Psi_{i,j}^{n+1} = D_{i,j}^{n}\Psi_{i,j}^{n} \\
&\qquad - \frac{\Delta t}{\Delta x}(D_{i+1/2,j}^{n}F_{i+1/2,j}^{n} - D_{i-1/2,j}^{n}F_{i-1/2,j}^{n}) \\
&\qquad - \frac{\Delta t}{\Delta y}(D_{i,j+1/2}^{n}F_{i,j+1/2}^{n} - D_{i,j-1/2}^{n}F_{i,j-1/2}^{n})
\end{aligned}
\tag{4.87}
$$

with the according two-dimensional continuity equation

$$
D_{i,j}^{n+1} = D_{i,j}^{n} - \frac{\Delta t}{\Delta x}(U_{i+1/2,j}^{n} - U_{i-1/2,j}^{n}) - \frac{\Delta t}{\Delta y}(V_{i,j+1/2}^{n} - V_{i,j-1/2}^{n}) \tag{4.88}
$$

For the split schemes 1. - 3., the slope limited P_2 scheme (P_2-PDM) will be used (see *Pietrzak* [1998] and section 4.7.5.1), for the two-dimensional scheme 4., the two-dimensional P_2 scheme (UTOPIA, uniformly third-order polynomial interpolation

algorithm, which has been described and named by *Leonard et al.* [1995]) will be applied together with the flux-correction by *Zalezak* [1979]. This computationally heavy but accurate combination has already been successfully applied by *Burchard and Petersen* [1997] for a two-dimensional xz model.
The test problem investigated here is based on the following velocity field:

$$u = v = \begin{cases} d(1 - a|x - y|) & \text{for } |x - y| < 20 \\ 0 & \text{else.} \end{cases} \tag{4.89}$$

with $a = 0.1$ and $d = 1$ for $t < 12.5$ s and $d = -1$ for $t \geq 12.5$ s. (4.89) can be regarded as a current in a straight channel in a south-west to north-east direction with a linear velocity variation across the channel. In the centre of the channel, the velocity is flowing north-east with a current speed of 1 $\mathrm{m\,s^{-1}}$, and at the banks the currents points south-west-wards with with a current speed of 1 $\mathrm{m\,s^{-1}}$. After 12.5 s, the current is reversing such that after a runtime of 25 s all fluid particles return to their initial position. The width of the channel is $\sqrt{800} \approx 28.28$. It can easily be seen that the velocity field given by (4.89) is divergence-free, but the single one-dimensional contributions are not:

$$\partial_x u = -\partial_y v \neq 0. \tag{4.90}$$

Specifically at the edges of the channel, the flow is strongly divergent in each direction.
In the centre of the channel, a cube with a side length of 20 m is located. The initial condition for Ψ is thus:

$$\Psi = \begin{cases} 5 & \text{for } 40 \leq x, y \leq 60 \\ 1 & \text{else,} \end{cases} \tag{4.91}$$

see figure 4.15.
Numerical experiments are run here for spatial resolutions of $\Delta x = \Delta y = 1$ m and time steps of $\Delta t = 0.1$ s and $\Delta t = 0.8$ s resulting in (one-dimensional) Courant numbers of $c = 0.1$ and $c = 0.8$, respectively.
The distortion of the cube after 12.5 s is shown for the FCT scheme 4 in figure 4.16. Figures 4.17 and 4.18 show the numerical results for all 4 schemes after 25 s for Courant numbers of $c = 0.1$ and $c = 0.8$, respectively. The scheme 3 performs significantly worse than the other schemes. The two other split schemes perform only slightly worse than the FCT scheme 4, which proves for $c = 0.1$ to the be only

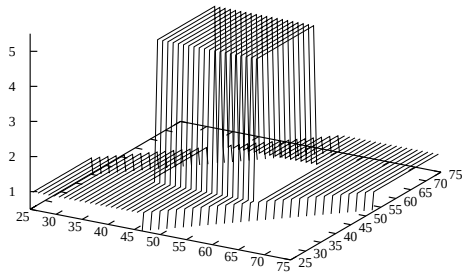

Figure 4.15: Initial condition for the linear distortion test.

Scheme	Courant no.	Min_{fin}	Max_{fin}	TV/TV_0	L_2 error
1	0.1	0.99999	5.00046	1.1069	0.20941
2	0.1	0.99998	5.00046	1.1070	0.20941
3	0.1	0.91385	5.25745	1.2010	0.27860
4	0.1	1.00000	5.00000	1.1039	0.20584
1	0.8	0.98917	5.01530	1.2686	0.29063
2	0.8	0.98226	5.03604	1.2810	0.29097
3	0.8	–	–	–	–
4	0.8	0.86887	5.06703	1.2061	0.25468

Table 4.5: Final minima (Min) and maxima (Max), total variation of final profile normalised by initial total variation (TV/TV_0), and L_2 error for the schemes 1. - 4. for the linear distortion test. Two Courant numbers were used, $c = 0.1$ and $c = 0.8$.

exactly monotone (with machine accuracy) scheme tested here. For $c = 0.8$, the FCT scheme performs worse than the two split schemes 1 and 2, probably due to a more strict stability constraint, although *Leonard et al.* [1995] state that the unlimited UTOPIA scheme should require the same stability constraints that one-dimensional versions.

4.7.5.4 Conclusion for tracer advection schemes

One-dimensional advection schemes applied alternately as directional split methods for multi-dimensional problems seem to be a good compromise between accuracy and computational effort. This has already been stated by several authors, see e.g.

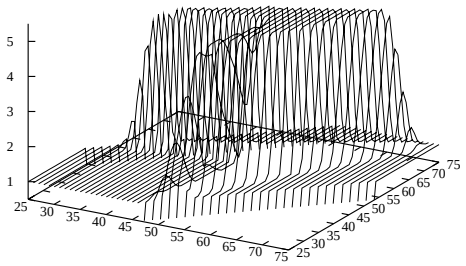

Figure 4.16: Concentrations for the linear distortion test with a Courant number of $c = 0.1$ after half of the runtime (12.5 s) for the fully two-dimensional scheme 4.

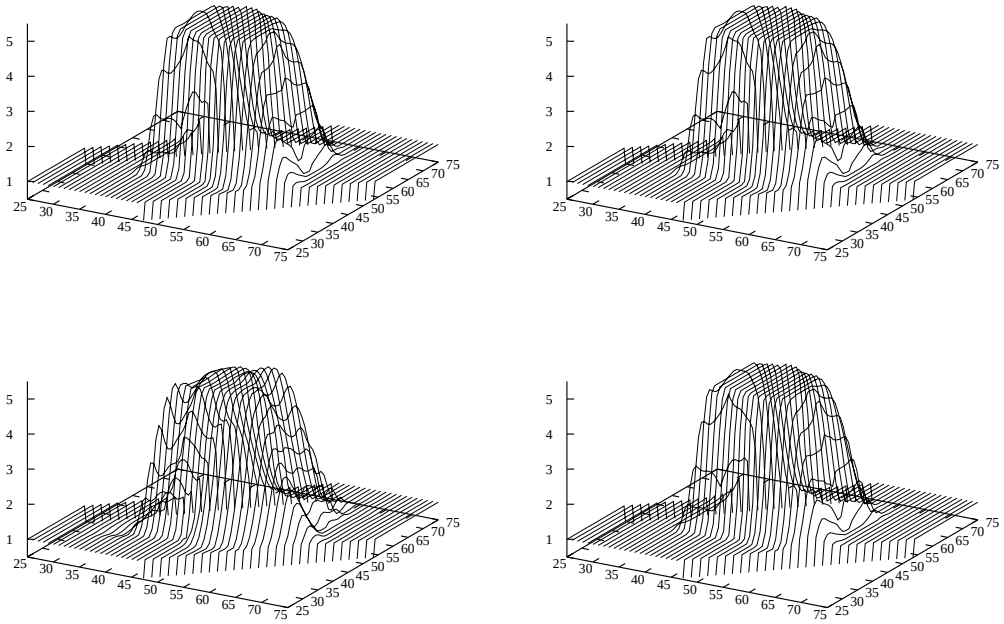

Figure 4.17: Final concentrations for the linear distortion test with a Courant number of $c = 0.1$. Upper left: Scheme 1; upper right: scheme 2; lower left: scheme 3; lower right: scheme 4.

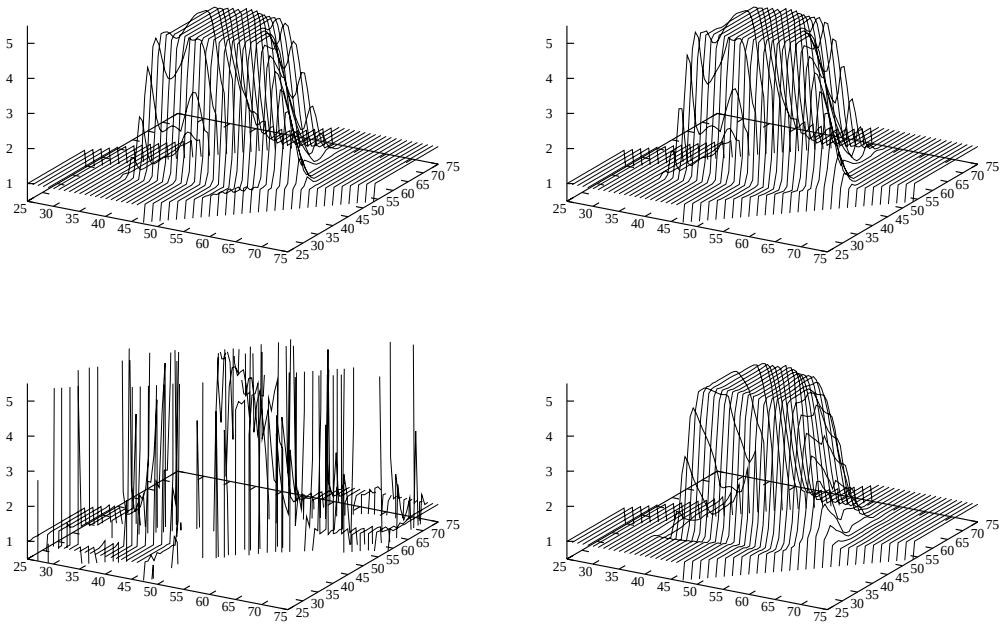

Figure 4.18: Final concentrations for the linear distortion test with a Courant number of $c = 0.8$. Upper left: Scheme 1; upper right: scheme 2; lower left: scheme 3; lower right: scheme 4.

LeVeque [1992] and *Pietrzak* [1998]. They are much easier to implement into three-dimensional ocean models, and they are also faster than multidimensional schemes. The loss of accuracy compared to the computational expensive FCT scheme discussed in section 4.7.5.3 is relatively small. The calculation of intermediate layer thicknesses is essential for the conservation of these split schemes. One potential problem of the conventional split scheme discussed by *Pietrzak* [1998] could be the occurance of zero or negative intermediate layer thicknesses for wadden sea applications. The performance of the split scheme 2 suggested in section 4.7.5.3 which avoids this problem needs to be further assessed in real fluid dynamics applications. It seems that the application of *Strang* [1968] splitting slightly increases the accuracy of the advection schemes in fluid dynamics applications, see the lock exchange test case in section 5.2.

4.8 Internal pressure gradient

The internal part of the pressure gradient is discretised according to *Mellor et al.* [1994]. The crucial part of this term, which is $(\partial_x^* b)_k$ (in the case of the u-equation), is discretised between two vertically adjacent velocity points (i.e. on X-points):

$$\begin{aligned}
&\frac{1}{2}(h_{i,j,k}+h_{i,j,k+1})\,(m\,\partial_{\mathcal{X}}^* b)_{i,j,k}\\
&\approx \frac{1}{2}(h^u_{i,j,k}+h^u_{i,j,k+1})\frac{\frac{1}{2}(b_{i+1,j,k+1}+b_{i+1,j,k})-\frac{1}{2}(b_{i,j,k+1}+b_{i,j,k})}{\Delta x^u_{i,j}}\\
&-(\partial_x z_k)^x_{i,j,k}\left(\frac{1}{2}(b_{i+1,j,k+1}+b_{i,j,k+1})-\frac{1}{2}(b_{i+1,j,k}+b_{i,j,k})\right)
\end{aligned} \tag{4.92}$$

The discretisation (4.92) can be rewritten as:

$$(\partial_x^* b)_k \approx \frac{(\frac{1}{2}-\alpha_b)b_{i+1,j,k+1}+(\frac{1}{2}+\alpha_b)b_{i+1,j,k}-(\frac{1}{2}+\alpha_b)b_{i,j,k+1}-(\frac{1}{2}-\alpha_b)b_{i,j,k}}{\Delta x^u_{i,j}} \tag{4.93}$$

with $\alpha_b = \partial_x z_k \Delta x^u_{i,j}/(h_{i,j,k}+h_{i+1,j,k})$. For $|\alpha| \le \frac{1}{2}$, (4.93) can be interpreted as interpolating vertically between $b_{i+1,j,k+1}$ and $b_{i+1,j,k}$ on one hand and between $b_{i,j,k+1}$ and $b_{i,j,k}$ on the other hand. For $|\alpha_b| > \frac{1}{2}$, extrapolations are made instead. The requirement $|\alpha_b| \le \frac{1}{2}$ is commonly called 'hydrostatic consistency condition' and can be rewritten as:

$$|\partial_x z_k|\frac{\Delta x}{\frac{1}{2}(h_{i,j,k}+h_{i+1,j,k})} \le 1. \tag{4.94}$$

Condition (4.94) is easily violated when the bathymetry is steep and the vertical discretisation fine. The numerical problems arising in σ-coordinate models due to the discretisation of the internal pressure gradient have been discussed by numerous authors, see e.g. *Kliem and Pietrzak* [1999] for an overview. Many numerical schemes have been suggested for circumventing this problem (see e.g. *Stelling and van Kester* [1994] for a non-linear scheme, *McCalpin* [1994] for a fourth-order scheme and *Chu and Fan* [1997] for a sixth-order scheme). Some of these might be integrated into GETM later, in case the second-order scheme fails. It should however be noted that

higher order schemes are not a general remedy for the pressure gradient error, see *Kliem and Pietrzak* [1999].
One alternative, energy-conserving second-order method has been suggested by *Song* [1998]:

$$\begin{aligned}
&\frac{1}{2}(h_{i,j,k}+h_{i,j,k+1})\,(m\,\partial^*_{\mathcal{X}}b)_{i,j,k}\\
&\approx \frac{\frac{1}{4}(b_{i+1,j,k+1}+b_{i+1,j,k})(h^c_{i+1,j,k+1}+h^c_{i+1,j,k})-\frac{1}{4}(b_{i,j,k+1}+b_{i,j,k})(h^c_{i,j,k+1}+h^c_{i,j,k})}{\Delta x^u_{i,j}}\\
&-\left(\frac{1}{2}(b_{i+1,j,k+1}+b_{i,j,k+1})\,(\partial_x z_k)^u_{i,j,k+1}-\frac{1}{2}(b_{i+1,j,k}+b_{i,j,k})\,(\partial_x z_k)^u_{i,j,k+1}\right)
\end{aligned} \tag{4.95}$$

4.9 Coriolis and grid-related rotation

The Coriolis terms in the momentum equations (3.27) and (3.28) are discretised together with the rotational terms due to the curvilinear grid. For doing so, various interpolations of velocities have to be carried out because of the staggering of the Arakawa C-grid. One straight-forward method for the discretisation of these terms is given here.
After multiplication with mn, rotational terms in (3.27) can be discretised as follows:

$$\begin{aligned}
&\left(q_k\left\{f+mn\,v_k\partial_{\mathcal{X}}\left(\frac{1}{n}\right)-mn\,u_k\partial_{\mathcal{Y}}\left(\frac{1}{m}\right)\right\}\right)_{i,j}\approx\\
&q^u_{i,j,k}\left(f^u_{i,j}+v^u_{i,j,k}\frac{\Delta y^c_{i+1,j}-\Delta y^c_{i,j}}{\Delta x^u_{i,j}\Delta y^u_{i,j}}-u_{i,j,k}\frac{\Delta x^+_{i,j}-\Delta x^+_{i,j-1}}{\Delta x^u_{i,j}\Delta y^u_{i,j}}\right)
\end{aligned} \tag{4.96}$$

with $v^u_{i,j,k}=\frac{1}{4}(v_{i,j,k}+v_{i,j-1,k}+v_{i+1,j,k}+v_{i+1,j-1,k})$ and $q^u_{i,j,k}=\frac{1}{4}(q_{i,j,k}+q_{i,j-1,k}+q_{i+1,j,k}+q_{i+1,j-1,k})$.
The same can be done in equation (3.28):

$$\begin{aligned}
&\left(p_k\left\{f+mn\,v_k\partial_{\mathcal{X}}\left(\frac{1}{n}\right)-mn\,u_k\partial_{\mathcal{Y}}\left(\frac{1}{m}\right)\right\}\right)_{i,j}\approx\\
&p^v_{i,j,k}\left(f^v_{i,j}+v^{i,j,k}\frac{\Delta y^+_{i,j}-\Delta y^+_{i-1,j}}{\Delta x^v_{i,j}\Delta y^v_{i,j}}-u^v_{i,j,k}\frac{\Delta x^c_{i,j+1}-\Delta x^c_{i,j}}{\Delta x^v_{i,j}\Delta y^v_{i,j}}\right)
\end{aligned} \tag{4.97}$$

with $u^v_{i,j,k} = \frac{1}{4}(u_{i,j,k} + u_{i,j+1,k} + u_{i-1,j,k} + u_{i-1,j+1,k})$ and $p^v_{i,j,k} = \frac{1}{4}(p_{i,j,k} + p_{i,j+1,k} + p_{i-1,j,k} + p_{i-1,j+1,k})$. Here $f^u_{i,j}$ is the Coriolis frequency at the U-points and $f^v_{i,j}$ the Coriolis frequency at the V-points.
Alternative formulations for spatial averaging have recently been suggested by *Espelid et al.* [2000] for the Coriolis rotation in order to guarantee energy conservation:

$$p^v_{i,j,k} = \frac{\sqrt{h^v_{i,j,k}}}{4}\left(\frac{p_{i,j,k}}{\sqrt{h^u_{i,j,k}}} + \frac{p_{i,j+1,k}}{\sqrt{h^u_{i,j+1,k}}} + \frac{p_{i-1,j,k}}{\sqrt{h^u_{i-1,j,k}}} + \frac{p_{i-1,j+1,k}}{\sqrt{h^u_{i-1,j+1,k}}}\right) \tag{4.98}$$

and

$$q^u_{i,j,k} = \frac{\sqrt{h^u_{i,j,k}}}{4}\left(\frac{q_{i,j,k}}{\sqrt{h^v_{i,j,k}}} + \frac{q_{i,j-1,k}}{\sqrt{h^v_{i,j-1,k}}} + \frac{q_{i+1,j,k}}{\sqrt{h^v_{i+1,j,k}}} + \frac{q_{i+1,j-1,k}}{\sqrt{h^v_{i+1,j-1,k}}}\right) \tag{4.99}$$

The effect of these alternative spatial averaging procedures in combination with curvi-linear coordinates has so far not been investigated.
In order to minimise the violation of kinetic energy conservation due to Coriolis rotation, the horizontal momentum equations are calculated in alternating sequence such as:

$$U \quad V \quad V \quad U \quad U \quad V \quad V \quad U \quad U \quad \ldots$$

(see *Beckers and Deleersnijder* [1993]). In each of these calculations, the most recent result from the preceding equation is used for the evaluation of the Coriolis term. This procedure is used for the vertically integrated mode (2.16) and (2.17) and for the three-dimensional momentum equations (3.15) and (3.16).

4.10 Drying and flooding

The main requirement for drying and flooding is that the vertically integrated fluxes U and V are controlled such that at no point a negative water depth occurs. It is clear that parts of the physics which play an important role in very shallow water of a few centimetres depth like non-hydrostatic effects are not included in the equations. However, the model is designed in a way that the control of U and V in very shallow water is mainly motivated by the physics included in the equations rather than by defining complex drying and flooding algorithms. It is assumed that the major process in this situation is a balance between pressure gradient and bottom friction. Therefore, in the case of very shallow water, all other terms are multiplied with the

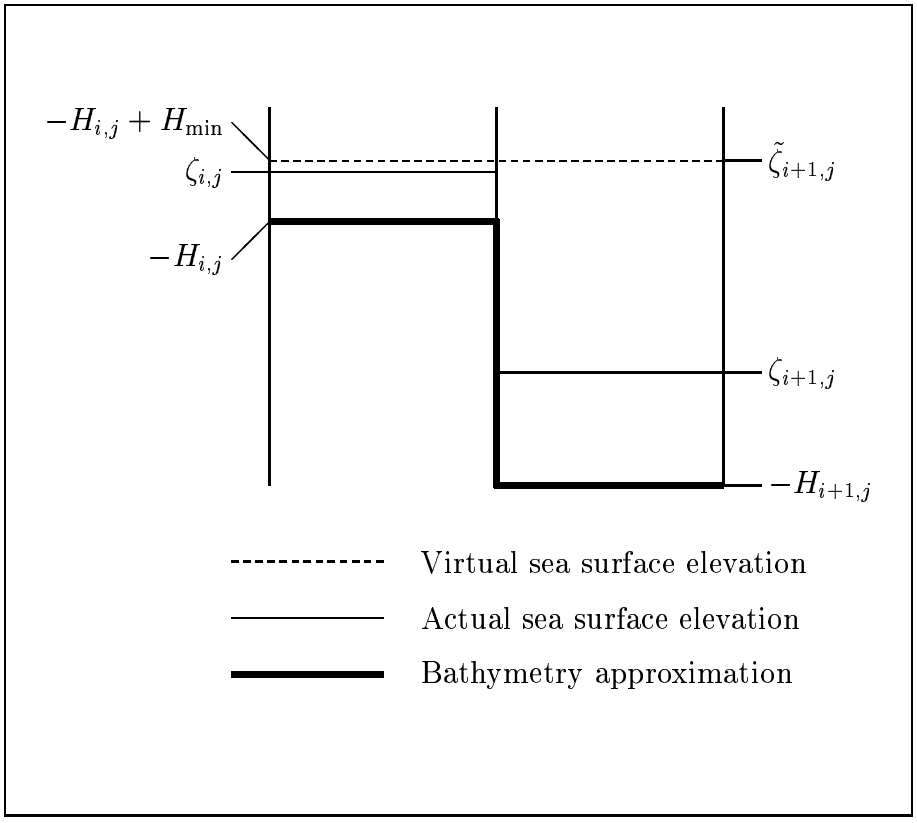

Figure 4.19: Sketch explaining the principle of pressure gradient minimisation during drying and flooding over sloping bathymetry.

non-dimensional factor α which approaches zero when a minimum water depth is reached.
By using formulation (2.26) for calculating the bottom drag coefficient R, it is guaranteed that R is exponentially growing if the water depth approaches very small values. This slows the flow down when the water depth in a velocity point is sinking and also allows for flooding without further manipulation.
In this context, one important question is how to calculated the depth in the velocity points, H^u and H^v, since this determines how shallow the water in the velocity points may become on sloping beaches. In ocean models, usually, the depth in the velocity points is calculated as the mean of depths in adjacent elevation points (T-points):

$$H^u_{i,j} = \frac{1}{2}\left(H_{i,j} + H_{i+1,j}\right), \qquad H^v_{i,j} = \frac{1}{2}\left(H_{i,j} + H_{i,j+1}\right). \tag{4.100}$$

Other models which deal with drying and flooding such as the models of *Duwe* [1988] and *Casulli and Cattani* [1994] use the minimum of the adjacent depths in the T-points:

$$H^u_{i,j} = \min\{H_{i,j}, H_{i+1,j}\}, \qquad H^v_{i,j} = \min\{H_{i,j}, H_{i,j+1}\}. \tag{4.101}$$

This guarantees that all depths in the velocity points around a T-point are not deeper than the depth in the T-point. Thus, when the T-point depth is approaching the minimum depth, then all depths in the velocity points are also small and the friction coefficient correspondingly large.
Each of the methods has however drawbacks: When the mean is taken as in (4.100), the risk of negative water depths is relatively big, and thus higher values of $D_{\min}$ have to be chosen. When the minimum is taken, large mud-flats might need unrealistically long times for drying since all the water volume has to flow through relatively shallow velocity boxes. Also, velocities in these shallow boxes tend to be relatively high in order to provide sufficient transports. This might lead to numerical instabilities.
Therefore, GETM has both options, (4.100) and (4.101) and the addition of various other options such as depth depending weighting of the averaging can easily be added.
If a pressure point is dry (i.e. its bathymetry value is higher than a neighbouring sea surface elevation), the pressure gradient would be unnaturally high with the consequence of unwanted flow acceleration. Therefore this pressure gradient will be manipulated such that (only for the pressure gradient calculation) a virtual sea surface elevation $\tilde{\zeta}$ is assumed (see figure 4.19). In the situation shown in figure 4.19, the left pressure point is dry, and the sea surface elevation there is for numerical reasons even slightly below the critical value $-H_{i,j} + H_{\min}$. In order not to let more water flow out of the left cell, the pressure gradient between the two boxes shown is calculated with a manipulated sea surface elevation on the right, $\tilde{\zeta}_{i+1,j}$.

4.11 Coupling with turbulence model

The turbulence model GOTM (see section 2.3) is located in the T-points. Therefore, the turbulence production terms need to be interpolated to these locations.
For the shear production P from (2.40) the shear squared

$$S^2 = (\partial_z u)^2 + (\partial_z v)^2 \tag{4.102}$$

is calculated in a straight-forward way as follows:

$$(S^2)_{i,j,k} \approx \frac{1}{2}\Bigg(\left(\frac{u_{i,j,k+1} - u_{i,j,k}}{\frac{1}{2}(h^u_{i,j,k+1} + h^u_{i,j,k})} \right)^2 + \left(\frac{u_{i-1,j,k+1} - u_{i-1,j,k}}{\frac{1}{2}(h^u_{i-1,j,k+1} + h^u_{i-1,j,k})} \right)^2 + \left(\frac{v_{i,j,k+1} - v_{i,j,k}}{\frac{1}{2}(h^v_{i,j,k+1} + h^v_{i,j,k})} \right)^2 + \left(\frac{v_{i,j-1,k+1} - v_{i,j-1,k}}{\frac{1}{2}(h^v_{i,j-1,k+1} + h^v_{i,j-1,k})} \right)^2 \Bigg) \tag{4.103}$$

A method which should better conserve energy for strongly varying layer thicknesses (see *Burchard* [2001d]) would be the following:

$$\begin{aligned}(S^2)_{i,j,k} \approx \frac{1}{2}\Bigg(& \frac{\frac{1}{2}(\nu_{i,j,k} + \nu_{i+1,j,k})(u_{i,j,k+1} - u_{i,j,k})^2}{\frac{1}{2}(h^u_{i,j,k+1} + h^u_{i,j,k})} \\ & + \frac{\frac{1}{2}(\nu_{i-1,j,k} + \nu_{i,j,k})(u_{i-1,j,k+1} - u_{i-1,j,k})^2}{\frac{1}{2}(h^u_{i-1,j,k+1} + h^u_{i-1,j,k})} \\ & + \frac{\frac{1}{2}(\nu_{i,j,k} + \nu_{i,j+1,k})(v_{i,j,k+1} - v_{i,j,k})^2}{\frac{1}{2}(h^v_{i,j,k+1} + h^v_{i,j,k})} \\ & + \frac{\frac{1}{2}(\nu_{i,j-1,k} + \nu_{i,j,k})(v_{i,j-1,k+1} - v_{i,j-1,k})^2}{\frac{1}{2}(h^v_{i,j-1,k+1} + h^v_{i,j-1,k})} \Bigg) \\ & \cdot \left(\frac{1}{2}\left(h^c_{i,j,k} + h^c_{i,j,k+1}\right)\nu_{i,j,k} \right)^{-1}\end{aligned} \tag{4.104}$$

The higher numerical stability of (4.104) compared to (4.103) needs to be shown however for some special test scenarios.

For the buoyancy production B from (2.40) the Brunt-Väisälä frequency squared, $N^2 = \partial_z b$ with buoyancy b from (2.4), has to be calculated:

$$(N^2)_{i,j,k} \approx \frac{1}{6}\Bigg(2\frac{b_{i,j,k+1}-b_{i,j,k}}{\frac{1}{2}(h^t_{i,j,k+1}+h^t_{i,j,k})} + \frac{b_{i+1,j,k+1}-b_{i+1,j,k}}{\frac{1}{2}(h^t_{i+1,j,k+1}+h^t_{i+1,j,k})} + \frac{b_{i-1,j,k+1}-b_{i-1,j,k}}{\frac{1}{2}(h^t_{i-1,j,k+1}+h^t_{i-1,j,k})} + \frac{b_{i,j+1,k+1}-b_{i,j+1,k}}{\frac{1}{2}(h^t_{i,j+1,k+1}+h^t_{i,j+1,k})} + \frac{b_{i,j-1,k+1}-b_{i,j-1,k}}{\frac{1}{2}(h^t_{i,j-1,k+1}+h^t_{i,j-1,k})}\Bigg) \tag{4.105}$$

For the case that one or more T-points involved in the calculation of (4.105) are land points, the weighting needs to be corrected in such a way, that the weight of the central T-point (i, j) is twice the weight of each surrounding T-point.
In contrast to the weighted average given by (4.105), the straight-forward discretisation of N^2 is given by

$$(N^2)_{i,j,k} \approx \frac{b_{i,j,k+1}-b_{i,j,k}}{\frac{1}{2}(h^t_{i,j,k+1}+h^t_{i,j,k})}. \tag{4.106}$$

In some cases, this did not produce stable numerical results. The reason for this might be that the velocities involved in the calculation for the shear squared do depend on the buoyancies in the two neighbouring T-points such that the straight-forward method (4.106) leads to an inconsistency. However, other experiments with the energy-conserving discretisation of the shear stress squared, (4.104) and the straight-forward discretisation of N^2, (4.106), produced numerically stable results. Thus, the proper discretisation of the shear and buoyancy production terms surely needs further attention in the future.

Chapter 5

Idealised tests

5.1 Simple channel flow

5.1.1 Grid distortion

In this section a rectangular channel with a constant depth of $H = 2$ m, a length of $L_x = 1500$ m and a width of $L_y = 300$ m is discretised with a distorted grid in order to assess the discretisation error due to the curvilinear coordinates. The two grids with different resolution which are tested here are based on the following functions:

$$y_{i,j} = y^l_j + \frac{2y_c}{L_y^2} y_{i,j}(L_y - y_{i,j}) \exp\left(-b(x_{i,j} - x_0)^2\right),$$

$$x_{i,j} = x^l_i - \frac{2y_c}{L_y^2}\left(\frac{1}{2}L_y y_{i,j}^2 - \frac{1}{3}y_{i,j}^3\right)(-2b(x_{i,j} - x_0)) \exp\left(-b(x_{i,j} - x_0)^2\right), \tag{5.1}$$

with $y_c = 100$ m, $b = 1.6 \cdot 10^{-5}$ m^{-2} and $x_0 = \frac{1}{2}L_x$. For the coarse resolution, $\Delta x^l_i = \Delta y^l_j = 150$ m and for the fine resolution, $\Delta x^l_i = \Delta y^l_j = 50$ m have been used (see figure 5.1). The grid is calculated by prescribing the values of x^l_i and y^l_j and calculating $x_{i,j}$ and $y_{i,j}$ by non-linear iteration over (5.1).
It can easily be seen by converting (5.1) into a continuous function ($x_{i,j} \to x$, $y_{i,j} \to y$) that $\partial_x y = -\partial_y x$, which is equivalent to the orthogonality of the grid.
The vertically integrated flow is forced by an external pressure gradient imposed by an elevation difference at the open boundaries with $\zeta(x = 0) = -0.05$ m and $\zeta(x = L_x) = -0.05$ m. Since no variations in the x-direction are imposed, the resulting flow should be strictly eastwards with the northward velocity component

$v = 0$. This will be checked for the two resolutions along a cross-section at $x = \frac{1}{2}L_x$ where the transformed coordinate is exactly directed along the physical coordinate, such that no re-transformations are needed.
The results are shown in figure 5.2. It can be seen that the velocity varies by about 2 % for both resolutions around a value of $u = 0.62$ m s^{-1}. The northward velocity which should be zero, has a maximum value of $v = 0.008$ m s^{-1} for the fine resolution and the surface elevation deviates by less than 0.001 m from its mean value. These results state that the curvilinear grid as it is used here and discretised in the model leads to a discretisation error which is relatively small for this case. However, this matter should be investigated further with the aim to minimise this grid related error. Probably, the use of higher order advection schemes for momentum will improve the performance of the model for curvilinear coordinates.

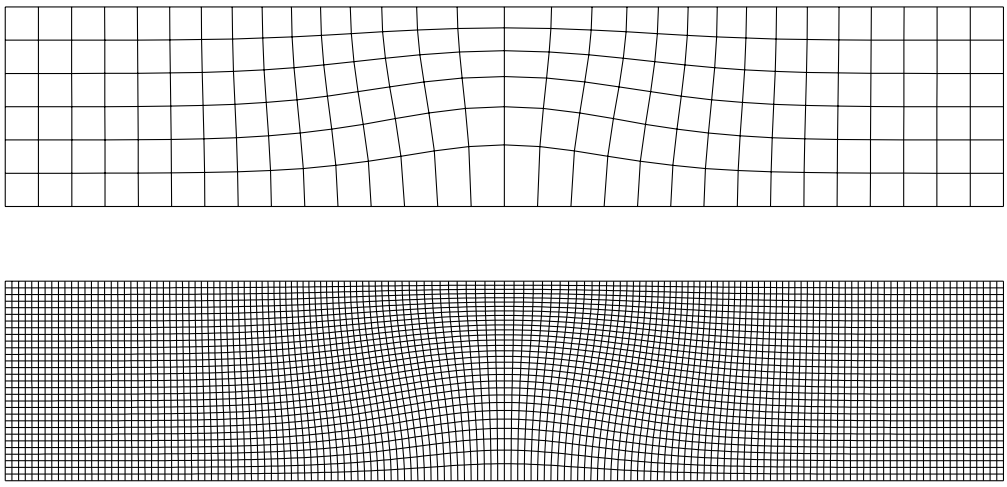

Figure 5.1: Distorted grid test: above: low resolution; below: high resolution.

5.1.2 Bended channel

Here, vertically integrated, steady-state flow in a bended channel is simulated with Cartesian and curvilinear grids. The channel with homogeneous depth ($H = 2$ m) consists of a semi-circle with two straight parts at each end, see figures 5.3 and 5.4. The inner radius of the bended part is 1500 m, the outer radius 2250 m. The uniform width of the channel is 750 m, the lengths of the straight parts at the end is

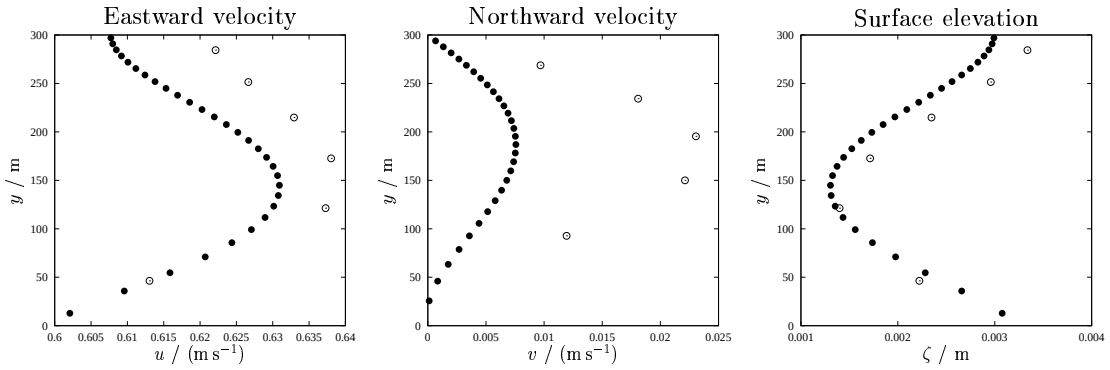

Figure 5.2: Distorted grid test: Northward velocity component (left), eastward velocity component (middle) and surface elevation (right) along a cross-section at $x = \frac{1}{2}L_x$. ○: low resolution solution; ●: high resolution curvilinear.

2250 m each. For the Cartesian grids the resolutions are $\Delta x = \Delta y = 150$ m (coarse) and $\Delta x = \Delta y = 30$ m (fine). The resolutions for the curvilinear grid in the straight parts of the channel are $\Delta x = \Delta y = 150$ m (coarse) and $\Delta x = \Delta y = 50$ m (fine). The flow is forced by an external pressure gradient imposed by different elevations at the open boundaries, which is -0.05 m at the northern open boundary and 0.05 m at the southern open boundary. All test cases have been integrated for 4 hours such that a steady-state given by a balance of advection, bed friction and pressure gradient is approached. The results for v, u and ζ are shown as cross-sections at $y = \frac{1}{2}L_y = 2250$ m, see figure 5.5. Due to the larger along channel pressure gradient, the northward velocity is larger at the inner channel edge than at the outer edge. This is reproduced by all grids. However, the Cartesian grids produce a lateral boundary layer due to numerical friction at the boundaries with zig-zagged boundary approximation. This appears to be a major drawback of Cartesian grids in such flow situations. The high resolution Cartesian grid however approximates the curvilinear solutions well in the centre of the channel, whereas the coarse resolution Cartesian solution significantly underestimates the other results. It should actually be fairly easy to derive an approximate analytical solution for better comparison. For the cross-channel velocity, the curvilinear solutions predict values close to zero, in contrast to the two Cartesian solutions which predict some small cross-flow. It is assumed that this cross-flow component is generated by the lateral boundary layer due to the numerical friction. The predicted surface elevations do all reproduce the effect of flow curvature (centrifugal force) such that the elevations are slightly higher at the outer edge of the channel.

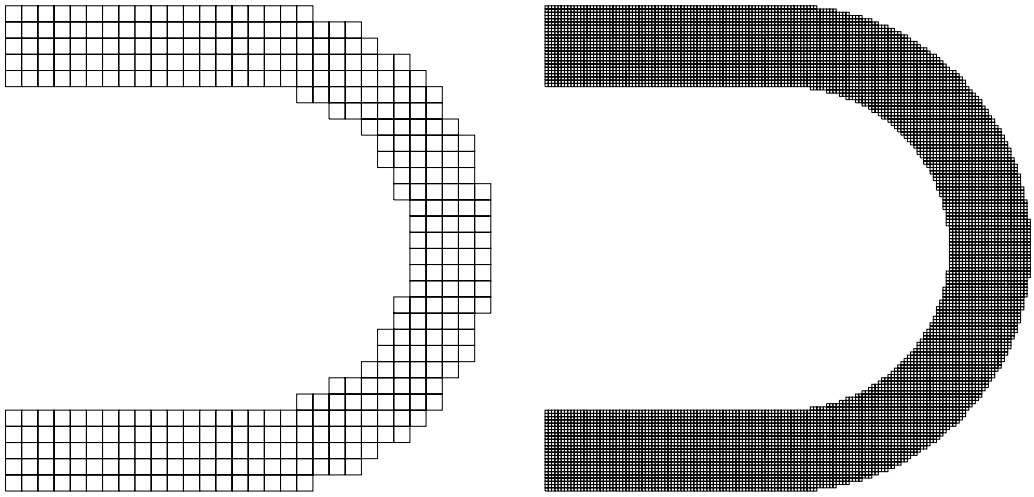

Figure 5.3: Bended channel test: Cartesian coordinate grid; left: low resolution; right: high resolution.

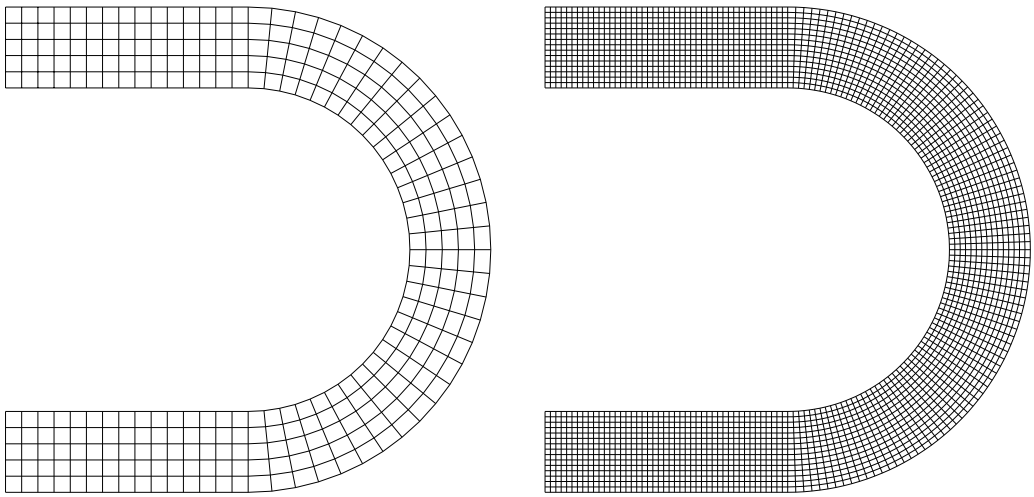

Figure 5.4: Bended channel test: Curvilinear coordinate grid; left: low resolution; right: high resolution.

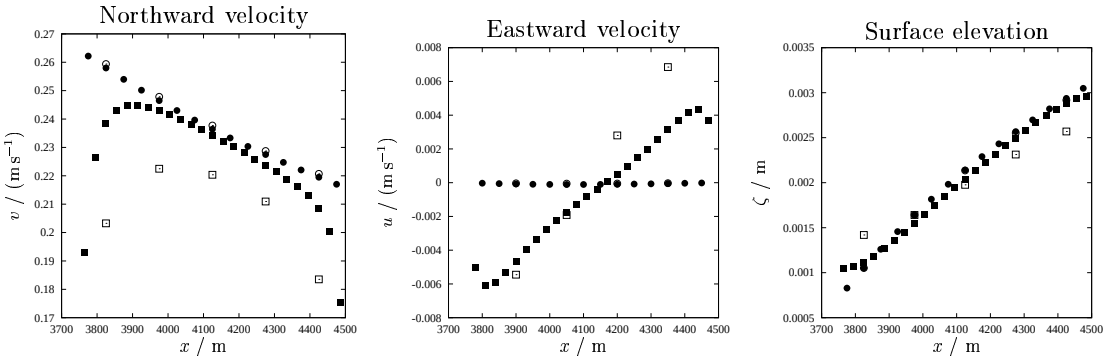

Figure 5.5: Bended channel test: Northward velocity component (left), eastward velocity component (middle) and surface elevation (right) along a longitudinal cross-section at $y = \frac{1}{2}L_y$. ○: low resolution curvilinear solution; ●: high resolution curvilinear solution; □: low resolution Cartesian solution; ■: high resolution Cartesian solution.

5.1.3 Constricted channel

A further test case is a constricted channel with a length of $L_x = 1500$ m, a maximum width of $L_y = 300$ m at both end and a minimum width of 100 m in the middle. Three Cartesian grids with $\Delta x = \Delta y = 50$ m (coarse), $\Delta x = \Delta y = 10$ m (fine) and $\Delta x = \Delta y = 2.5$ m (very fine) and two curvilinear grids with a grid-spacing equivalent to the coarse and fine Cartesian grids will be tested (see figures 5.6 and 5.7). Similarly to section 5.1.1, the curvilinear grids are given by an analytical expression as well:

$$
\begin{aligned}
y_{i,j} &= y^l_j + \frac{y_c}{y_0}(y_0 - y_{i,j})D_{i,j} \\
x_{i,j} &= x^l_i - \frac{y_c}{y_0}y_{i,j}\left(y_0 - \frac{\frac{1}{2}y^2_{i,j} - y_c D_{i,j}}{1 - \frac{y_c}{y_0}D_{i,j}}\right)(-2b(x_{i,j} - x_0))D_{i,j} \\
&\qquad + y_c\left(y_0 - \frac{\frac{1}{2}y^2_0 - y_c D_{i,j}}{1 - \frac{y_c}{y_0}D_{i,j}}\right)(-2b(x_{i,j} - x_0))D_{i,j}, \\
D_{i,j} &= \exp\left(-b(x_{i,j} - x_0)^2\right),
\end{aligned}
\tag{5.2}
$$

such that $x_{i,j} = x^l_i$ for $y_{i,j} = y_0$. Also here, the orthogonality can easily be proven.

In (5.2), the following parameters have been used: $y_c = 100$ m, $x_0 = \frac{1}{2}L_x$, $y_0 = \frac{1}{2}L_y$, $b = 1.6 \cdot 10^{-5}$ m^{-2}.

The uniform depth of the channel is $H = 2$ m. The forcing will be again imposed by a prescribed elevation difference ($\zeta(x = 0) = -0.05$ m and $\zeta(x = L_x) = -0.05$ m). The results for all five grids are shown in figures 5.8 and 5.9. Figure 5.8 shows u, v and ζ along a cross-section at $x = \frac{1}{2}L_x$. The curvilinear grids predict flow maxima at the edges of the flow whereas the Cartesian solutions show the typical lateral boundary layer due to numerical friction. Only the very fine Cartesian solution predicts a local velocity minimum in the centre of the channel. The flow velocity for the fine resolution curvilinear solution is significantly higher than the corresponding low resolution solution. This is due to the fact, that the cross-section for the low resolution curvilinear grid is slightly wider than the high-resolution grid, because the values of $\Delta y^u_{i,j}$ have been interpolated from the $\Delta y^c_{i,j}$ values. All grids predict some non-zero northward flow velocity. The curvilinear grids show a southward component in the northern part and vice versa. The very high resolution Cartesian grid partially confirms this, although the numerical boundary layer effect is clearly visible. The surface elevation has a maximum in the centre of the flow for all grids except the coarse resolution Cartesian grids (which has only two grid points across the channel). The fine curvilinear grid predicts however a significantly lower surface elevation than all other grids, probably due to the higher flow velocity.

Figure 5.9 shows along channel velocity and surface elevation for all five grids. Also here, the effect of numerical friction is visible: the total flux through the channel is significantly lower for the Cartesian grids. Also, the hydraulic jump at about $x = \frac{1}{2}L_x$ is more pronounced for the high-resolution Cartesian grid than for the other grids due to the higher flow velocities in this test case.

The constricted channel in curvilinear coordinates has also been used for generating the GETM logo shown on the front page of this report. The logo **GETM** has been discretised by hand with 30 increments in the vertical and then been used as initial condition for tracer concentration with $c = 20$ being the concentration for the acronym and $c = 10$ being the background concentration. In order to fit this initial condition to the left side of the constricted channel, it was extended such that the length was now $L_x = 4100$ m. The sea surface elevation difference at the open boundaries was again 0.1 m. After the flow was in steady-state, the tracer concentration was reinitialised and thus transported through the constriction. For this, the curvilinear grid with fine resolution with 30 increments in south-north direction was used. The result is shown in figure 5.10 in such a way that all grid boxes with $c > 13$ are drawn. As advection scheme, the Superbee limiter has been used in order to retain steep gradients as much as possible. At some places, concentrations dropped from $c = 20$ to below $c = 13$, since some parts of the acronym

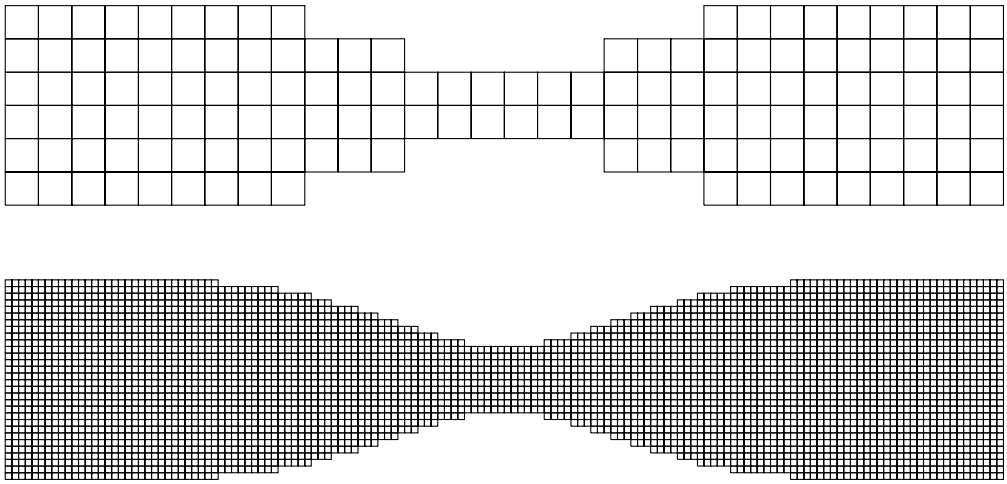

Figure 5.6: Constricted channel test: Cartesian coordinate grid; above: low resolution; below: high resolution.

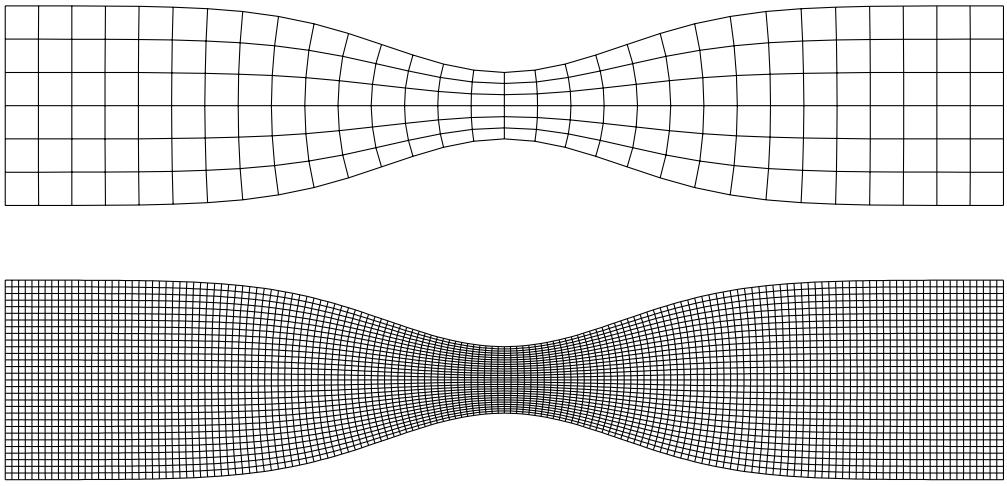

Figure 5.7: Constricted channel test: Curvilinear coordinate grid; above: low resolution; below: high resolution.

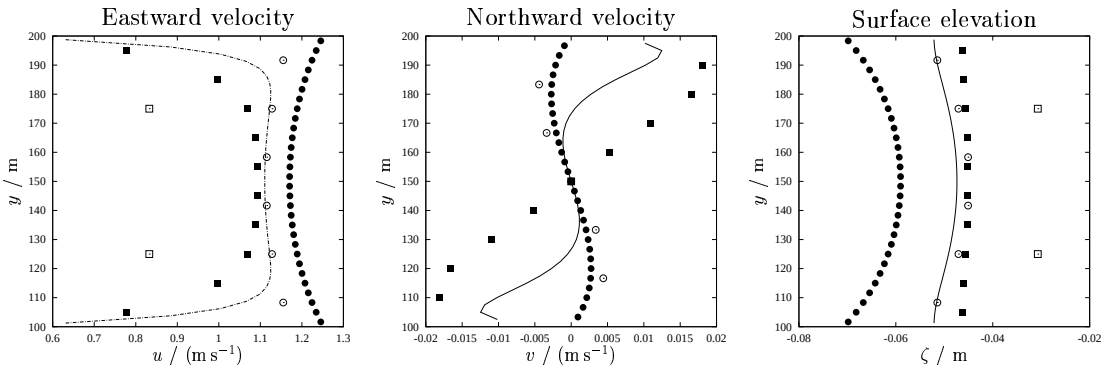

Figure 5.8: Constricted channel test: Northward velocity component (left), eastward velocity component (middle) and surface elevation (right) along a cross-section at $x = \frac{1}{2}L_x$. O: low resolution curvilinear solution; ●: high resolution curvilinear solution; □: low resolution Cartesian solution; ■: high resolution Cartesian solution; ———: very high resolution Cartesian solution.

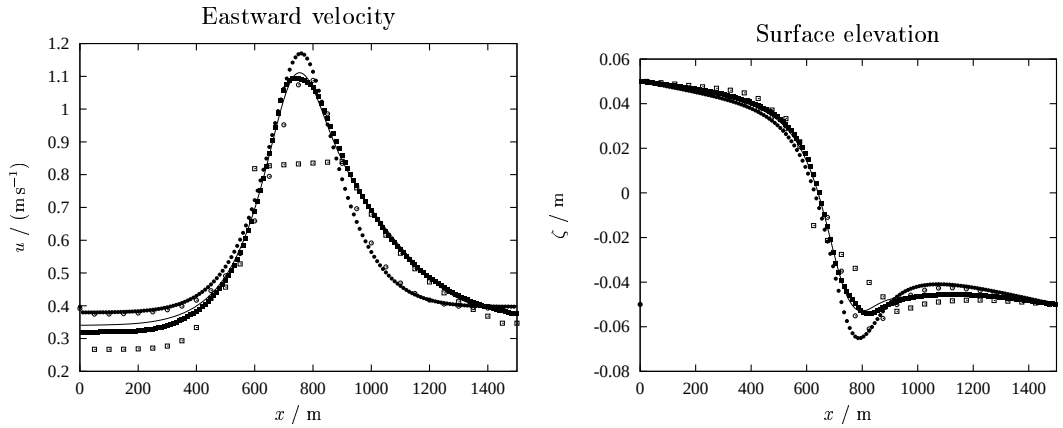

Figure 5.9: Constricted channel test: Eastward velocity component (left) and surface elevation (right) along a longitudinal section at $y = \frac{1}{2}L_y$. O: low resolution curvilinear solution; ●: high resolution curvilinear solution; □: low resolution Cartesian solution; ■: high resolution Cartesian solution; ———: very high resolution Cartesian solution.

were only 2 increments wide in along-flow direction. In addition to the numerical diffusion of the acronym, also some spatial distortion is visible, especially inside the constriction. It should be noted that this TVD-based scheme was minimum and maximum conserving and monotone, as discussed in section 4.7.5.2.
The logo of the 11th Biennial Conference on Physics in Estuaries and Coastal Sea (September 17-20 in Hamburg, Germany, see `http://www.pecs-conference.org`) has been generated with the same method as discussed above, see figure 5.11.

5.2 Lock exchange test

Here, a more realistic fluid mechanical test case with non-constant and non-divergent flow is investigated. In this so-called lock exchange test, a 64 km long and 20 m deep closed rectangular basin with vertical walls two water masses with a density difference of 5 $\mathrm{kg\,m^{-3}}$ are initially separated by an interface which is removed at $t = 0$ (see *Haidvogel and Beckmann* [1999]). Friction and rotation are set to zero. Due to the internal pressure gradient, a circulation is set on with the heavier water layering under the lighter water. Due to the sharp density difference and flow divergence at the moving fronts near the surface and near the bed, this is a good test cases for advection schemes. Nine directional split schemes are tested here, the first-order upstream scheme, the Superbee scheme, the MUSCL scheme, the unlimited P_2 scheme and the limited P_2 scheme. For the latter four, the three directional splits are either performed alternately in the sequence x, y and z or using the symmetric in time *Strang* [1968] splitting with two half steps in x- and in y-direction, a full step in z-direction, followed by two half steps in y- and in x-direction. By doing so, the temporal accuracy can be increased to second order. The numerical results for the nine schemes are shown in figures 5.12, 5.13, 5.14, 5.15 and 5.16. It can be seen that the first-order upstream scheme produces considerable numerical diffusion, and the two unlimited P_2 schemes produce strong numerical dispersion leading to overshoots and undershoots at the fronts. The limited schemes do basically not suffer from these drawbacks. The Superbee scheme performs as expected best for this test case without mixing. The MUSCL and the P_2-PDM scheme give similar results. The differences between the cases with and without *Strang* [1968] splitting are small. The numerical result without *Strang* [1968] splitting shows however small under- and overshoots for the limited P_2-PDM of the order of 10^{-6} $\mathrm{kg\,m^{-3}}$, whereas the *Strang* [1968] splitting scheme is monotone up to machine accuracy.

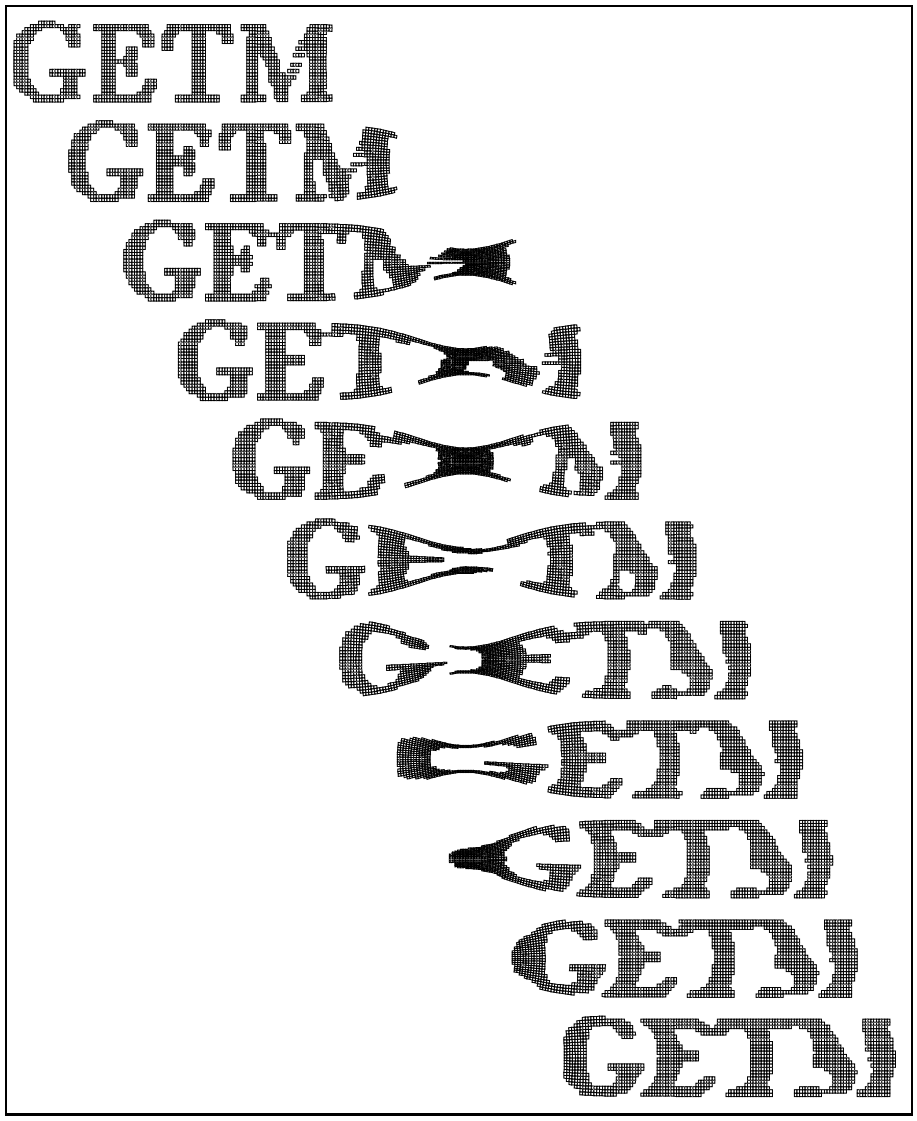

Figure 5.10: Advection of the acronym **GETM** in steady-state flow through the extended constricted channel with curvilinear coordinates in fine resolution. Shown are all grid boxes with $c > 13$, with $c = 20$ being the initial concentration for the acronym and $c = 10$ being the background concentration.

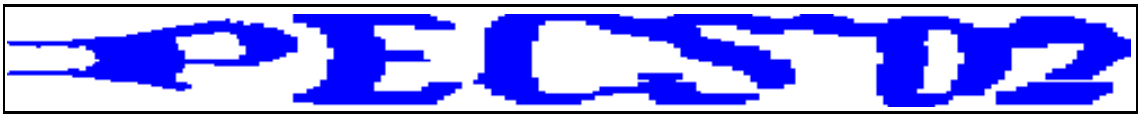

Figure 5.11: Generation of the **PECS**-Logo (Conference on Physics of Estuaries and Coastal Seas) with the same method as shown in figure 5.10.

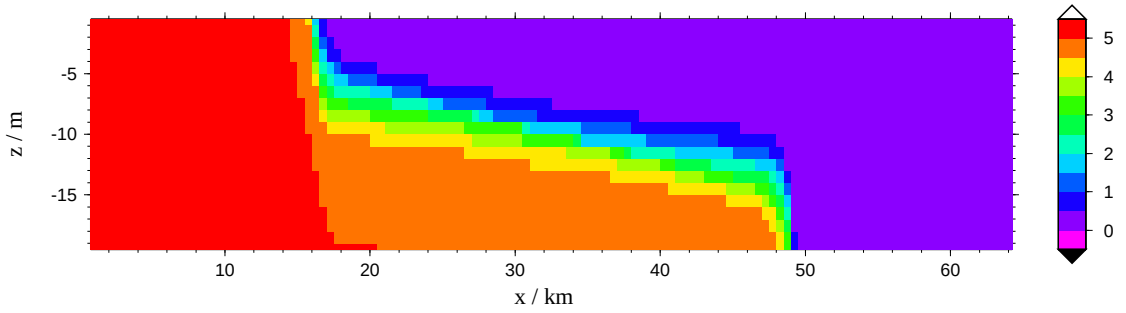

Figure 5.12: Lock exchange experiment: Density distribution for the upstream scheme at the end of the experiment.

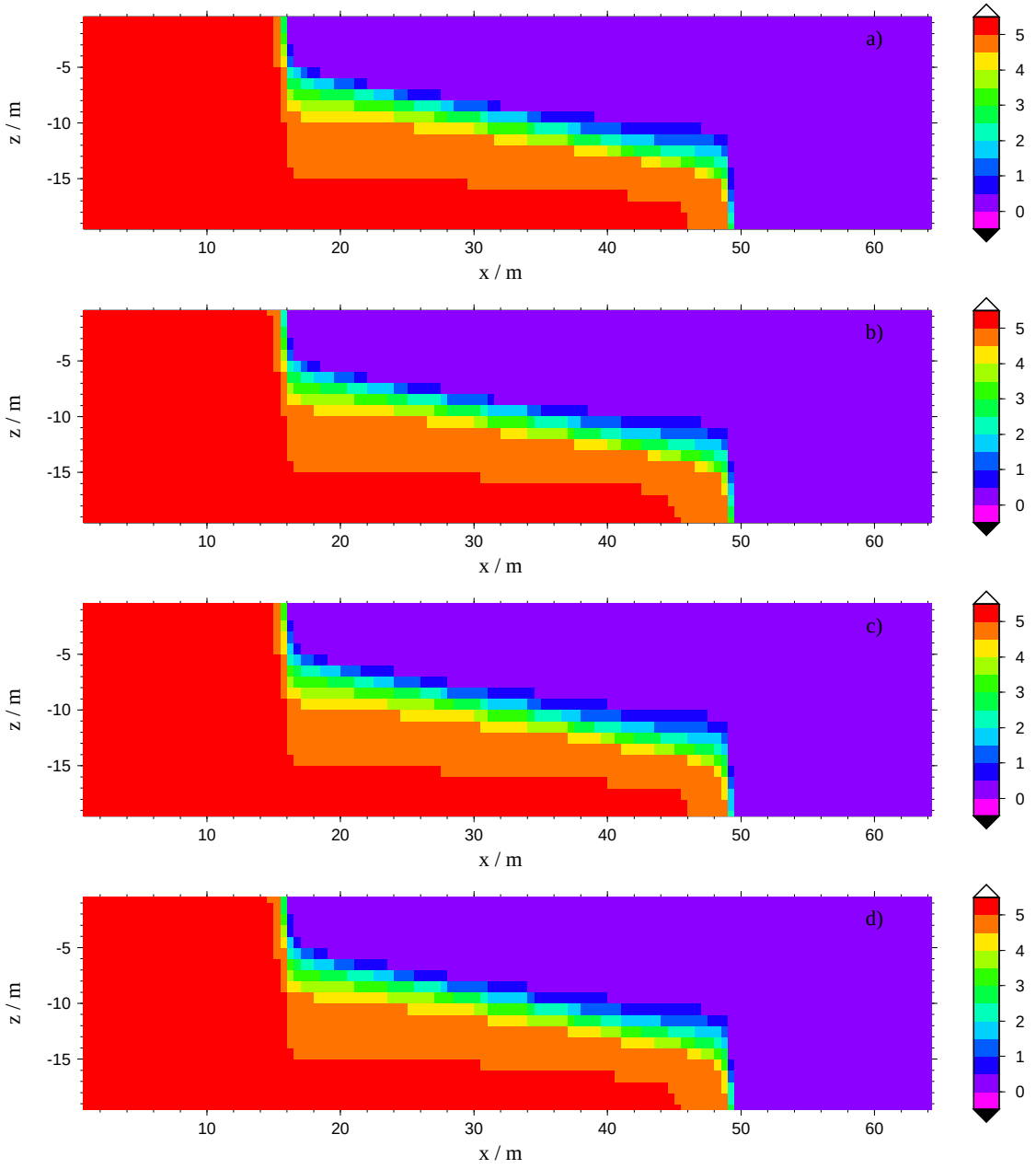

Figure 5.13: Lock exchange experiment: Density distribution for four different numerical schemes at the end of the experiment. a) Superbee scheme without *Strang* [1968] splitting; b) Superbee scheme with *Strang* [1968] splitting; c) MUSCL scheme without *Strang* [1968] splitting; d) MUSCL scheme with *Strang* [1968] splitting.

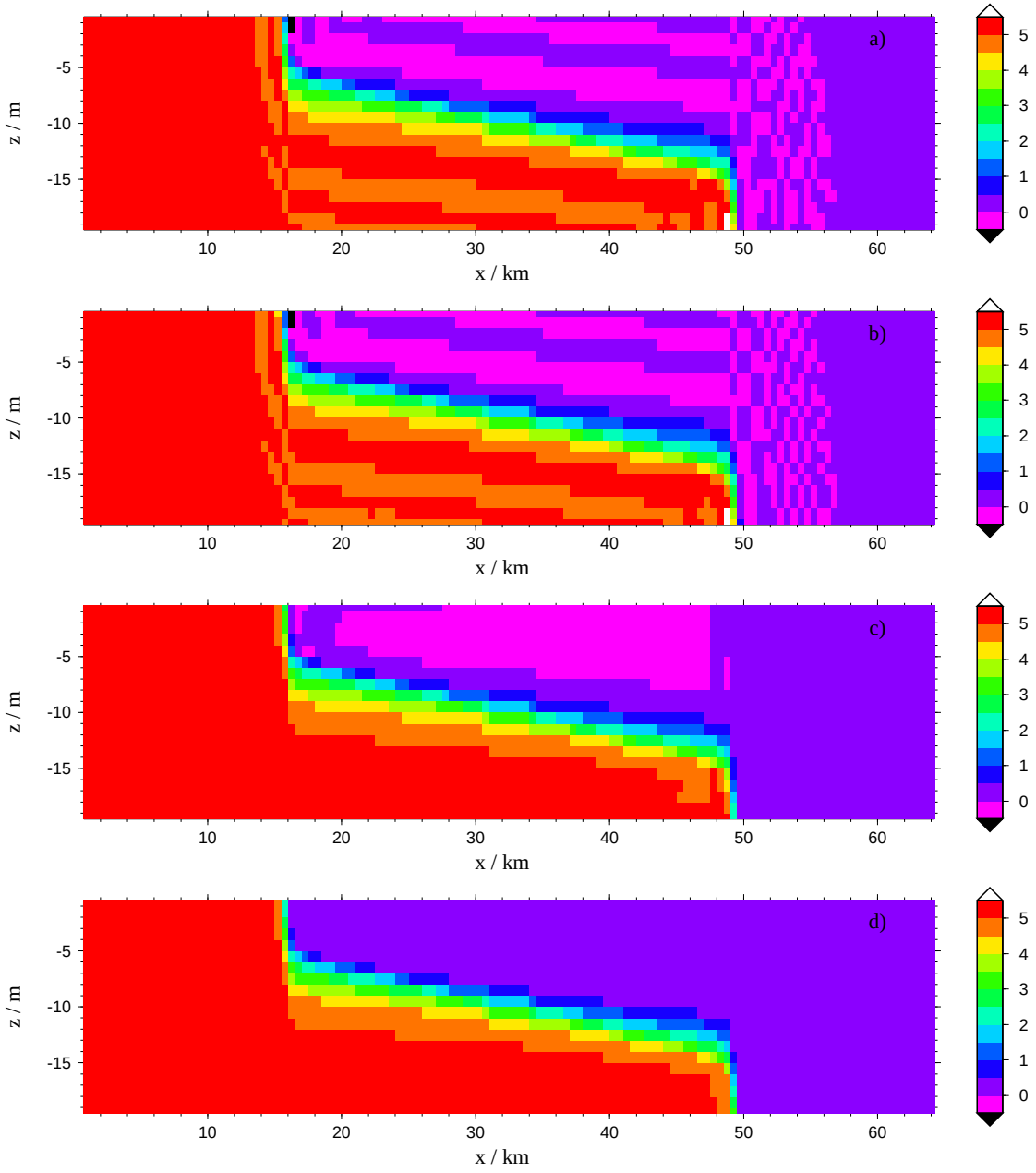

Figure 5.14: Lock exchange experiment: Density distribution for four different numerical schemes at the end of the experiment. a) P_2 scheme without *Strang* [1968] splitting; b) P_2 scheme with *Strang* [1968] splitting; c) limited P_2 scheme without *Strang* [1968] splitting; d) limited P_2 scheme with *Strang* [1968] splitting.

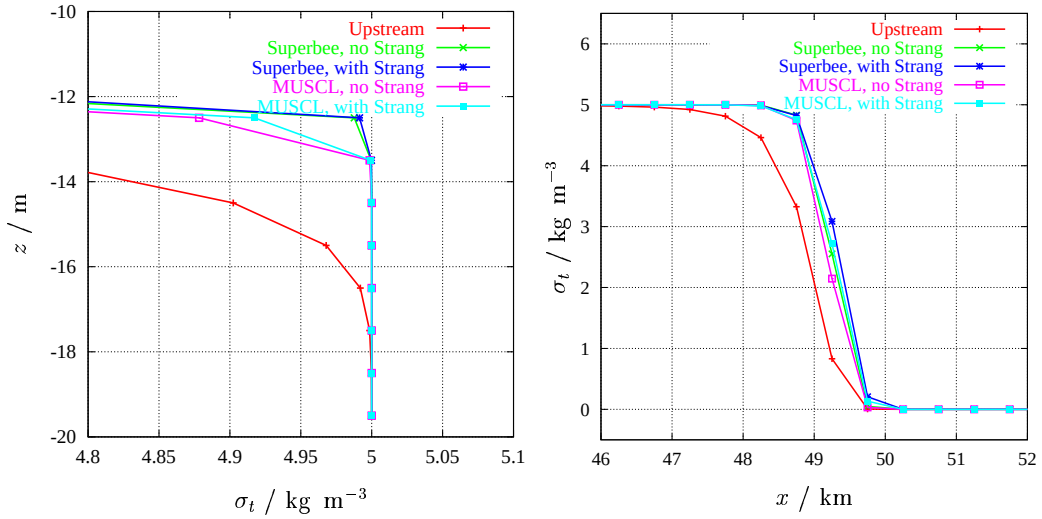

Figure 5.15: Lock-exchange experiment: vertical density profiles (left) and near-bed density distribution of density (right) for five different numerical schemes (Upstream, Superbee, MUSCL) at $x = 32$ km at the end of the experiment.

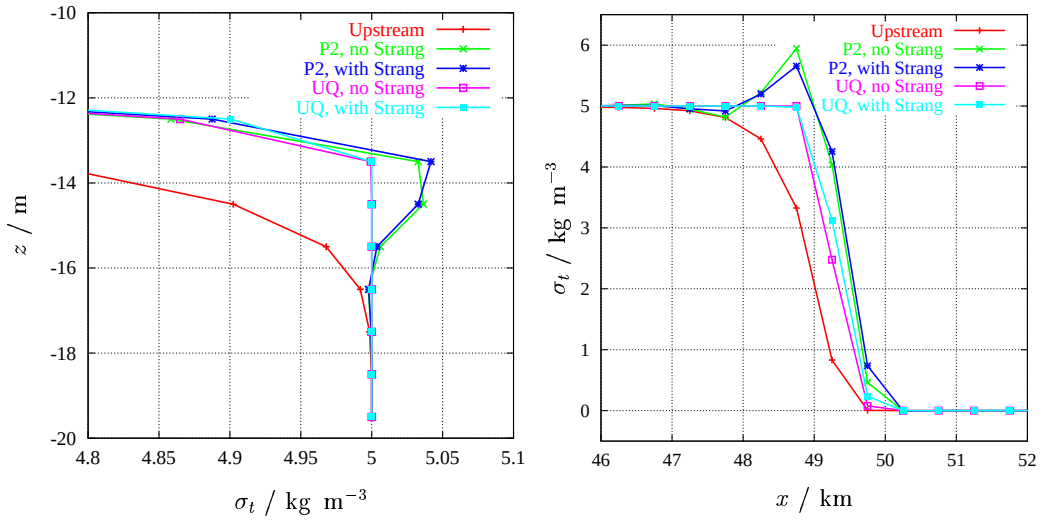

Figure 5.16: Lock-exchange experiment: vertical density profiles (left) and near-bed density distribution of density (right) for five different numerical schemes (Upstream, P_2, P_2-PDM) at $x = 32$ km at the end of the experiment.

5.3 Estuarine turbidity maximum

This section 5.3 has been written and kindly provided to us by Dr. Manuel Ruiz Villarreal, Institute for Oceanography, University of Hamburg, Germany. The presented study is part of a project on the modelling of estuarine turbidity maxima in the Elbe estuary funded by the Marie Curie Program of the European Commission. The present version of GETM (extended by a routine for SPM dynamics) has been used for this numerical study.

In this section, an idealised set-up for studying the mechanisms that induce the appearance of an Estuarine Turbidity Maximum is described. Estuarine Turbidity Maxima (ETMs) are characterised by high concentrations of suspended sediment matter in a region of an estuary, usually near the tip of the salt wedge. ETMs are associated to accumulation of organic material, and therefore are of great ecological interest. They usually appear under the combined effect of tides and density gradients between river and coastal waters. The model set-up designed for studying ETMs is based on the study by *Burchard and Baumert* [1998], who applied a 2D model in a similar set-up to study the physical mechanisms that influence the appearance of an ETM. The dimensions of the domain and other relevant parameters (river run-off, sediment features...) are set to those characteristic of the Elbe estuary. A 2D channel of length L_x=100 km and constant depth of 15 m is closed at the left boundary where a weir in the real Elbe estuary exists. Tidal forcing at the open boundary is a M_2 tide of amplitude 1.3 m and at the river boundary, a river run-off of 700 m^3s^{-1}, the most frequent value for the Elbe river, is imposed. To represent the open sea influence at the right open boundary, salinity is relaxed towards a value of 30 psu during the first 20 km, with a relaxation factor linearly increasing towards the open sea, where the salinity $S = 30$ psu is prescribed. Temperature is neglected. The horizontal spatial steps are set to $\Delta x = \Delta y = 200$ m, and $N = 30$ equidistant σ-layers in the vertical are considered, which results in a vertical step of Δz=0.5 m. The micro time step is $\Delta t_m = 10$ s and with $M = 5$, the macro time step is Δt= 50 s. The k-ε model with stability functions by *Canuto et al.* [2001] is used as turbulence model. Neumann flux boundary conditions for k and ε are chosen (see *Burchard and Petersen* [1999]). The value of the empirical constant $c_{3\varepsilon}$, that determines the dampening effect of stratification on turbulence is set to the value recommended by *Burchard and Bolding* [2001] for this set of stability functions.

A simple model for Suspended Particulate Matter (SPM) with a single class of non-cohesive SPM particles that do not interact with the mean flow (no density effect of SPM) is considered. The concentration C of SPM is modelled with the tracer

equation:

$$\partial_t C + \partial_x(uC) + \partial_y(vC) + \partial_z\left((w - w_s)C\right) - \partial_z\left(\nu_t'\partial_z C\right) \\ -\partial_x\left(A_h^T\partial_x C\right) - \partial_y\left(A_h^T\partial_y C\right) = 0 \tag{5.3}$$

where w_s is the sinking velocity of SPM, that will be set to a constant value (0.001 $\mathrm{m\,s^{-1}}$) characteristic of the Elbe estuary. At the open boundary, no-flux conditions are imposed:

$$\partial_x C = 0 \tag{5.4}$$

Also, no flux through the surface is assumed:

$$w_s C + \nu_t'\partial_z C = 0 \tag{5.5}$$

At the bottom, SPM flux is the result of erosion minus sedimentation:

$$-w_s C - \nu_t'\partial_z C = F_e - F_s \tag{5.6}$$

where erosion and sedimentation fluxes are modelled following *Krone* [1962] as functions of the bottom shear stress τ_b. This parameterisation has been widely applied because its simplicity and because it requires only few empirical parameters. The erosion flux is only not zero when the bottom shear stress exceeds a critical shear stress τ_{ce}

$$F_e = \tfrac{c_e}{\rho_0}(|\tau_b| - \tau_{ce})^+, \tag{5.7}$$

with c_e, a proportionality constant set to 0.5 $\mathrm{kg\,s\,m^{-4}}$. The sedimentation flux is only not zero for bottom shear stresses smaller than a critical shear stress τ_{cs}. This flux is limited by the near bottom concentration C_b.

$$F_s = \tfrac{w_s C_b}{\tau_{cs}}(|\tau_b| - \tau_{cs})^+ \tag{5.8}$$

The selected values of critical shear stresses are based in empirical estimations in the Elbe estuary. The critical shear stress for erosion is set to 0.13 $\mathrm{N\,m^{-2}}$, and for sedimentation to a slightly lower value of 0.1 $\mathrm{N\ m^{-2}}$. A pool B of non-dynamic particulate matter is assumed to take into account the effects of depletion of erodible material at the bottom. A constant value of this pool $\mathrm{B_0}$ is 0.3 $\mathrm{kg\,m^{-2}}$ is initially assumed in all points of the domain. Sedimentation and erosion fill and empty this pool, respectively:

$$\partial_t(B) = F_s - F_e \tag{5.9}$$

and the erosion flux is constricted by the availability of SPM from the pool, i.e. erosion flux only exists when the pool is not depleted and the value of the flux is limited by the quantity of sediment still in the pool.

The model has been run without computing SPM for 20 tidal cycles, when a periodically steady state is reached. Afterwards, the whole model with SPM dynamics is run until a periodically steady state in SPM concentration is found. In figure 5.17, four different tidal instants for this steady state are shown. Bottom shear stresses exhibit a maximum at full tides, which we define as the instant of maximum velocities, and have a minimum at slack tides, when elevation reaches maxima or minima. A clear saltwedge with a tip around 40 km from the open boundary is evident. During flood, denser salty water enters the estuary, and is transported above fresher water near the bottom due to near-bed shear. Because of this unstable stratification, the bottom part of the water column tends to be well mixed. This process is opposite during ebb, when fresh water encounters the salty water and propagates faster at surface layers.

During flood, the increase of bottom shear stress until full flood resuspends material that is advected with the ingoing current causing the strong maximum of SPM concentration near the tip of the salt wedge. Inhibition of mixing in the halocline confines SPM to the lower part of the water column. In the freshwater part of the estuary, near the saltwedge tip, no halocline exists and resuspended SPM can reach surface layers as seen in figure 5.17a. After full flood, tidal velocities reduce and also bottom shear stresses, and reach a minimum at high water. The lower shear stresses decrease the erosion rate and at the end of the flood, also deposition takes place. This reduces SPM concentration at the ETM (figure 5.17b). During ebb, the current reverses and bottom shear stresses start to increase again, so erosion starts again and a peak in SPM concentration appears. It is interesting to note that two different peaks appear during early ebb (see figure 5.17c.), one in the stratified region and the other in the non-stratified region. The increase of erosion rate and the density distribution clearly can explain these ebb peaks. The reduction of velocities decreases erosion from full ebb on and sedimentation refills the bottom pool. The ETM is still present at low water (figure 5.17d), partly because of the small sinking velocities considered.

This combination of tidal motion in a stratified environment induces the setting up of an ETM, that we have been able to reproduce with the numerical model. Although we have only described the model results in general terms, the results show the models ability in describing the kind of effects that dominate circulation and transport of sediments in partially mixed and strongly mixed estuaries. Further experiments with this setup can help in increasing our knowledge on the physics of ETMs and also in assessing the effect of different model assumptions (vertical

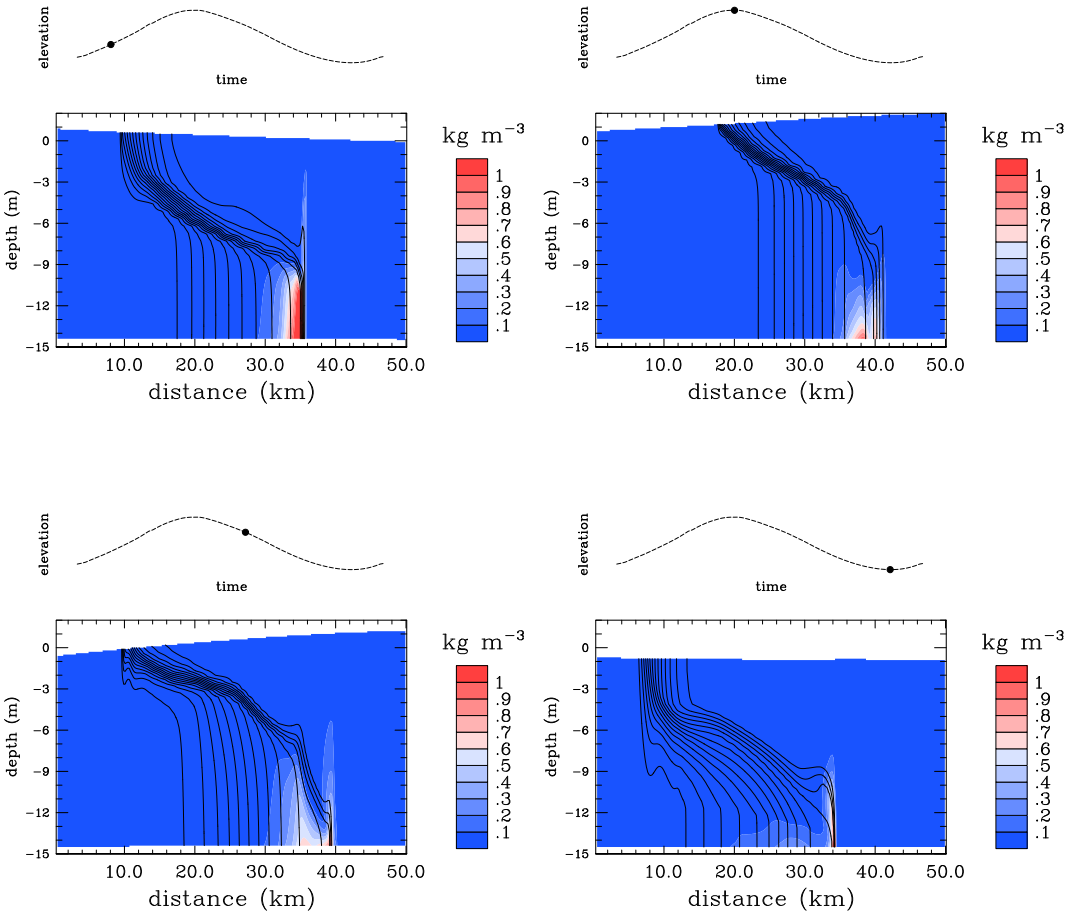

Figure 5.17: Salinity (contours) and SPM concentration (shaded) on the first 50 km of the domain for four tidal instants: a) full flood, b) high water, c) full ebb and d) low water. Salinity is plotted in contours with minimum contour (to the right) 2 PSU and maximum (to the left) 30 PSU. Instantaneous tidal elevation at 40 km is marked with a point in the elevation plot on top of every figure.

coordinates, advection schemes, turbulence parameterisations...) in the simulation of ETMs in tidal estuaries. This will allow us to decide on the best assumptions for realistic 3D simulations of SPM transport in the Elbe estuary, for which the GETM model seems to be fully appropriate.

5.4 Freshwater eddy

Here, a lens of relative low salinity is placed on top of denser ambient water initially at rest. This test case has been suggested by *Tartinville et al.* [1998] for the NOMADS concerted action within the MAST-III programme of the European Communities. In this project various numerical shelf sea models for the North Sea have been compared. The experiment is set up such, that a mode two instability should arise after geostrophical adjustment due to baroclinic instability. This has been proven by rotating tank experiments by *Griffiths and Linden* [1981]. As noted by *Tartinville et al.* [1998], low-resolution C-grid models usually perform mode four instabilities for this experiment due to the averaging of rotational terms. In contrast to this, B-grid models are able to reproduce the mode two instability, when high-order advection schemes with low numerical dissipation are used.
This test case will be used here for assessing the quality of various advection schemes for momentum and tracers. Therefore, the set-up is briefly described here, for a deeper description, see *Tartinville et al.* [1998].
The domain is quadratic with $L_x = L_y = 30$ km and has a flat bottom with $H = 20$ m. All four lateral boundaries are open. All frictional processes are neglected. The simulation is initialised with $u = v = 0$ and $\zeta = 0$, and the initial salinity distribution is

$$S = \begin{cases} 1.1\left(\frac{d}{d_0}\right)^8 + 33.75 & \text{for } d < d_0 \\ 34.85 & \text{else} \end{cases} \tag{5.10}$$

with $d = ((x - L_x/2)^2 + (y - L_y/2)^2)^{1/2}$ and $d_0 = 3$ km. A linearised equation of state is used for calculating the density:

$$\rho = \rho_0 + \alpha_S(S - S_0) \tag{5.11}$$

with $\rho_0 = 1025$ kg m^{-3}, $S_0 = 33.75$ psu and $\alpha_S = 0.78$ kg m^{-3}psu^{-1}.
The run time for the simulation is 6 days.

Outside the domain, a four point wide relaxation zone (sponge layer) has been implemented (see *Martinsen and Engedahl* [1987]) in which sea surface elevation and salinity are relaxed towards initial values.
After an adjustment period, the flow should be clockwise near the surface and anti-clockwise near the bottom.
In figures 5.18 – 5.22 the flow state after 6 days is shown for the following five different advection schemes and model resolutions:

1. Multidimensional first-order upstream scheme for momentum advection and directional split TVD-Superbee scheme, see equation 4.63 for salinity. The horizontal resolution was $\Delta x = \Delta y = 1000$ m and $N = 20$ vertical layers were used. For results, see figure 5.18.

2. Directional-split TVD-P2-PDM scheme, see equation 4.61, for both, momentum and salinity. The horizontal resolution was $\Delta x = \Delta y = 1000$ m and $N = 20$ vertical layers were used. For results, see figure 5.19.

3. Directional-split TVD-Superbee scheme, see equation 4.63, for both, momentum and salinity. The horizontal resolution was $\Delta x = \Delta y = 1000$ m and $N = 20$ vertical layers were used. For results, see figure 5.20.

4. Directional-split TVD-Superbee scheme, see equation 4.63, for both, momentum and salinity. The horizontal resolution was $\Delta x = \Delta y = 500$ m and $N = 20$ vertical layers were used. For results, see figure 5.21.

5. Directional-split TVD-Superbee scheme, see equation 4.63, for both, momentum and salinity. The horizontal resolution was $\Delta x = \Delta y = 500$ m and $N = 40$ vertical layers were used. For results, see figure 5.22.

It can be clearly seen that all these 5 numerical experiments generate wave number four instabilities instead of the physically more realistic wave number 2 instability. The reason for this persistent occurence of wave number four instabilities could be the quadratic structure of the grid, which does from the beginning of the experiment on trigger such wave number four instabilities. It is however not easy to understand why even for the high resolution case with $\Delta x = \Delta y = 500$ m, no sign of a wavenumber two instability is visible. This feature surely needs to be further investigated in the future.
Despite this, significant differences can be seen for the five numerical experiments carried out here. The most striking feature is the difference between experiments 1 and 3. The only difference is the way how the momentum advection is discretised, with a multidimensional upstream scheme in experiment 1 and a directional-split

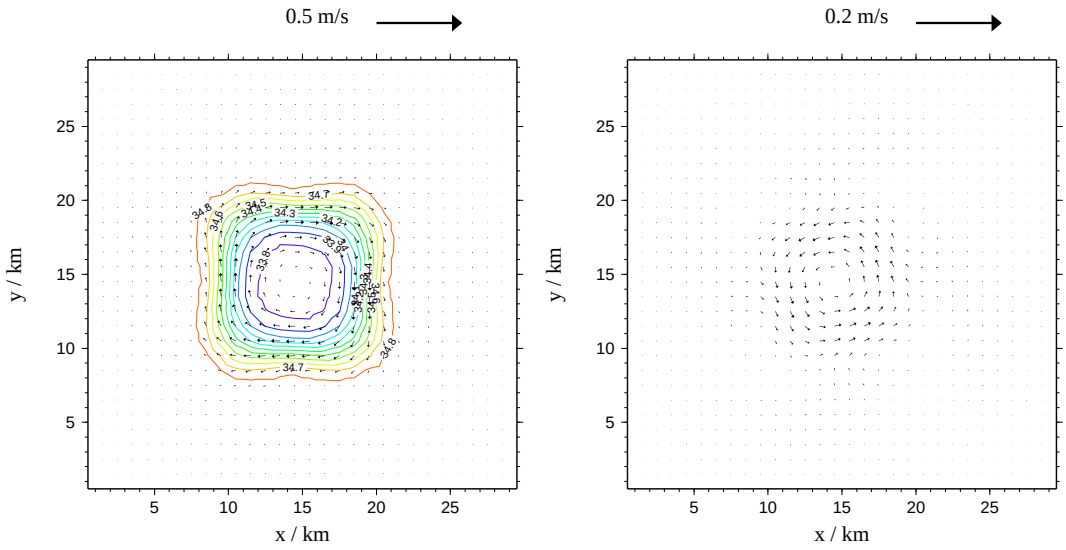

Figure 5.18: Salinity and current vectors for the freshwater eddy experiment 6 days after initialisation. Left: surface salinity and current vectors; right: bottom current vectors. Momentum advection has been discretised by the multidimensional upwind scheme, salinity advection with the TVD-Superbee directional-split scheme.

TVD-Superbee scheme in experiment 3. The upstream scheme is obviously so dissipative, that almost no baroclinic instability can develop. In contrast to this, the TVD-Superbee scheme allows for a significant wavenumber four instability. Regarding baroclinic instabilities, experiment 2, with directional-split TVD-P2-PDM advection schemes for momentum and salinity, lies in between experiment 1 and 3. The reason for this is that the Superbee scheme is less dissipative than the P2-PDM, although the latter is on order of approximation higher. It should be noted however, that the Superbee scheme tends to over-exaggerate gradients, as shown in sections 4.7.5.1 and 4.7.5.2.
As expected, the simulations 4 and 5 with increased horizontal resolution do results in more pronounced baroclinic instabilities than the experiments 1 - 3 with lower resolution. The latter two experiments generate approximately the same amount of instabilities, which means that the vertical resolution is not important for this friction-free experiment.
The time series of total kinetic energy shown in figure 5.23 confirm the results discussed above.

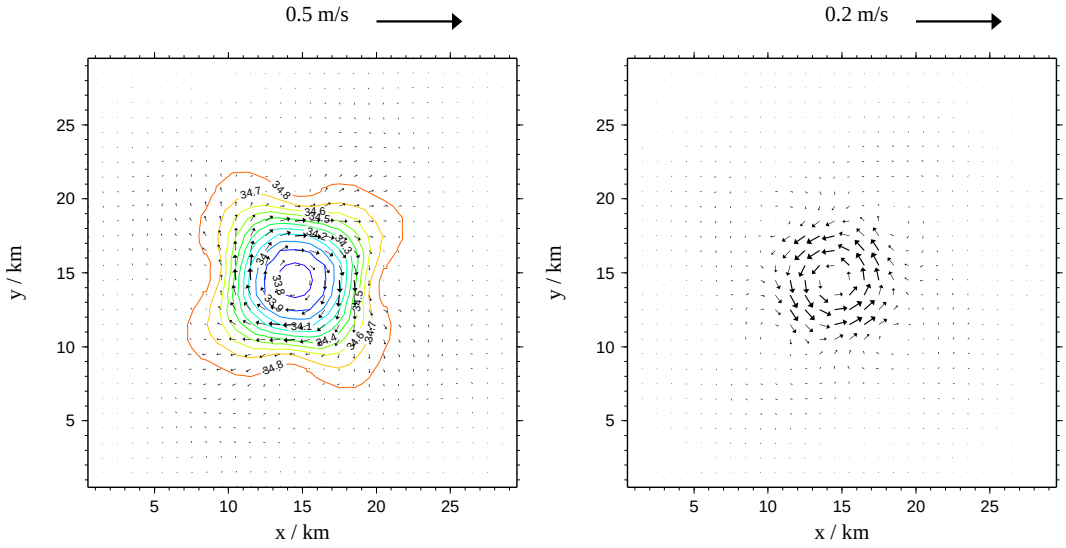

Figure 5.19: As figure 5.18, but momentum and salinity advection have both been discretised with the TVD-P2PDM directional-split scheme.

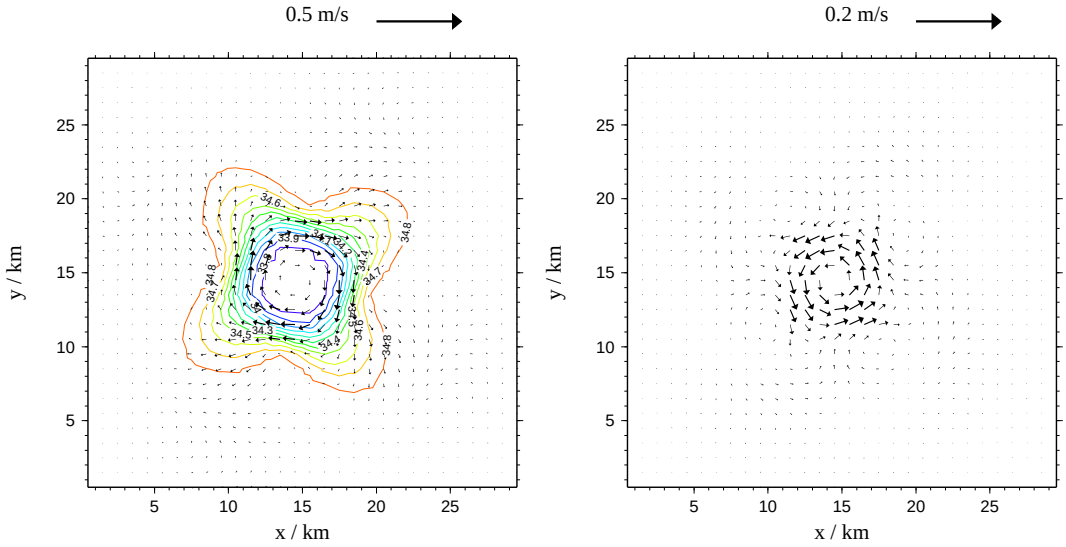

Figure 5.20: As figure 5.18, but momentum and salinity advection have both been discretised with the TVD-Superbee directional-split scheme.

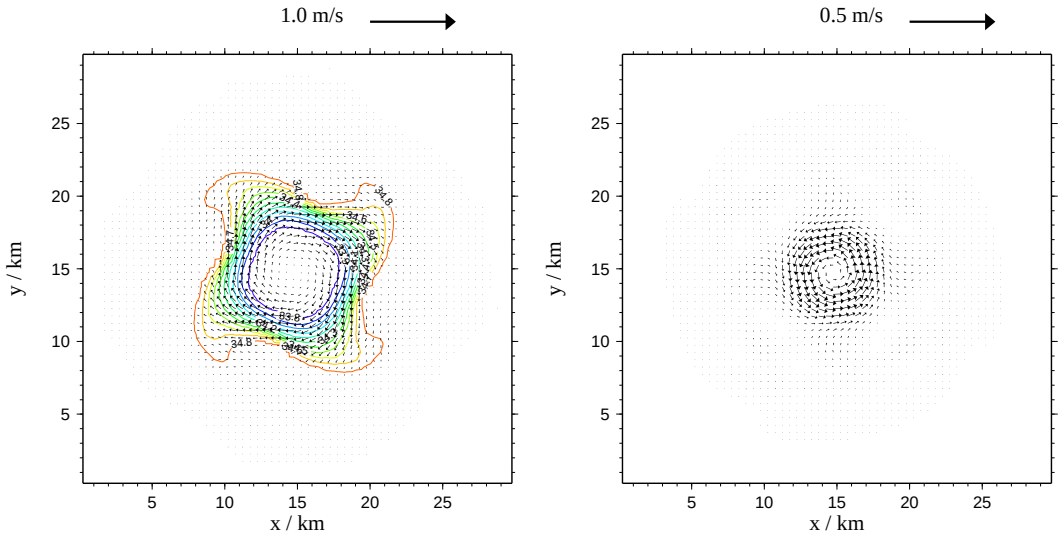

Figure 5.21: As figure 5.18, but momentum and salinity advection have both been discretised with the TVD-Superbee directional-split scheme. An increased horizontal resolution with $\Delta x = \Delta y = 500$ m has been used.

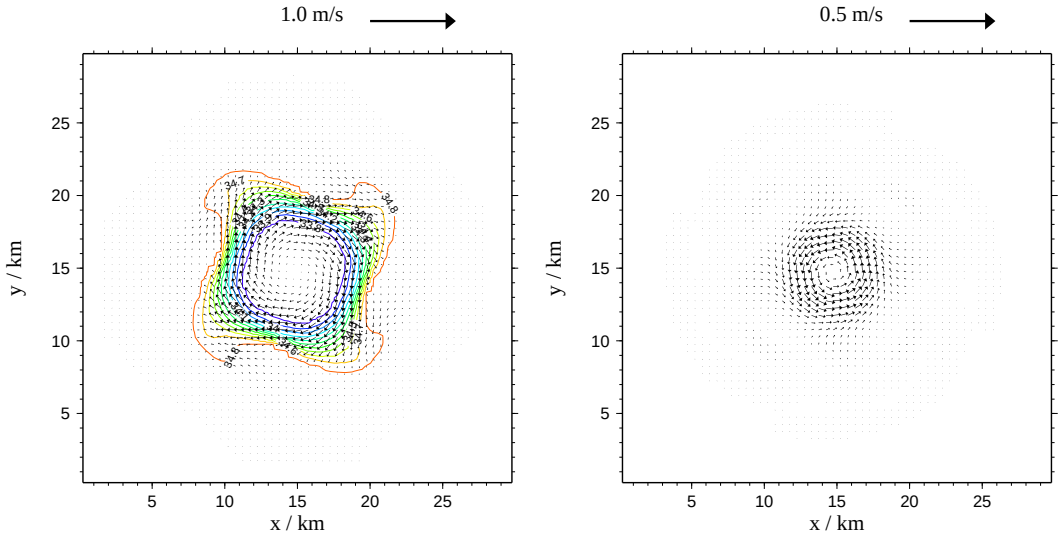

Figure 5.22: As figure 5.21, but the number of vertical increments has been $N = 40$ instead of $N = 20$.

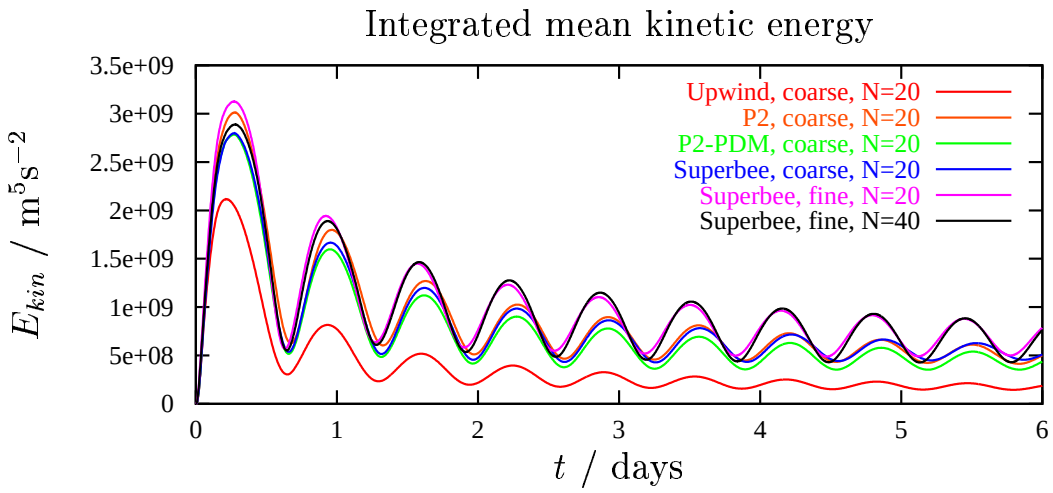

Figure 5.23: Time series of integrated mean kinetic energy for the freshwater eddy experiment obtained with various advection schemes and numerical resolutions.

Chapter 6

Realistic 3D applications

6.1 Sylt-Rømø Bight

In this section, the ability of the model to properly simulate the dynamics in areas with considerable drying and flooding of inter-tidal flats is demonstrated. For doing so, the tidal currents inside a wadden sea embayment are simulated. This embayment is situated in the North Sea between the Danish island Rømø and the German island Sylt at about 55° N and 8° E and covers an area of about 300 km^2, see figure 6.1. The embayment is closed by marshlands to the east and artificial dams to the north and south. The tidal channel (Lister Tief) leading into the embayment has a width of about 2.5 km with a maximum depth of more than 30 m. Inside the Bight, the Lister Tief branches into the Lister Ley to the south, the Hoyer Dyb to the south-east and the Rømø Dyb to the north-east. The extensive tidal flat east of the Hoyer Dyb is called Jordsand, a former small island which is eroded now. An interesting feature of the Sylt-Rømø Bay is the shallow embayment at the northern peak of Sylt, the so-called Königshafen.
The main forcing of the currents is the predominant M_2 tide with a tidal period of $T_4 = 44714$ s. There is no considerable freshwater inflow into the embayment, so that the water column is generally well mixed. Because of these ideal conditions (simple forcing, closed, well-mixed) the Sylt-Rømø bight is a good test case for wadden sea models. Several authors have carried out simulations in this embayment, see e.g. *Dick* [1987], *Burchard* [1995], *Schneggenburger et al.* [2000].
For the present simulation, a bathymetry data set with a horizontal resolution of 200 m × 200 m is used (see figure 6.1). An equidistant vertical discretisation with $N = 20$ σ layers is chosen. The micro time step is $\Delta t_m = 4.5$ s and with $M = 10$, the macro time step is Δt= 45 s. A tidal forcing considering 8 harmonic tides is applied until a periodically steady state is reached. The periods of the harmonic tides which

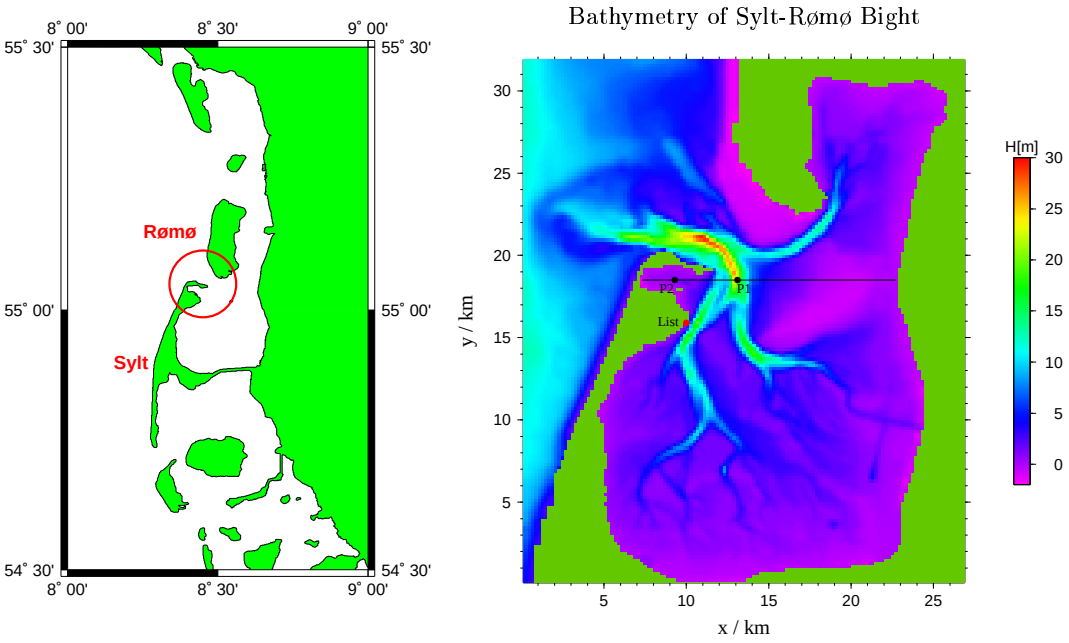

Figure 6.1: Sylt-Rømø Bight: left: Schematic overview over the west coast of Schleswig-Holstein (Germany) and Southern Jutland (Denmark) with the Sylt-Rømø Bight; right: 200 × 200 m bathymetry as used in the numerical model. The purple colour indicates inter-tidal flats. The points P1 and P2 show the locations where the temporal evolution of the water column is shown, see figures 6.7 and 6.8. Along the connecting line, sections for u, v, and ν_t are shown in figures 6.9-6.12.

are not over tides of the M_2 tide have been modified for this short term study such that the tidal forcing is periodic with the M_2 tide, for details, see *Burchard* [1995]. The minimum depth is chosen as $D_{\min} = 0.05$ m and the critical depth below which some physical processes are restricted is $D_{crit} = 0.2$ m. Wind forcing and surface heat fluxes are neglected.

The turbulence closure model used here is the k-ε model in combination with the algebraic second-moment closure by *Canuto et al.* [2001], see also *Burchard et al.* [2001]. As surface and bottom boundary conditions, Neumann flux conditions for the turbulent kinetic energy k and the dissipation rate are chosen, see *Burchard and Petersen* [1999].

Here, some results of the fifth tidal period after initialising the model from rest are shown. Basically, two model runs are compared, which only differ in the numerical treatment of the three-dimensional momentum advection. One method is the first-

order upstream method, here applied as a multidimensional one-step procedure, see section 4.7.1.1, which is known to be highly diffusive. The other method is the direction-split TVD-P_2-PDM method (also known as the ULTIMATE QUICKEST scheme), see equation (4.61).
In figures 6.2 - 6.5, vector plots of surface currents velocities for four phases of the tidal period are shown, during full flood (figure 6.2), high water (figure 6.3), full ebb (figure 6.4) and low water (figure 6.5). As reference, zero, maximum, zero and minimum sea surface elevation, respectively, at the harbour of List (see figure 6.1) have been chosen.
In the following discussion of the surface currents, the differences due to the two different advection schemes are briefly highlighted. During flood (figure 6.2) with high current speeds mostly in the deeper channels, the velocities are higher and the currents more jet-like for the TVD scheme. This is clearly seen in the deep part of the Lister Ley south-east of List. Furthermore, a recirculation cell appears at the entrance to the Königshafen for the TVD scheme which is not visible for the upstream scheme. All these difference can easily be explained by the higher numerical diffusion caused by the upstream scheme.
During high water (figure 6.3), flood current still dominate in the southern Lister Tief, but in the northern part ebb currents have already set on. This feature is continuing into the tidal channels branching from the Lister Tief, ebb in the Rømø Dyb and still flood in the Lister Ley and the Hoyer Dyb. The recirculation cell near the entrance to the Königshafen is now much more developed, with a more pronounced structure for the TVD scheme.
During full ebb (figure 6.4), the most interesting flow feature is the recirculation cell which is developing at the northern part of Sylt for the TVD advection scheme, and which is not visible for the upstream scheme. Again, currents are more constrained for the TVD-scheme.
During low water (figure 6.5), when ebb currents are still dominant, the recirculation cell is further developing, which more intensity for the TVD scheme.
Tidal mean vertically averaged residual currents can be calculated as follows, see *Dick and Soetje* [1990]:

$$u_r = \frac{\int_T U\,dt}{\int_T D\,dt}, \qquad v_r = \frac{\int_T V\,dt}{\int_T D\,dt}. \tag{6.1}$$

These residual currents are shown in figure 6.6. General features obtained with both advection schemes are low residual currents in the deep channels and high residual currents at the shallow edges of these channels. Ebb-dominance in the northern part of the Lister Tief and flood dominance in its southern part could already be expected

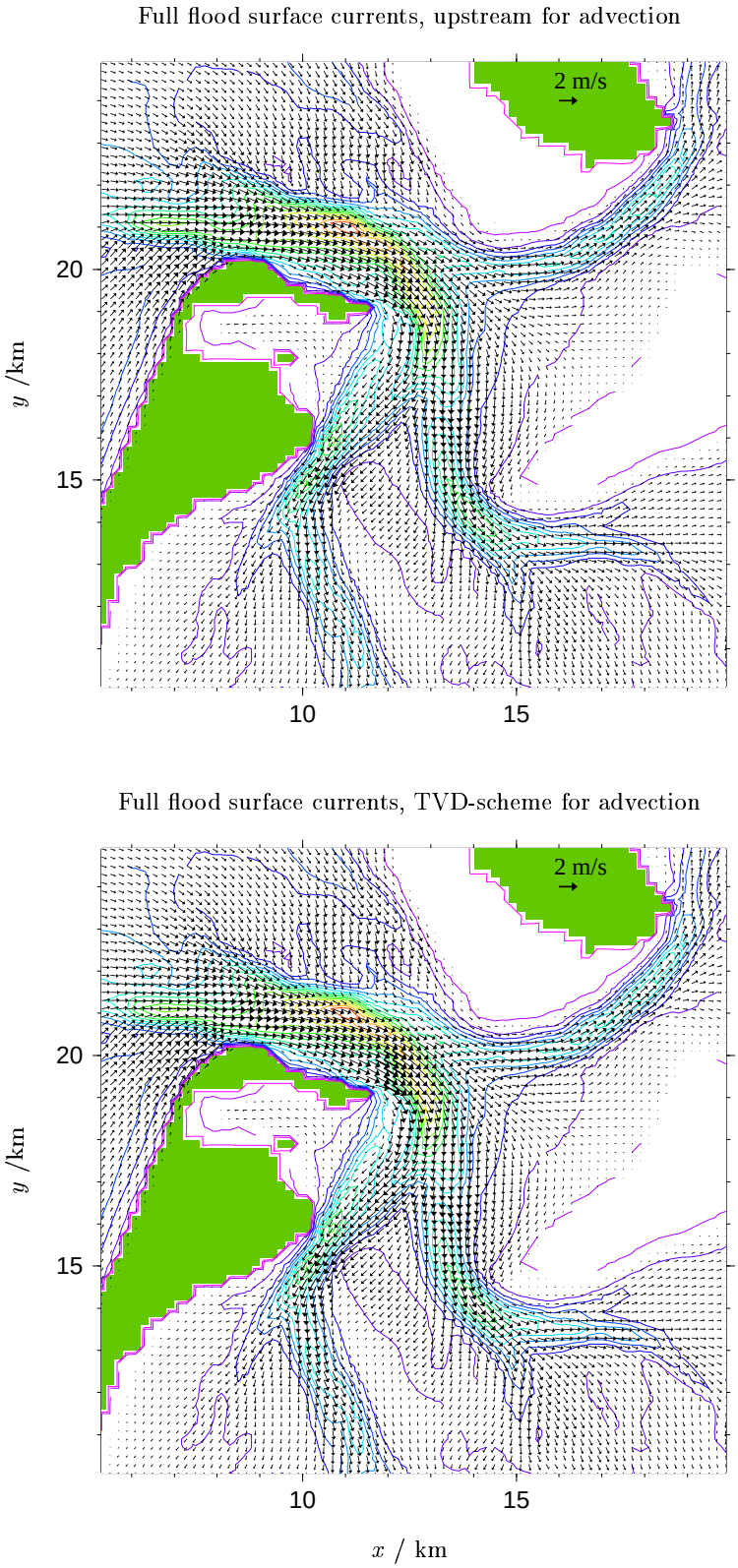

Figure 6.2: Full flood surface currents in the Sylt-Rømø Bight. Left: First-order upstream, multi-dimensional scheme for momentum advection; right: Directional-split TVD-P_2-PDM scheme for momentum advection.

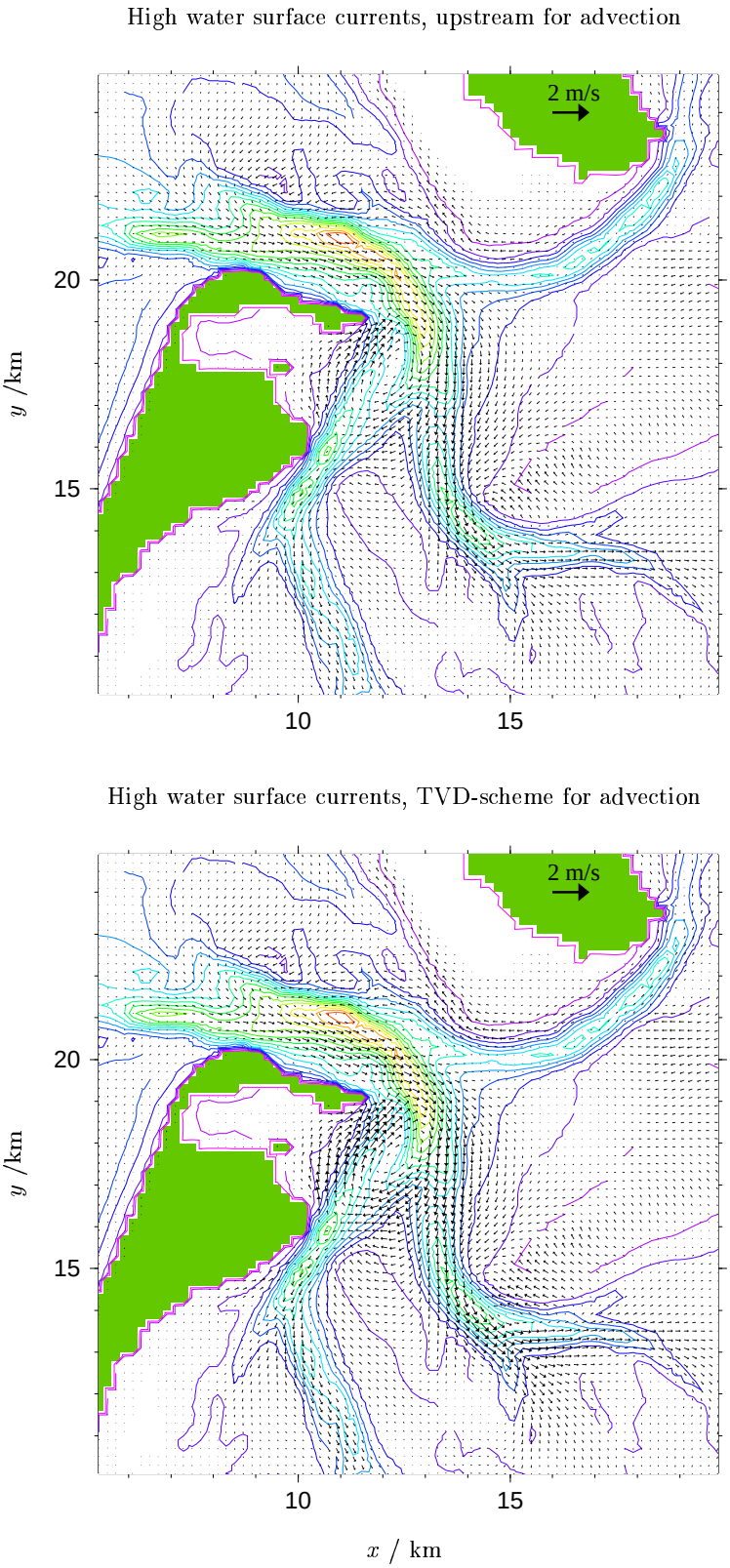

Figure 6.3: High water surface currents in the Sylt-Rømø Bight. Left: First-order upstream, multi-dimensional scheme for momentum advection; right: Directional-split TVD-P_2-PDM scheme for momentum advection.

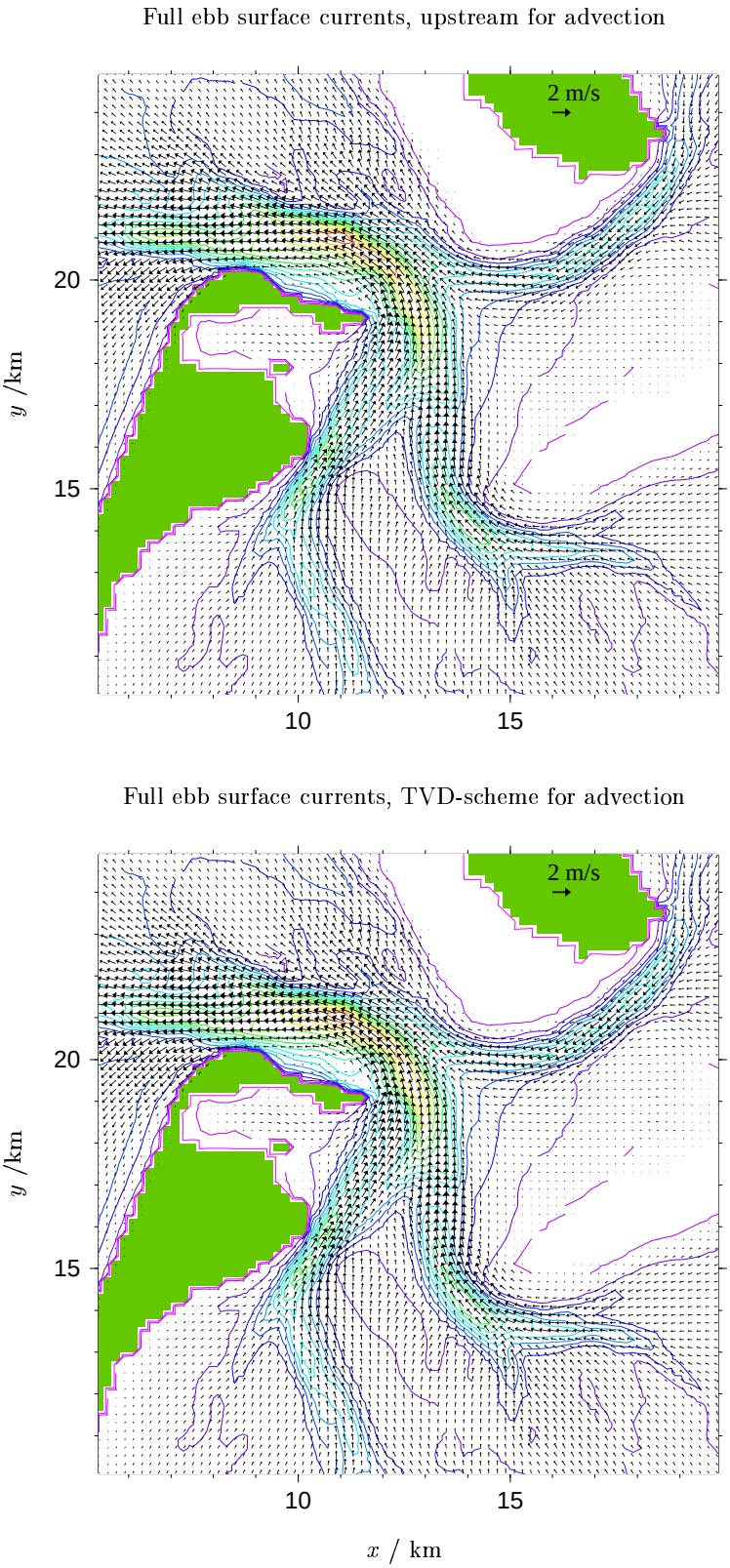

Figure 6.4: Full ebb surface currents in the Sylt-Rømø Bight. Left: First-order upstream, multi-dimensional scheme for momentum advection; right: Directional-split TVD-P_2-PDM scheme for momentum advection.

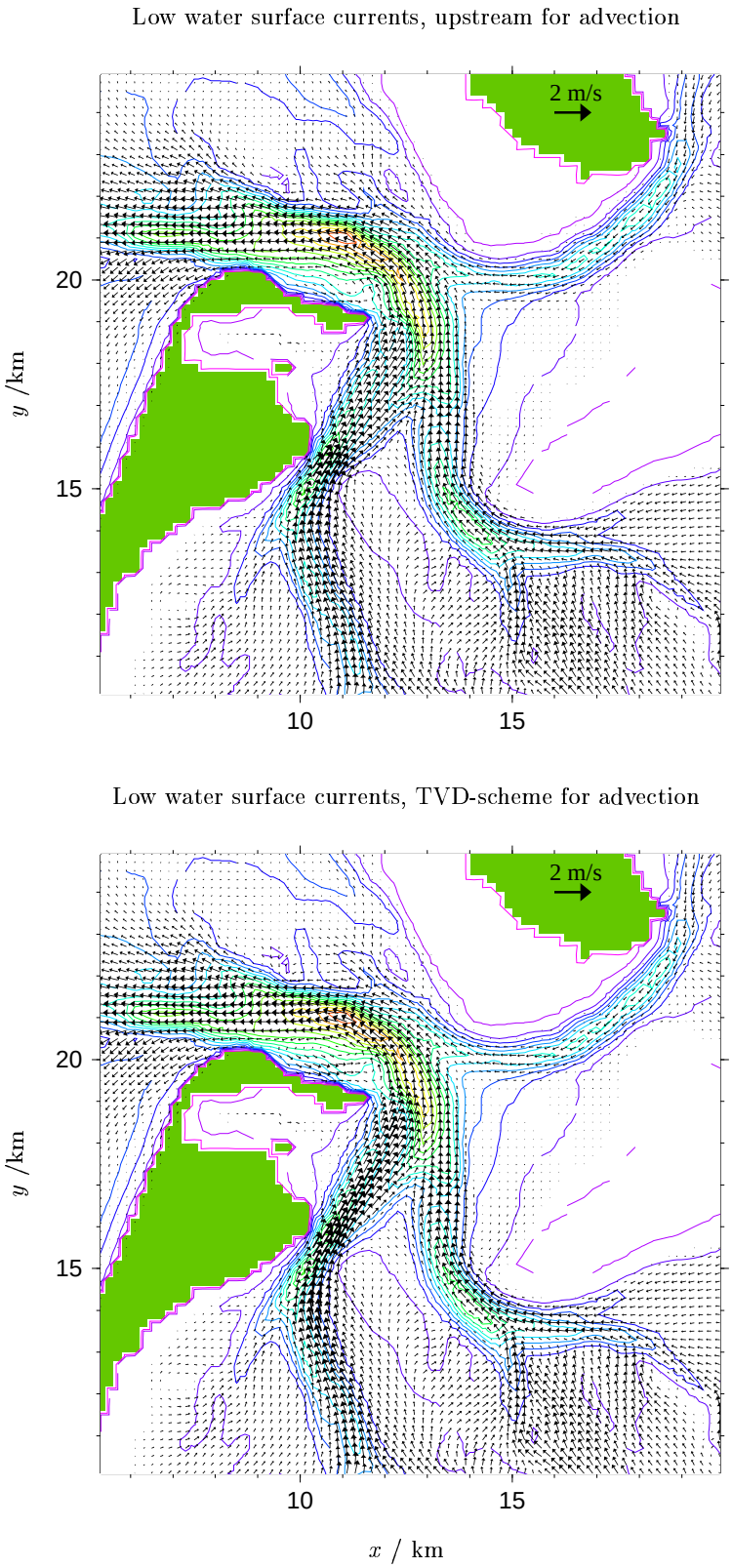

Figure 6.5: Low water surface currents in the Sylt-Rømø Bight. Left: First-order upstream, multi-dimensional scheme for momentum advection; right: Directional-split TVD-P_2-PDM scheme for momentum advection.

from figure 6.2. The strongest residual currents occur at the sand spit north of the Königshafen where they seem to stabilise this fragile sandy structure. As already seen from the instantaneous surface currents, structures are more pronounced when using the TVD scheme for momentum advection.

It should be noted here, that these features would become even more pronounced when using the Superbee instead of the P_2-PDM limiter, see equation (4.63). However, we refrained from this since this limiter has shown to be too anti-diffusive. One other thing to be noted is that we used so far the TVD-advection scheme only for the three-dimensional advection momentum advection of the internal mode, and not for the external mode, and not for the slow advection terms, see equation (2.20). It is not clear if the results would considerably improve when using the higher-order advection schemes also for these terms. In the steady-state flow, however, these two vertically integrated low-order advection terms would fully cancel out and thus high-order advection would be active, only.

In order to demonstrate the vertical structure of the flow in time the physical water evolution is shown in the two points P1 (deep water, see figure 6.7) and P2 (shallow water, see figure 6.7). Furthermore, current speed and eddy viscosity are shown along a zonal cross-section through these two points for full flood (see figure 6.9), high water (see figure 6.10), full ebb (see figure 6.11) and low water (see figure 6.12). For the location of the points P1 and P2 and the cross-section, see figure 6.1.

In order to generate these plots, the physical values has been transferred from the σ grid to a fine resolution vertical grid in z-coordinates by linear interpolation. The plots 6.7 - 6.12 show quite clearly that the model computes various details of the physics of the flow. In figure 6.7, the flood current (negative v is more pronounced than the ebb current (positive v), with the consequence that the turbulence reaches a higher level during flood. Eddy viscosity and turbulent kinetic energy show a clear peak before the onset of the flood current ($t/T_4 = 0.05$). Such an enhanced turbulence after the flow reversal has already been shown by *Savioli and Justesen* [1997] when simulating oscillatory sediment-laden flows with a k-ε model. This could have implications, when simulating suspended matter dynamics, see e.g. the laboratory studies by *Ribberink and Al-Salem* [1992].

The model results at point P2 demonstrate that sensible physical results are obtained even in areas where the tidal range is much larger than the mean water depth.

In figures 6.9 - 6.12, only the cross-sections above $z = -3$ m are shown in order to demonstrate drying and flooding processes. It is clearly seen that some water (here at least 5 cm due to the setting of $D_{\min}$) is left on the tidal flats. Significantly reducing the thickness of this remaining layer would require a reduced time step in order to avoid numerical instabilities.

It can be concluded here, that GETM is able to stably simulate currents and turbu-

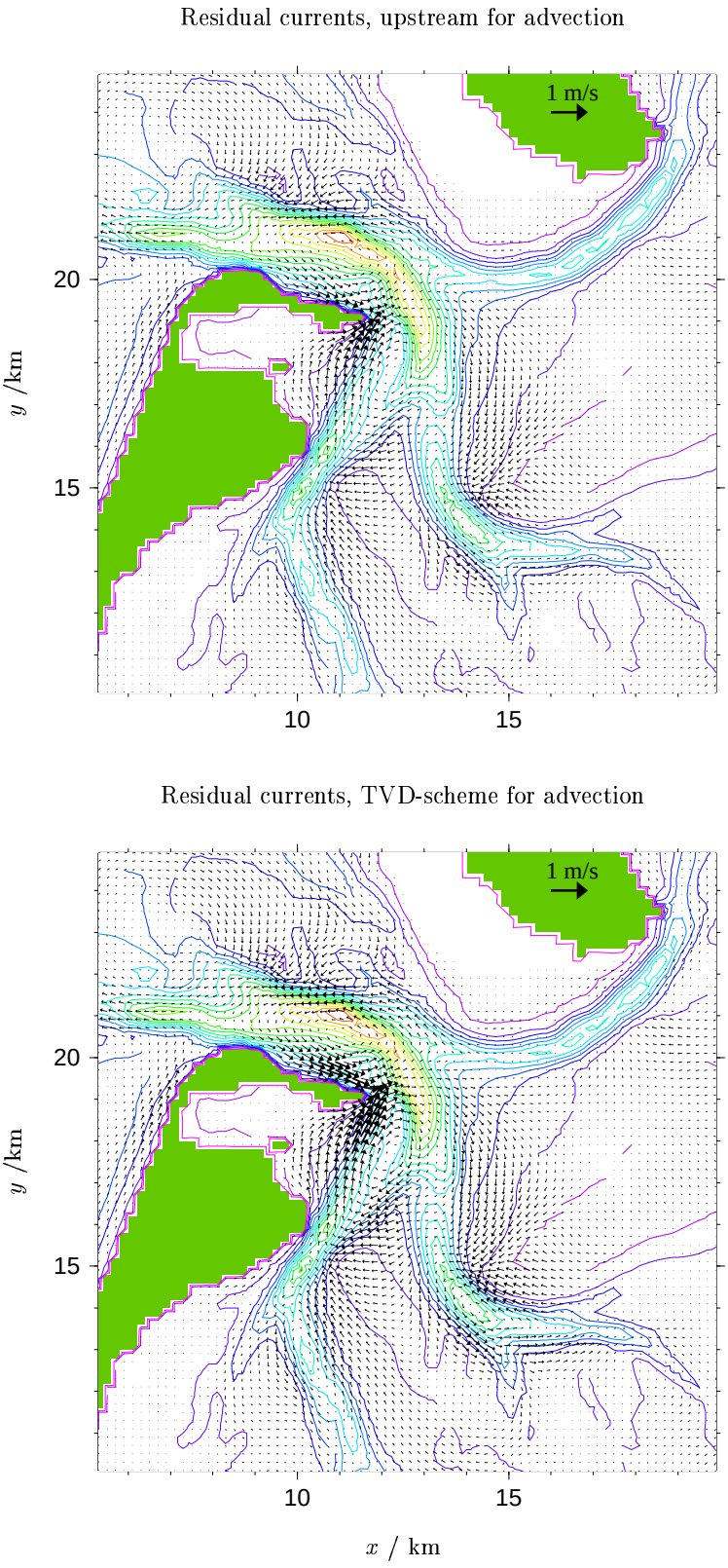

Figure 6.6: Residual currents in the Sylt-Rømø Bight. Left: First-order upstream, multi-dimensional scheme for momentum advection; right: Directional-split TVD-P_2-PDM scheme for momentum advection.

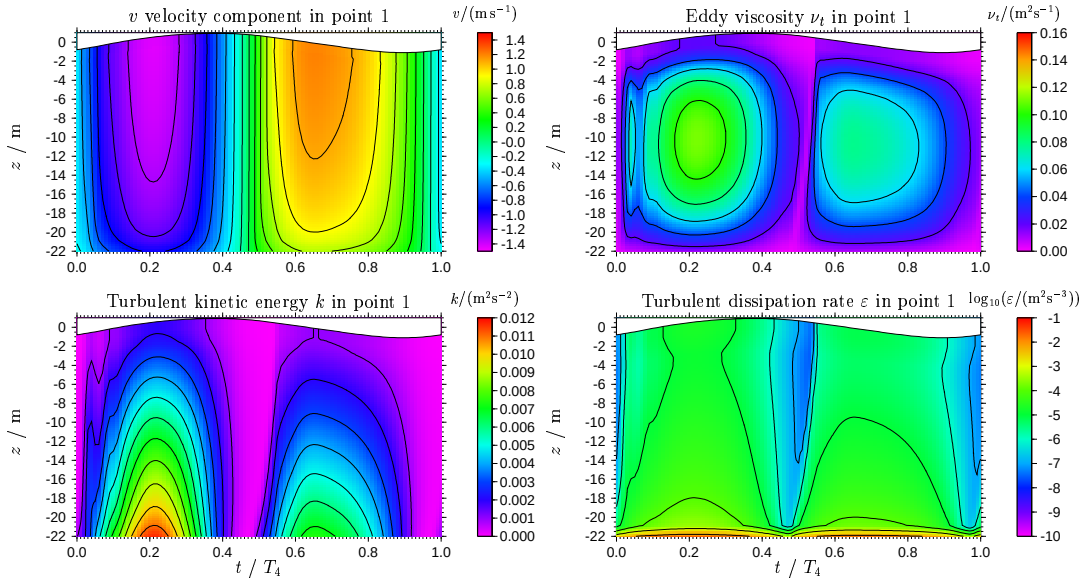

Figure 6.7: West-east velocity component u, eddy viscosity ν_t, turbulent kinetic energy k and turbulent dissipation rate ε during one tidal cycle at point 1.

lence in this wadden sea embayment with extensive tidal flats. The realism of these simulations clearly depends on the horizontal resolution which is here relatively coarse with $\Delta x = \Delta y = 200$ m and does not resolve all characteristic details of the topography. Furthermore, more realistic boundary conditions would be needed. For several applications, also the consideration of surface waves would increase the predictability of the model, see *Schneggenburger et al.* [2000].

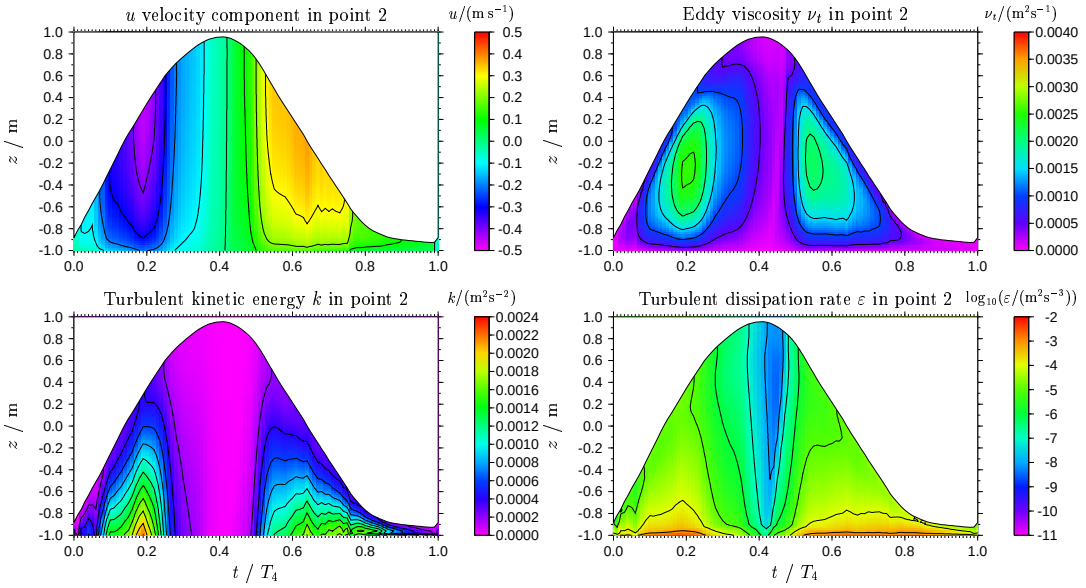

Figure 6.8: West-east velocity component u, eddy viscosity ν_t, turbulent kinetic energy k and turbulent dissipation rate ε during one tidal cycle at point 2.

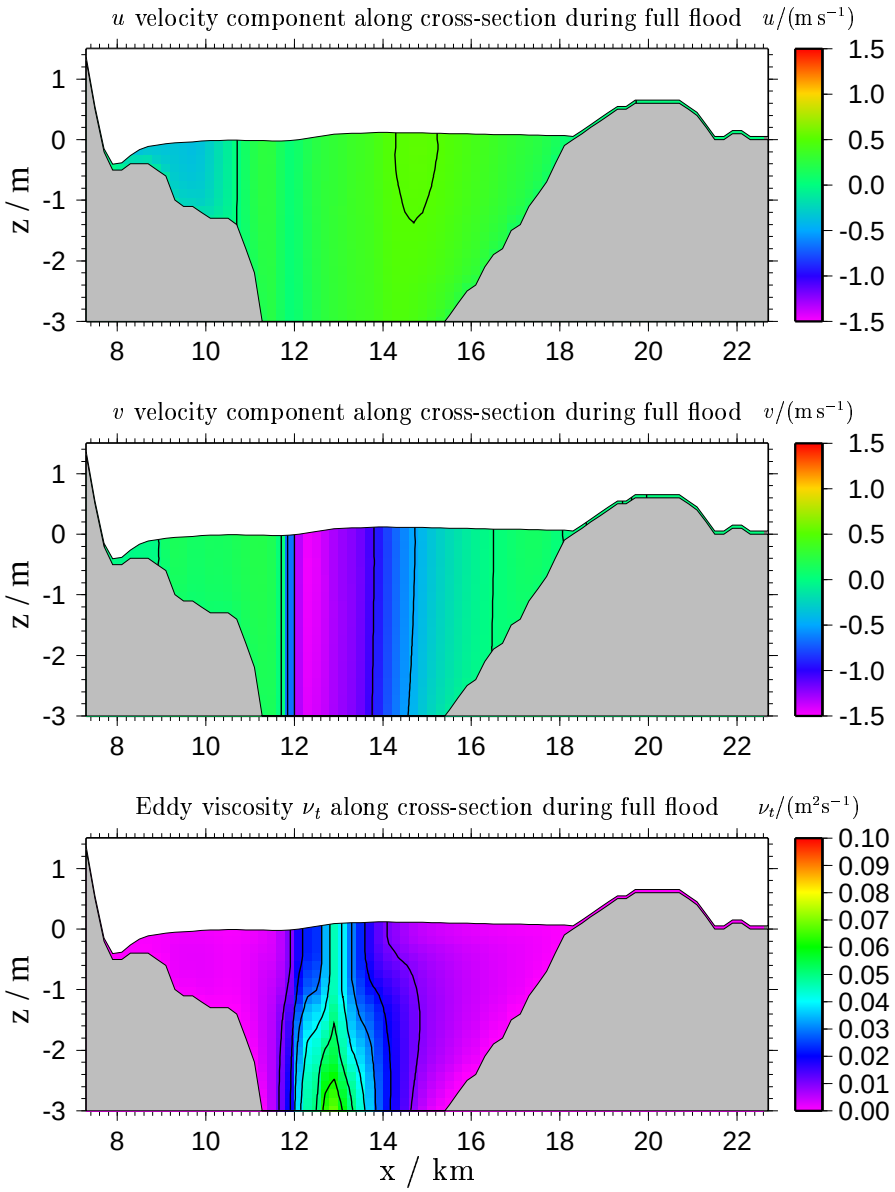

Figure 6.9: Velocity components u and v and eddy diffusivity along a cross-section (see figure 6.1) during full flood. Only the upper 3 m are shown.

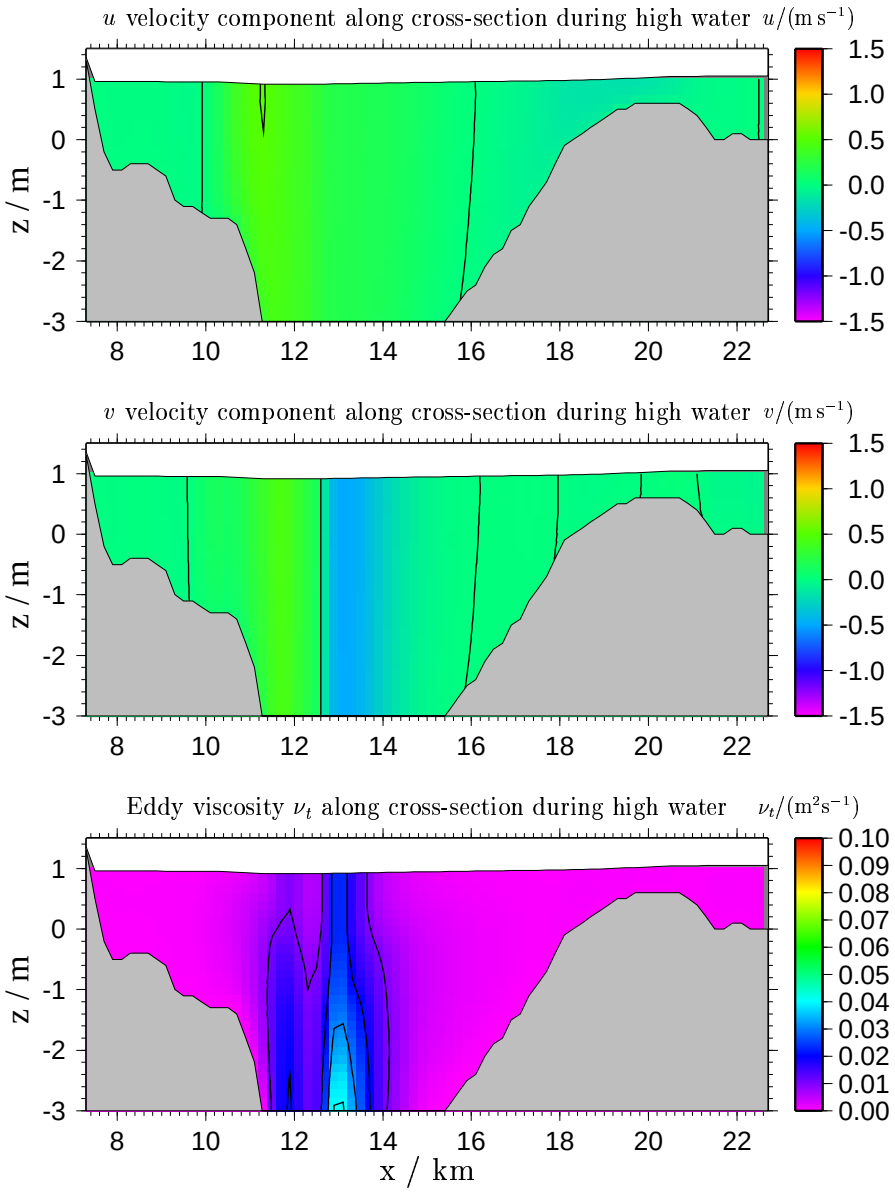

Figure 6.10: Velocity components u and v and eddy diffusivity along a cross-section (see figure 6.1) during high water. Only the upper 3 m are shown.

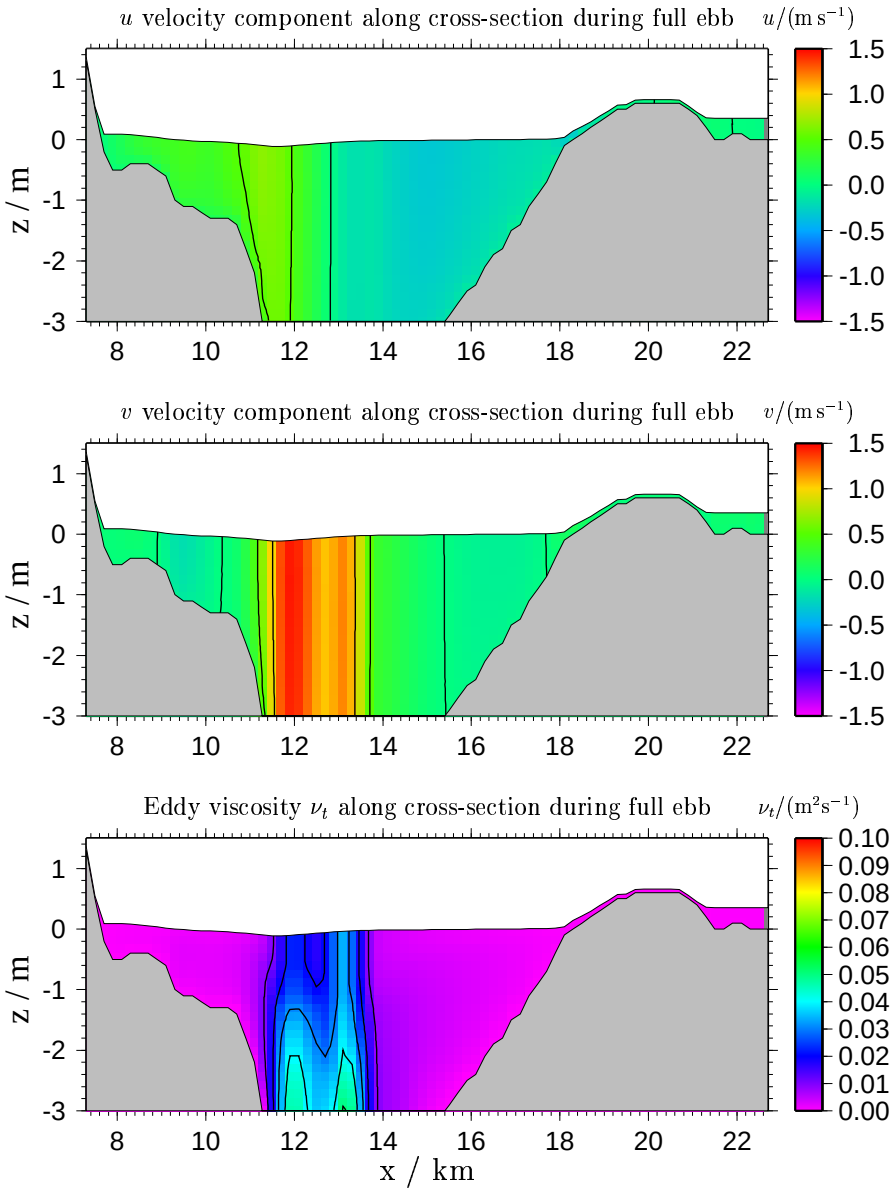

Figure 6.11: Velocity components u and v and eddy diffusivity along a cross-section (see figure 6.1) during full ebb. Only the upper 3 m are shown.

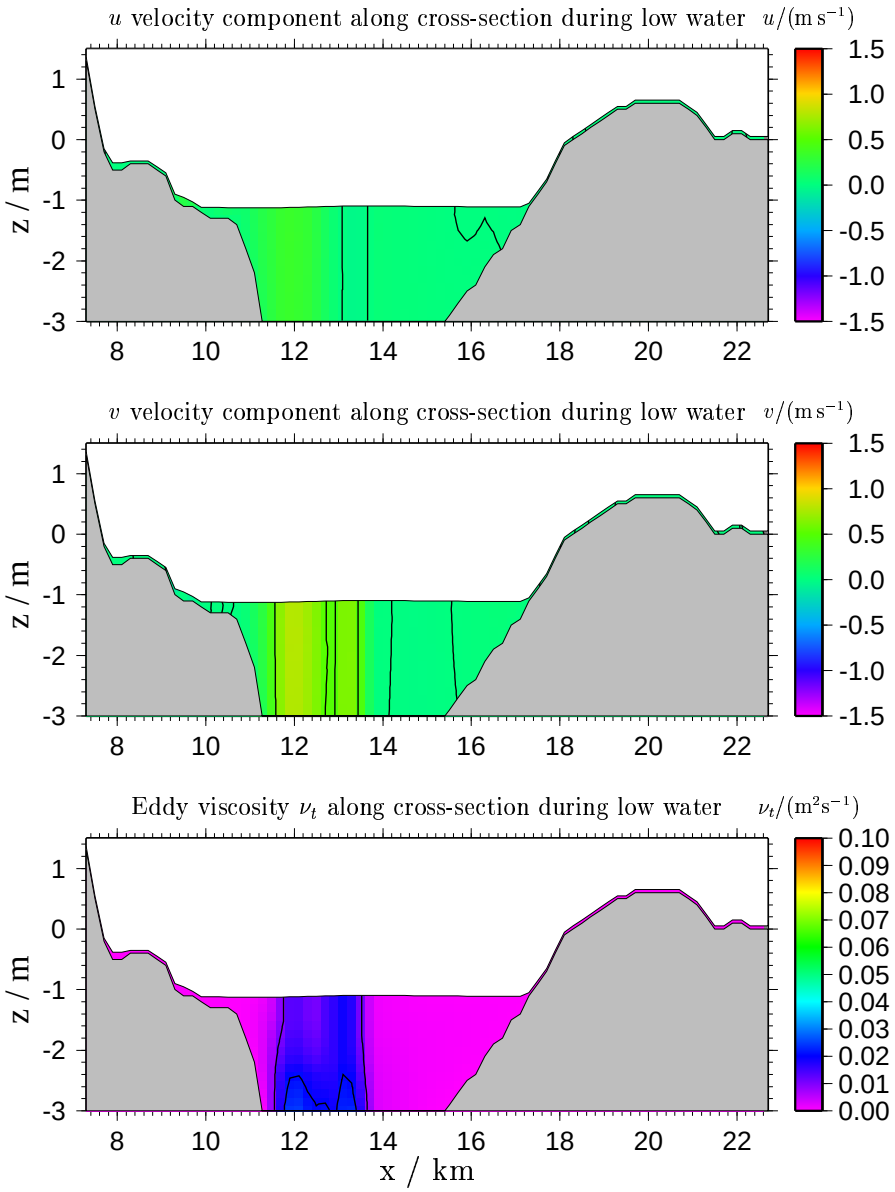

Figure 6.12: Velocity components u and v and eddy diffusivity along a cross-section (see figure 6.1) during low water. Only the upper 3 m are shown.

6.2 Lake Constance

In order to test the ability of the model for reproducing baroclinic features such as up-welling and internal seiches, stratified flow in a real lake is simulated. For this, the Lake Constance is chosen, situated north of the Alps at about 47°40' N, 9°20' E. Its surface is about 395 m above sea level, th maximum depth is about 250 m. The lake consists of three major basins, the Upper Lake Constance, the Lower Lake Constance and Lake Überlingen. The Rhine river flows through the Upper and Lower Lake which are dynamically separated by a narrow and shallow connecting channel. Upper Lake Constance and Lake Überlingen are connected by a wide passage with a sill depth of about 100 m. In the simulations carried out here, only the Upper Lake Constance and Lake Überlingen (maximum depth 153 m) are considered. After rotating the bathymetry by 32° in anti-clockwise direction in order to obtain a minimum of land points, and discretising the bathymetry with 500 m × 500 m Cartesian grid boxes, a picture as shown in figure 6.13 arises.

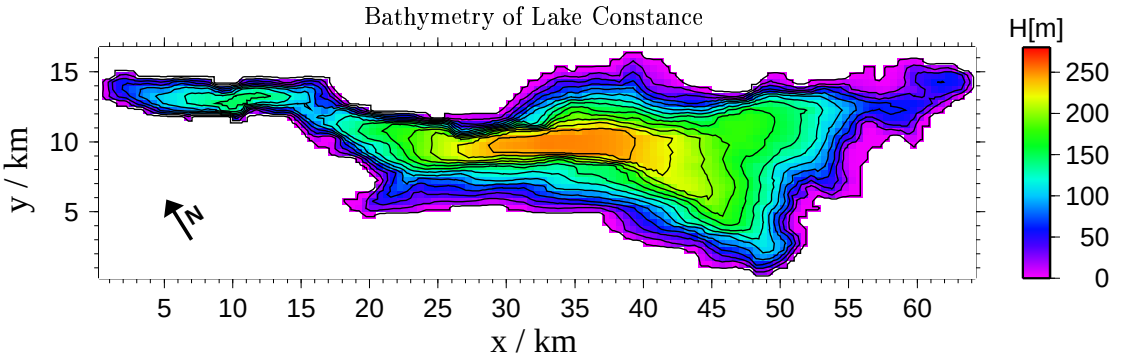

Figure 6.13: Bathymetry data set for Lake Constance. For generating this 500 × 500 m bathymetry, the data have been rotated by 32° in anti-clockwise direction in order to obtain a minimum of land points.

The idealised situation which is simulated here has been adapted from *Wang* [2001], who used this scenario for testing various numerical schemes for the advection of temperature and momentum. The simulation is initialised with a flow at rest and a horizontally homogeneous temperature distribution with the following typical vertical profile given in °C:

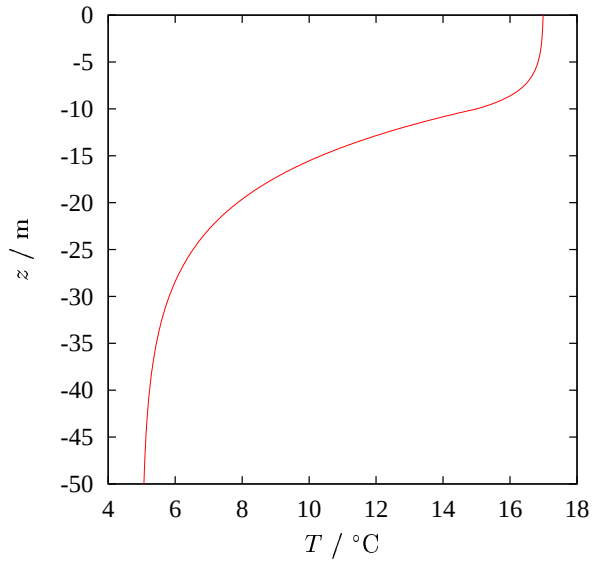

Figure 6.14: Initial temperature profile for the Lake Constance simulation.

$$T = \begin{cases} 17 - 2\exp\left(-\frac{z+10}{2}\right), & \text{for } z \geq -10 \text{ m} \\ \\ 5 + 10\exp\left(-\frac{z+10}{8}\right), & \text{for } z < -10 \text{ m}, \end{cases} \tag{6.2}$$

see figure 6.14. This initial profile is then linearly interpolated into the model grid. For constructing the latter, general vertical coordinates as introduced in section 3.1.1 have been used. The settings for the upper γ-coordinates (see equation (3.7)) are chosen here such that the critical depth is D_γ=20 m, and the zooming factors are d_u=2 and d_l=1. The resulting grid is shown for a section across the lake at $x = 38.75$ km in figure 6.15. It can be seen that the near-surface grid box heights do only weakly depend on the actual water depth.
The model is forced by a constant surface wind stress of $\tau_s = 0.035$ N m^{-2} which corresponds to a 10 m wind of about 4 m s^{-1}. The direction of the wind is 302° (from about NW), i.e. along the major axis of the lake. This wind blows with a constant strength in time and space for two days and is then switched off.
For the model simulation presented here, the following numerical discretisation schemes have been used:

- Horizontal and vertical advection TVD schemes with Superbee limiter and

Strang [1968] splitting for momentum and temperature according to equation (4.63).

- Internal pressure gradient discretisation according to *Song* [1998], see equation (4.95).

- Coriolis term averaging according to *Espelid et al.* [2000], see equations (4.98) and (4.99).

As micro time step, Δt_m=6 s and a split factor of $M = 10$ have been chosen, such that the external time step is Δt=60 s. In total, 10 days have been simulated, which mens that the simulation went on after the ceasing of the wind for further eight days without external forcing.
The model results are shown in figures 6.16 - 6.21.
After two days, when the wind along the lake ceases, a typical coastal up-welling situation is established. The sea surface temperature (SST) along the northern shore of the Upper Lake Constance is reduced by up to 5 K. The cross-section through the Upper Lake reveals that convective overturning takes place near the northern shore such that the water is fully mixed in the upper 5 m. In Lake Überlingen, a jet-like surface current has developed which continues into the Upper Lake as a coastal current along the southern shore. The coldest SST of below 8 °C occurs in Lake Überlingen, where then surface currents pushed the upper water masses into the Upper Lake. In the northern half of the Upper Lake, current pattern are visible which coincide with the meso-scale structure of the temperature field (see figure 6.16).
After four days, i.e. two days after the wind ceased, the surface waters are pushing back into Lake Überlingen such that now deeper water is up-welled in the eastern part of the lake. In the Upper Lake, an anti-cyclonic circulation is establishing, accompanied by down-welled isopycnals in the deep part of the lake (see figure 6.17).
During the following days, the anti-cyclonic circulation in the Upper Lake is enhancing, and also some meso-scale patterns become more pronounced. After eight days, a strong cyclonic eddy is propagating through the upper lake, accompanied by up-welling of isopycnals in its centre. This is partially visible in the cross-section through the lake, which cuts through the wake of the eddy (see figure 6.19). The situation at the end of the simulation period is dominated by a patch of warm water in the centre of the Upper Lake, surrounded by a strong anti-cyclonic circulation. In the other regions of the lake, geostrophically balanced meso-scale patterns exist (see figure 6.20).

Finally, temperature time series at a depth of about 10 m below the surface (initial position of steepest gradient) are extracted from the model results for six positions in the lake. These positions roughly coincide with the locations chosen by *Wang* [2001] for the same purpose. Compared to the *Wang* [2001] times series obtained with the same TVD schemes, the results shown in figure 6.21 are more damped, such that the amplitudes of the internal seiches are smaller. The present results do better compare to the results obtained by *Wang* [2001] for the first-order upstream advection scheme. This indicates that some additional mixing is effective here. This could be partially due to physical mixing by the k-ε model (in contrast to the fixed diffusivity profile used by *Wang* [2001]) or due to numerical diffusivity. Such numerical mixing could be caused by the steep bathymetry which has the consequence that adjacent grid boxes might have heights differing by a factor of more than 10. This can only be avoided by choosing a higher horizontal resolution. This is exactly what has been done by *Wang* [2001] who constructed a curvilinear grid with higher resolution across the lake. Since GETM also has the option for curvilinear grids, it would be interesting to study the effect of such a grid for this Lake Constance simulation.
It can be concluded for this present study that GETM allows for a stable and realistic simulation of stratified scenarios which steep bathymetry and small physical energy dissipation.

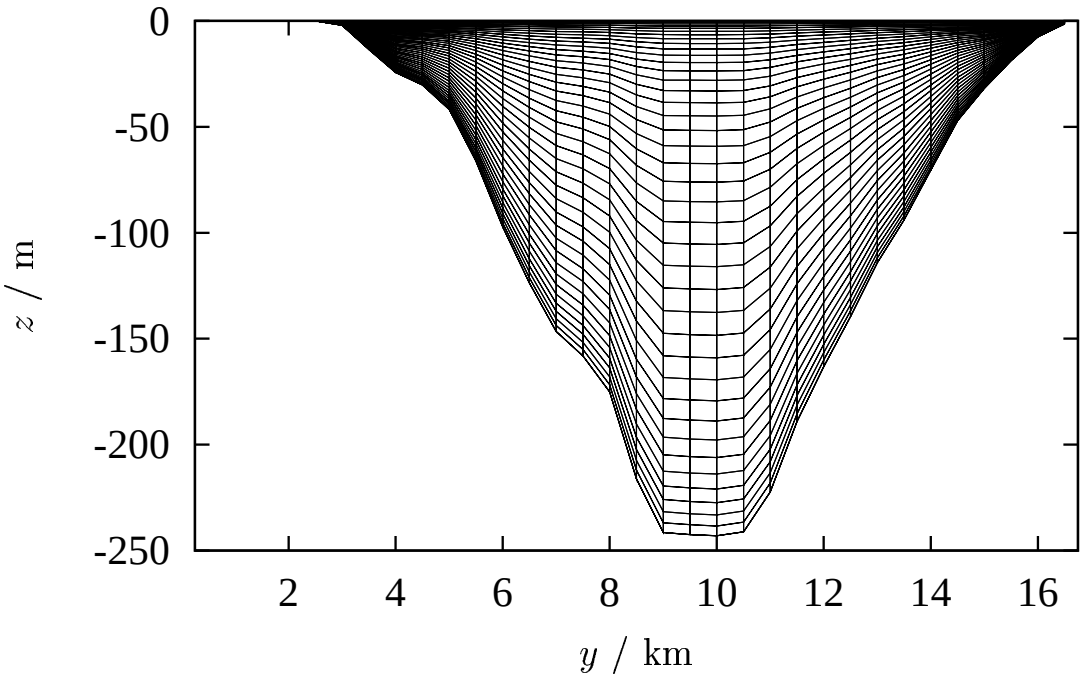

Figure 6.15: Distribution of grid boxes along a cross-section at $x = 38.75$ km.

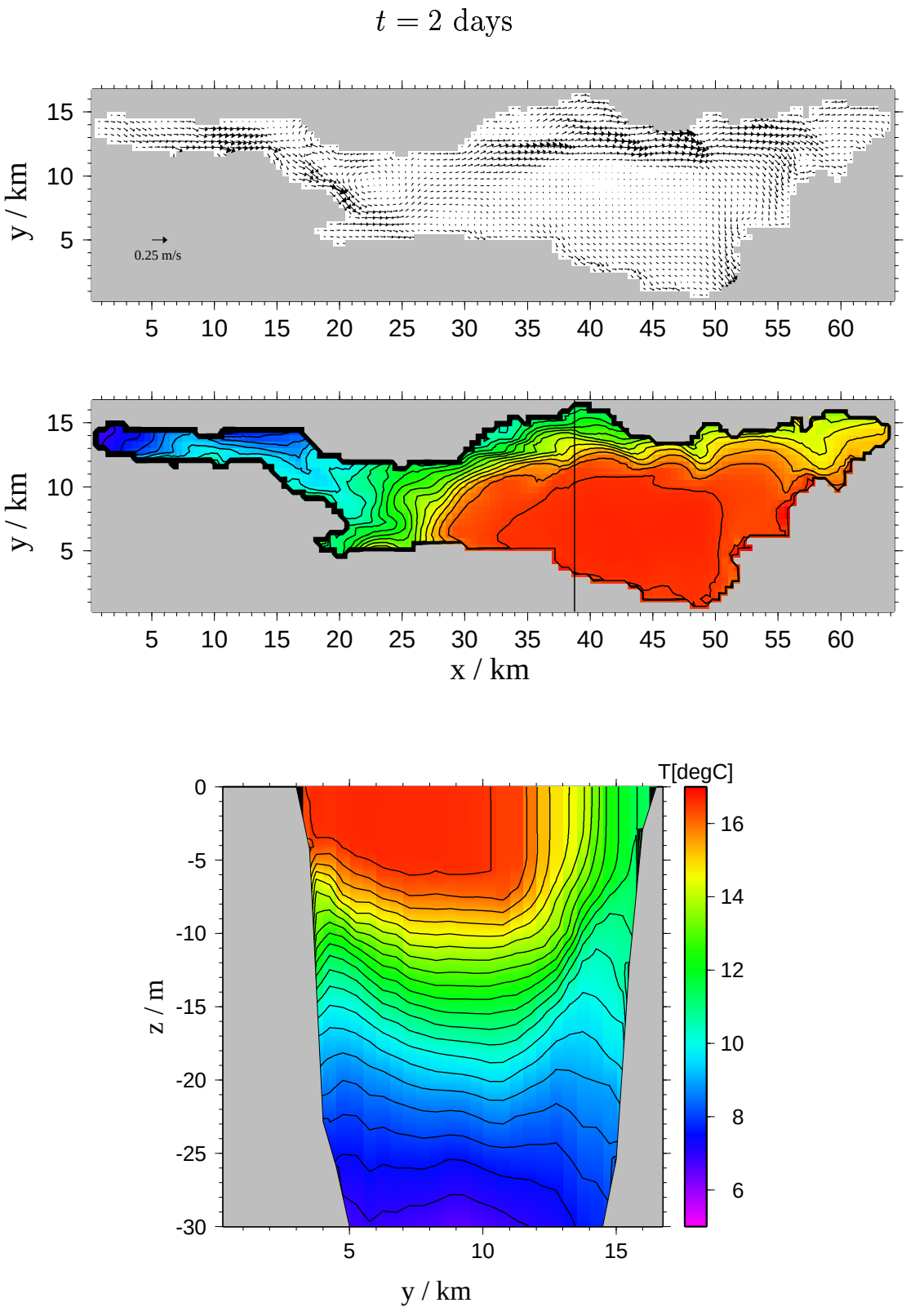

Figure 6.16: Lake Constance simulation: Sea surface temperature, surface velocity and temperature distribution in the upper 30 m along a section at $x = 38.75$ km two days after the initialisation of the experiment.

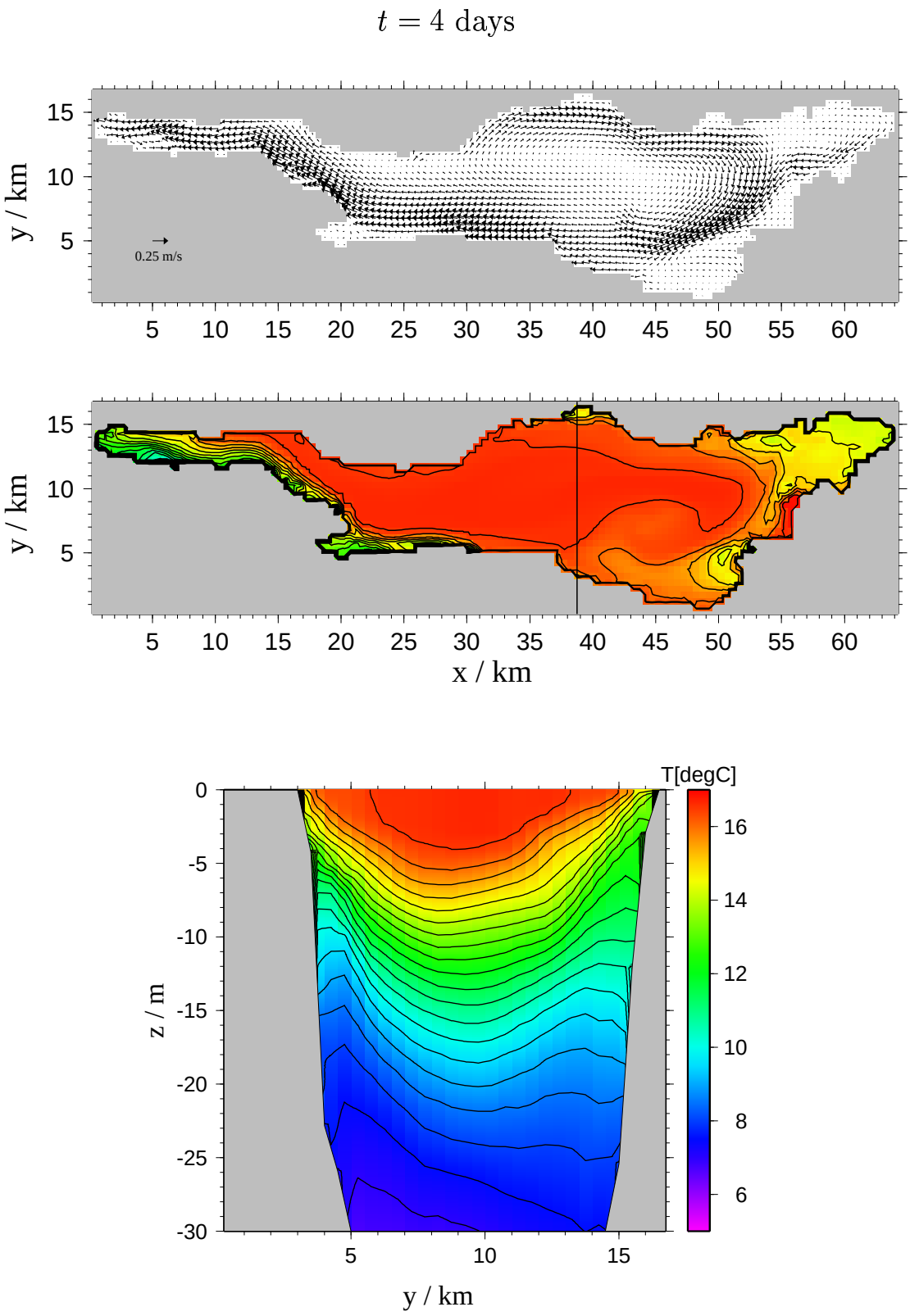

Figure 6.17: Lake Constance simulation: Sea surface temperature, surface velocity and temperature distribution in the upper 30 m along a section at $x = 38.75$ km four days after the initialisation of the experiment.

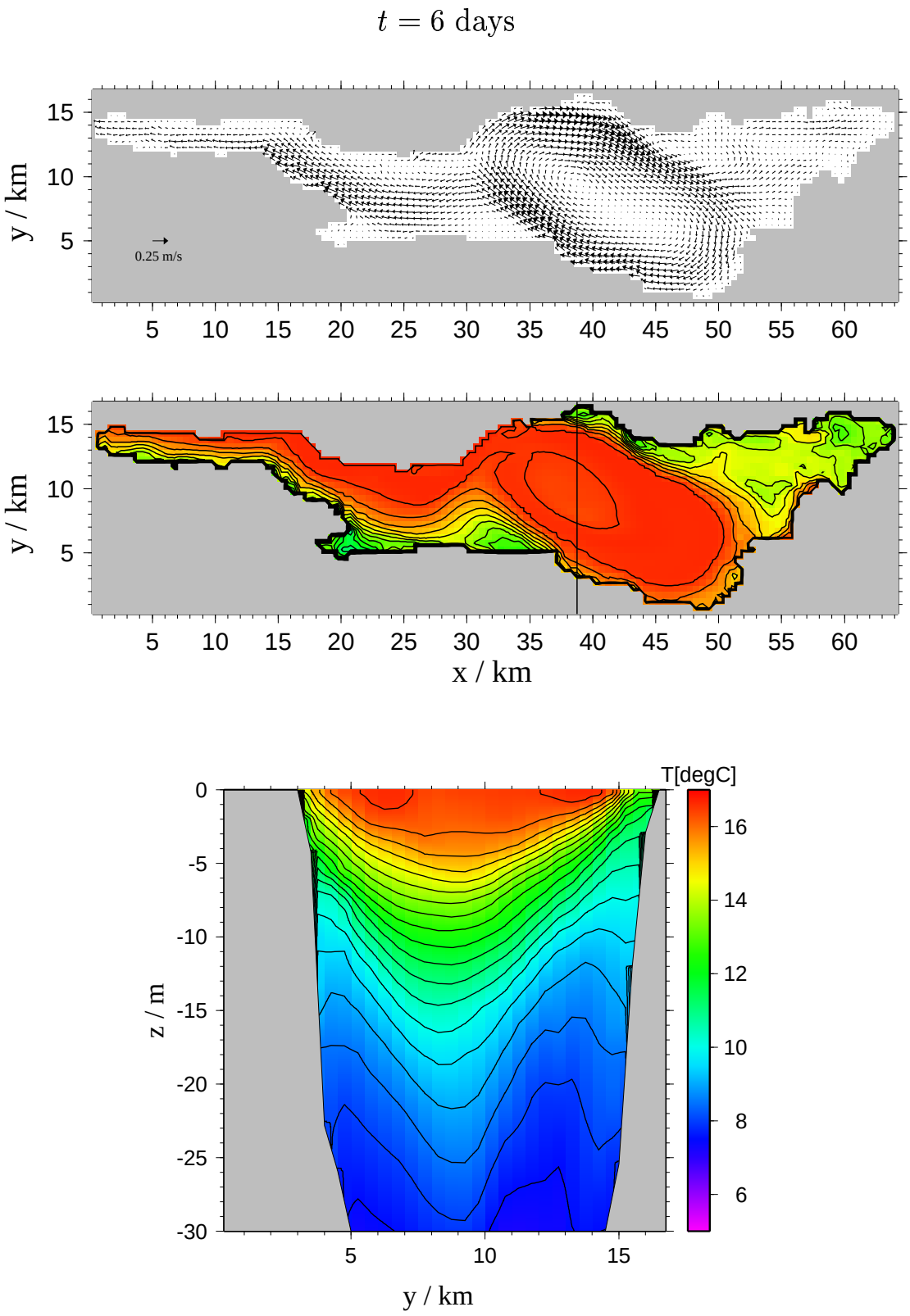

Figure 6.18: Lake Constance simulation: Sea surface temperature, surface velocity and temperature distribution in the upper 30 m along a section at $x = 38.75$ km six days after the initialisation of the experiment.

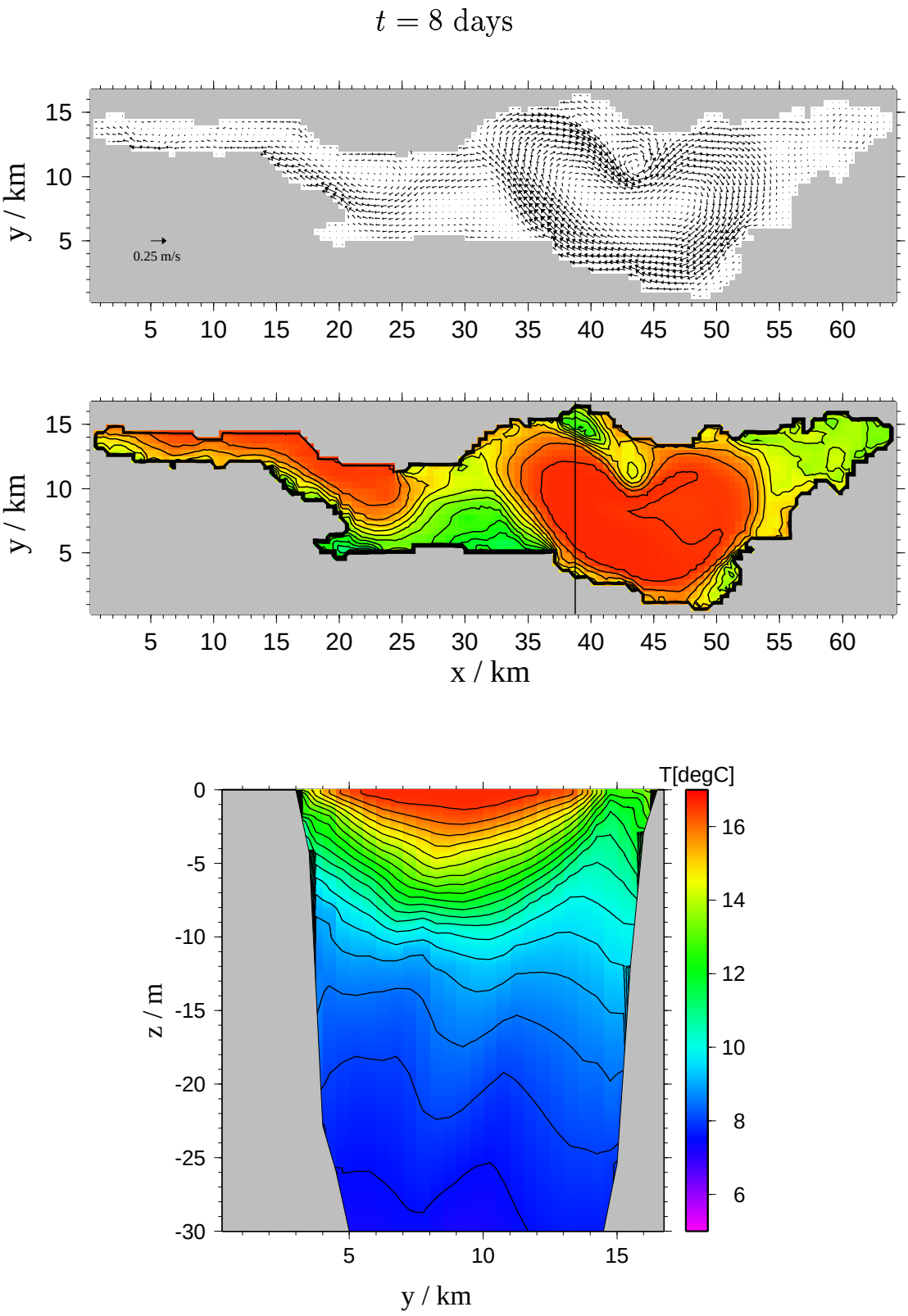

Figure 6.19: Lake Constance simulation: Sea surface temperature, surface velocity and temperature distribution in the upper 30 m along a section at $x = 38.75$ km eight days after the initialisation of the experiment.

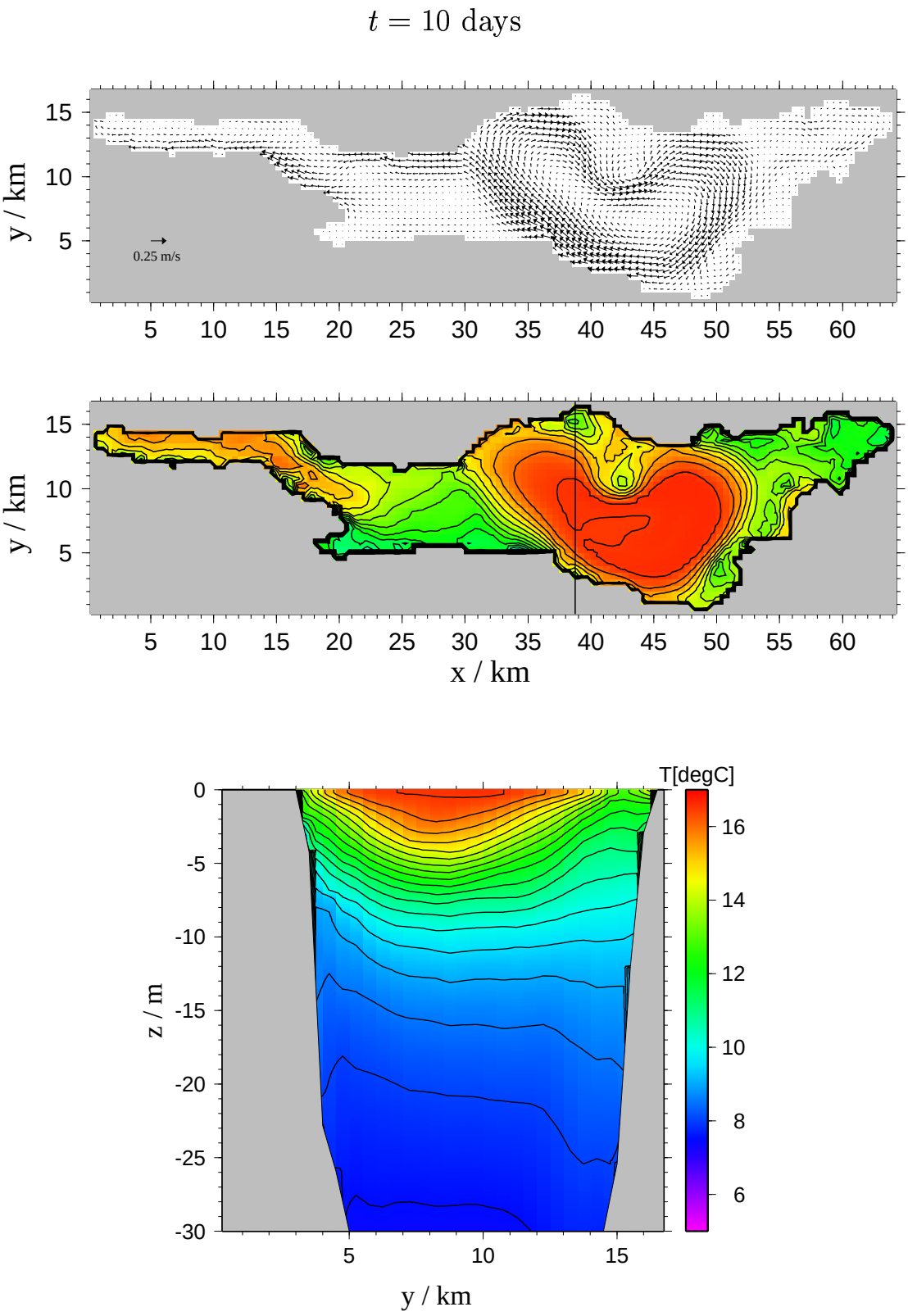

Figure 6.20: Lake Constance simulation: Sea surface temperature, surface velocity and temperature distribution in the upper 30 m along a section at $x = 38.75$ km ten days after the initialisation of the experiment.

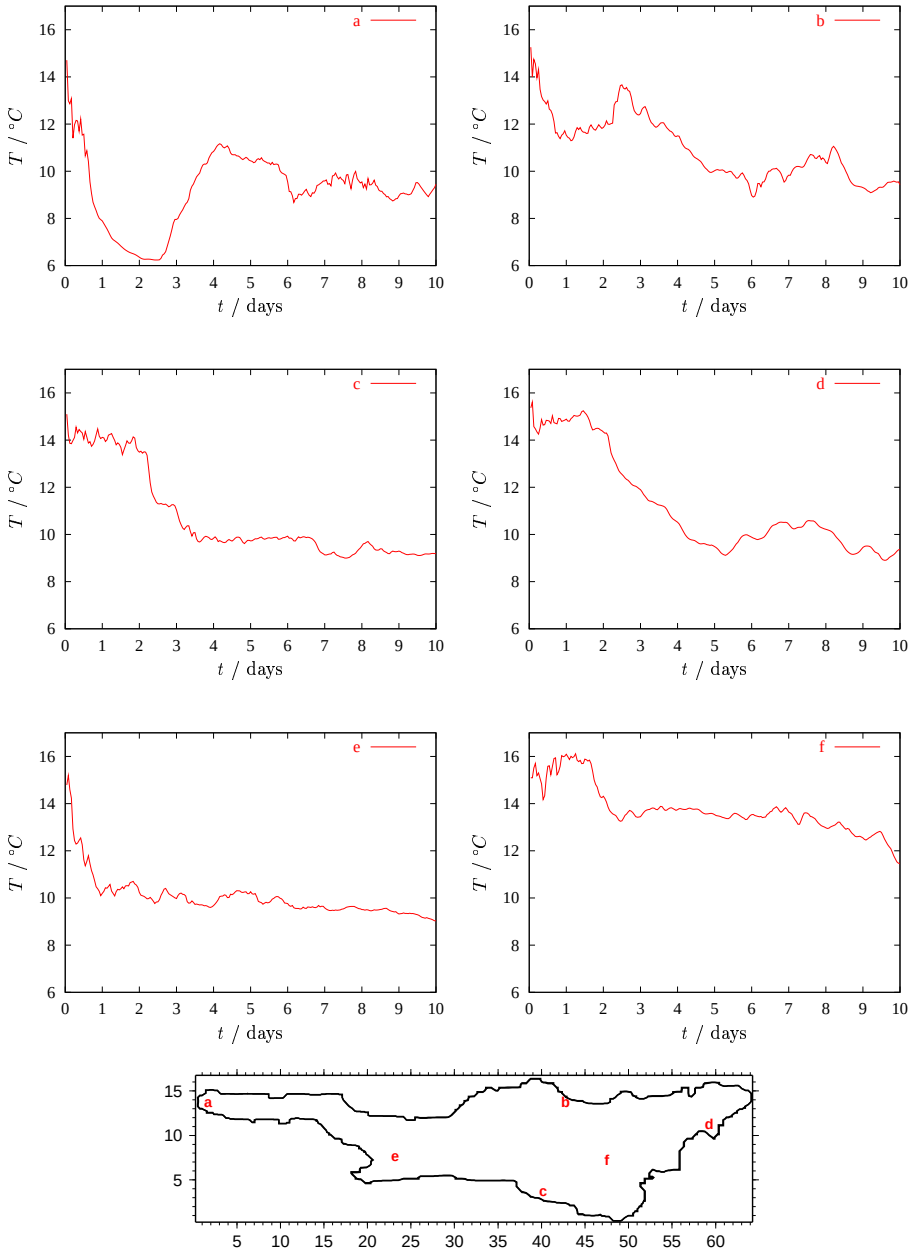

Figure 6.21: Time series of temperature at about 10 m depth for six locations in Lake Constance.

6.3 North Sea

In order to assess the performance of GETM for realistically simulating flows and transport on scales larger than the estuarine scale, an annual simulation of the North Sea circulation for the year 1997 has been carried out. This simulation is based on a relative coarse Cartesian grid with a resolution of 6 nm $\times$ 6 nm (see figure 6.22). The bathymetric values have been extracted from the 1 nm $\times$ 1 nm DYNOCS bathymetry, see *Weiergang and Jønsson* [1996]. In order not to have an open boundary towards the East, the whole Baltic Sea is included into the domain and calculated fully prognostically. The tidal forcing at the southern boundary towards the English Channel and at the northern boundary towards the Norwegian Sea has been extracted from the TOPEX-POSEIDON data set. For this, 13 partial tides have been considered. The initial values and the lateral boundary conditions for temperature and salinity have been extracted from the climatology of *Janssen et al.* [1999]. Meteorological parameters (six-hourly values on a $1^\circ \times 1^\circ$ grid for wind speed at 10 m, air pressure, relative humidity, air temperature and cloud cover at 2 m from the ECMWF re-analysis) have been used to calculate wind stress, and latent and sensitive surface heat fluxes by means of the bulk formulae by *Kondo* [1975] for which the simulated sea surface temperature was taken into account. The long-wave back radiation has been calculated based on a formula by *Clark et al.* [1974]. The solar radiation at the sea surface has been estimated from the cloud cover by means of the *Payne* [1972] albedo correction. From these values the radiation in the water column has been calculated by means of a formula by *Paulson and Simpson* [1977] who estimated the parameters for the *Jerlov* [1968] type I (clear water), see also equation (2.33). The freshwater run-off from 82 rivers into the Baltic Sea and the North Sea has been kindly provided by the Swedish Meteorological and Hydrological Institute. The formation of sea ice has been parameterised in a simple way by constraining the sea surface temperature to the freezing point (see e.g. *Kantha and Clayson* [2000a], p. 785). As turbulence model, the standard k-ε two-equation model with the turbulent Prandtl number parameterisation as suggested by *Schumann and Gerz* [1995] has been applied. Horizontal diffusion of momentum, temperature and salinity has been set to zero.

The external (barotropic) time step was $\Delta t_m = 45$ s, and the internal (baroclinic) time step $\Delta t = 1800$ s, i.e. a split factor of $M = 40$ was used. In the vertical, $N = 25$ layers have been used. As vertical coordinate transformation, the so-called upper γ-coordinate with $d_u = 2$ and $d_l = 1$ and a critical water depth of $D_\gamma = 40$ m has been used, see also section 3.1.1 and equation (3.8) therein. This results in a maximum surface layer thickness of $h = 1.67$ m, even in the Norwegian trench region where the water depth exceeds 700 m. Only at water depths below 40 m,

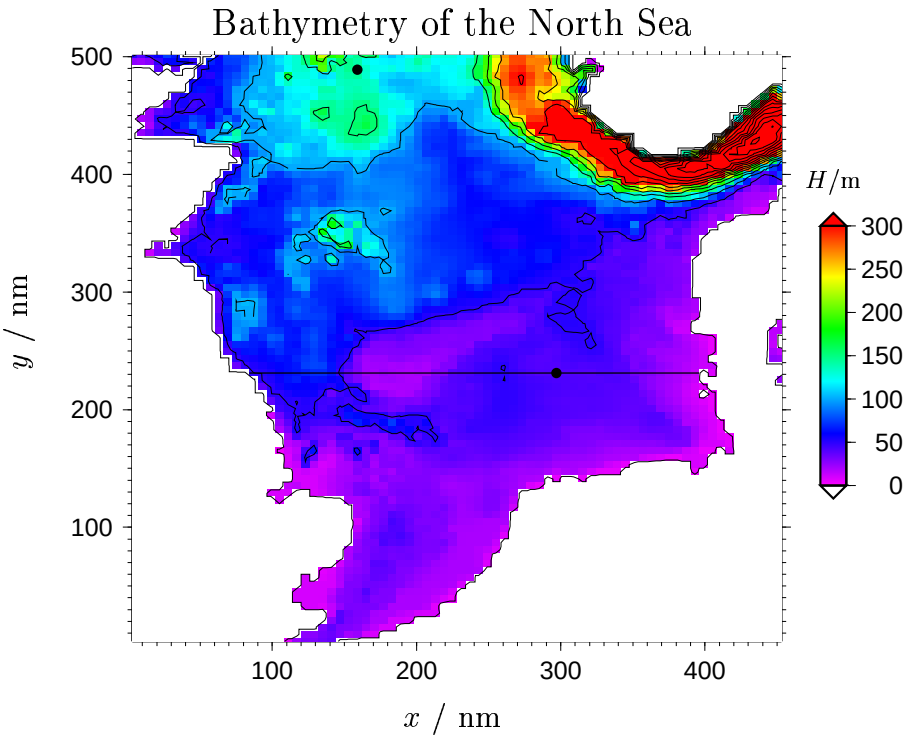

Figure 6.22: Bathymetry of the North Sea with a resolution of 6 nm × 6 nm as extracted from the DYNOCS data set. Shown are also the west-east Doggerbank section and station 1 in the Northern North Sea and station 2 in the Southern North Sea.

where (non-equidistant) σ coordinates are used, the surface layer thickness may be significantly less. For temperature and salinity the TVD directional splitting scheme with Superbee limiter (see equation (4.63)) has been applied, for the momentum advection the multi-dimensional first-order upstream scheme was used.

The model has been initialised at 0:00 h on December 1, 1996, with the December climatological values for temperature and salinity and zero velocities and surface elevation. For the first two weeks, the model has been run without tidal forcing in diagnostic mode with fixed temperature and salinity. After 0:00 h on December 16, 1996, the model has been integrated in fully prognostic mode.

Some results of this simulation are shown in figures (6.23) - (6.32) as contour plots of sea surface temperature and salinity and temperature and salinity across a section as indicated in figure 6.22 for every second month. Furthermore, temperature and salinity results are shown for two stations, one in the Northern North Sea and the

other in the Southern North Sea, as marked in figure 6.22 as well.
In the following, these results of a first application of GETM to the dynamics of the North Sea will be briefly discussed.
The surface salinity contour plots do all clearly show the regions of freshwater influence (ROFI) along the Dutch, German and Danish coast. Also some freshwater outflow out of the Skagerak along the Norwegian coast is visible. During the summer months these regions of low surface salinity are strongly enhanced (see figure 6.26) due to increased stability of the water column supported by thermal stratification and lower wind speeds. This haline stratification can be clearly seen in the cross section plots for salinity on the eastern shore. In autumn this stratification breaks down (see figures 6.27 and 6.28) such that the regions of low salinity are more confined to the coast. The results for the sea surface temperature show a much stronger annual variability in shallow coastal areas than in the deeper water, since in the former areas, the surface heat fluxes are distributed over much a shallower water column than in the latter case. The temperature sections across the Doggerbank area show that the water column is thermally well mixed until beginning of April (see figures 6.23 and 6.24), but during summer the deeper areas west and east of the shallow Doggerbank are strongly stratified. The tidal currents prohibit the evolution of stratification over the Doggerbank.
The results for the two stations in the Northern North Sea and the Southern North Sea show the typical evolution of a stratified two-layer system during summer. In contrast to that the haline stratification remains weak.
In the future, a careful comparison of these results to observations has to be carried out. There are many factors outside and inside a numerical model which can influence the results, such as the quality and resolution of the meteorological data, the choice of the bulk formulae and water turbidity parameters, the choice of the turbulence model. And also numerical aspects have a strong impact on the results such as spatial resolution in the horizontal and vertical, choice of the advection schemes, stability of the coupling between turbulence module and mean flow module, and many other more. For the first, it can be concluded that GETM provides reasonable and numerically robust results for simulating the dynamics of the North Sea.

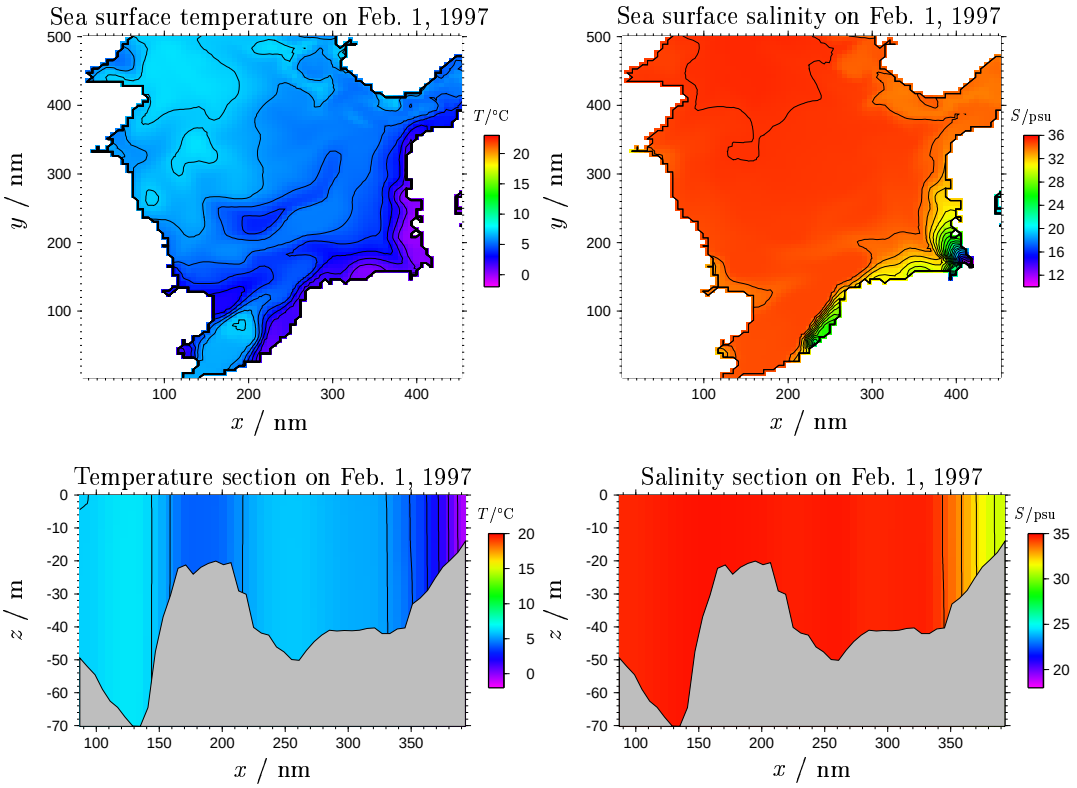

Figure 6.23: North Sea simulation: Sea surface temperature and salinity (upper panels) and temperature and salinity across the West-East Doggerbank section (lower panels) on Feb. 1, 1997.

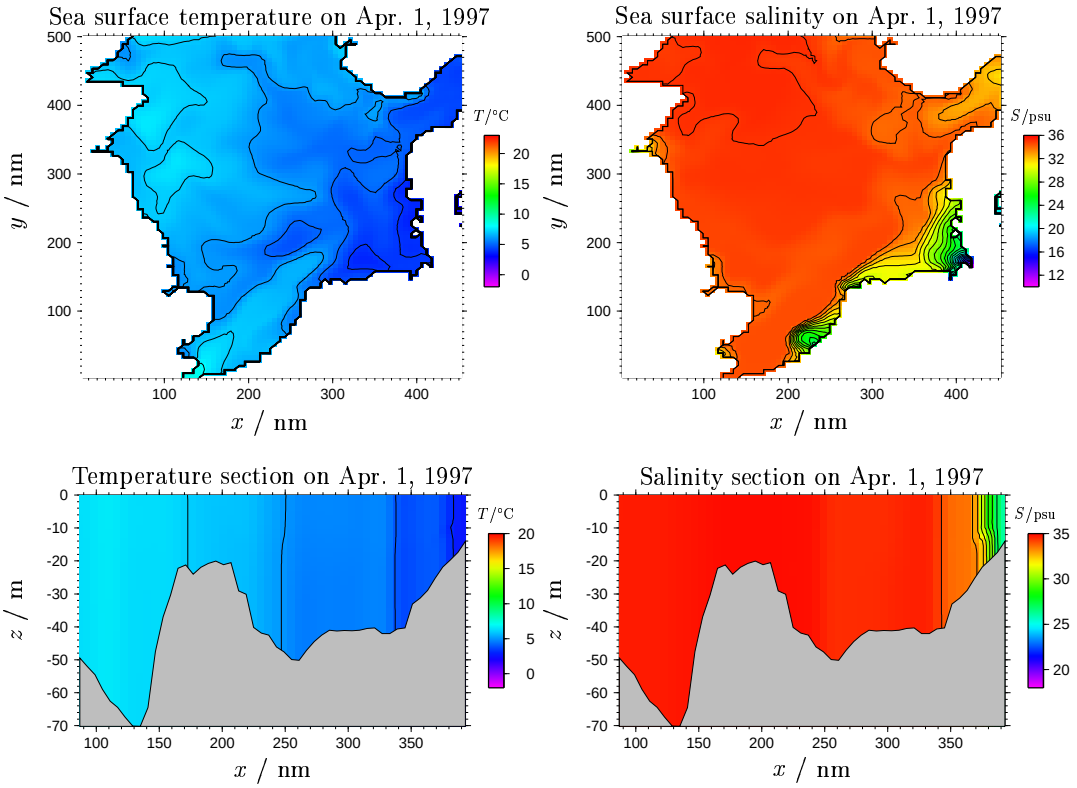

Figure 6.24: North Sea simulation: Sea surface temperature and salinity (upper panels) and temperature and salinity across the West-East Doggerbank section (lower panels) on Apr. 1, 1997.

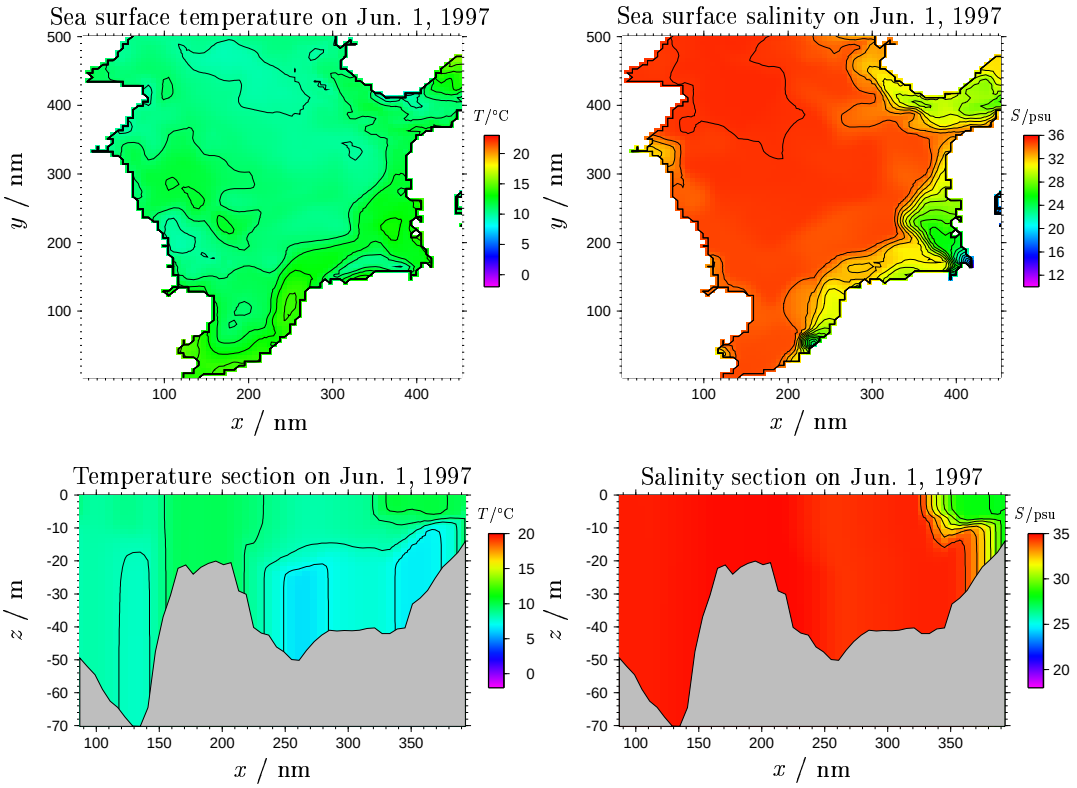

Figure 6.25: North Sea simulation: Sea surface temperature and salinity (upper panels) and temperature and salinity across the West-East Doggerbank section (lower panels) on Jun. 1, 1997.

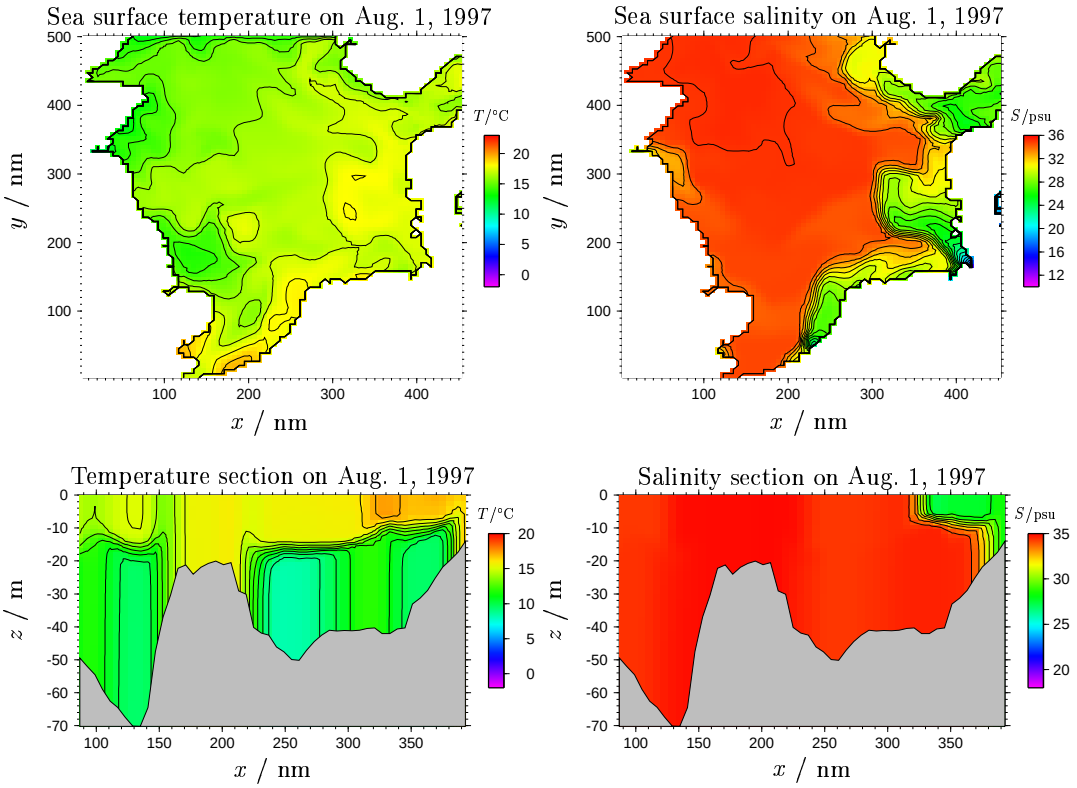

Figure 6.26: North Sea simulation: Sea surface temperature and salinity (upper panels) and temperature and salinity across the West-East Doggerbank section (lower panels) on Aug. 1, 1997.

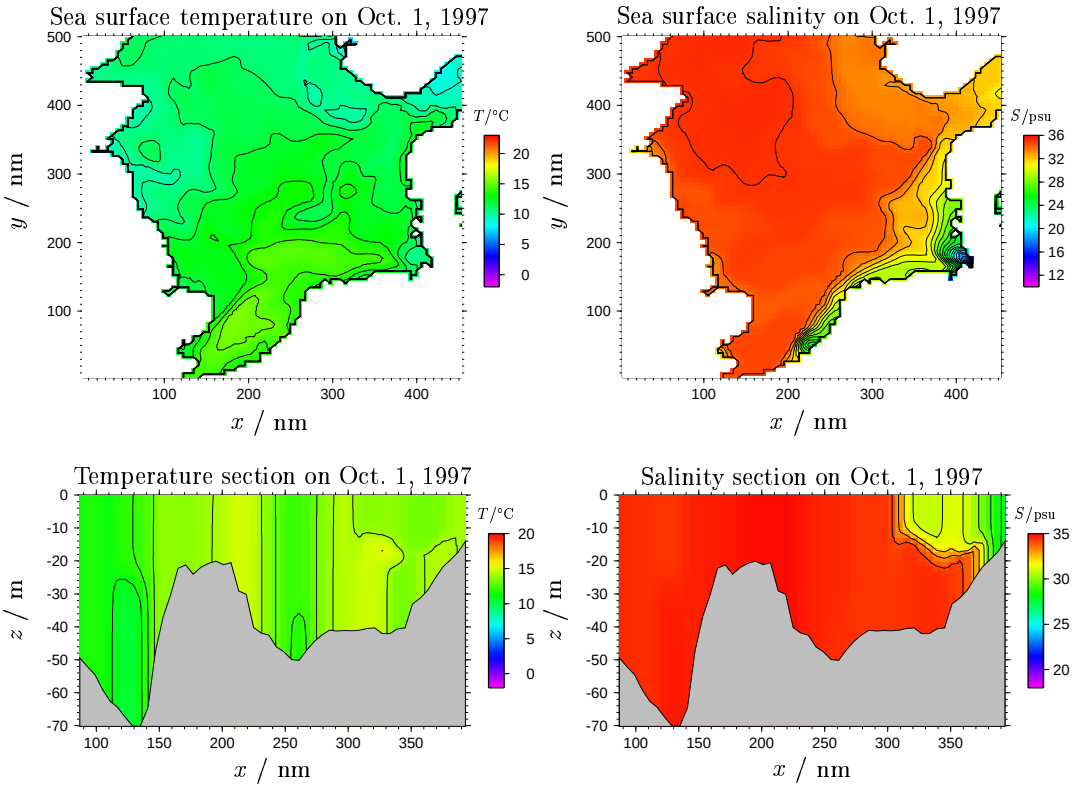

Figure 6.27: North Sea simulation: Sea surface temperature and salinity (upper panels) and temperature and salinity across the West-East Doggerbank section (lower panels) on Oct. 1, 1997.

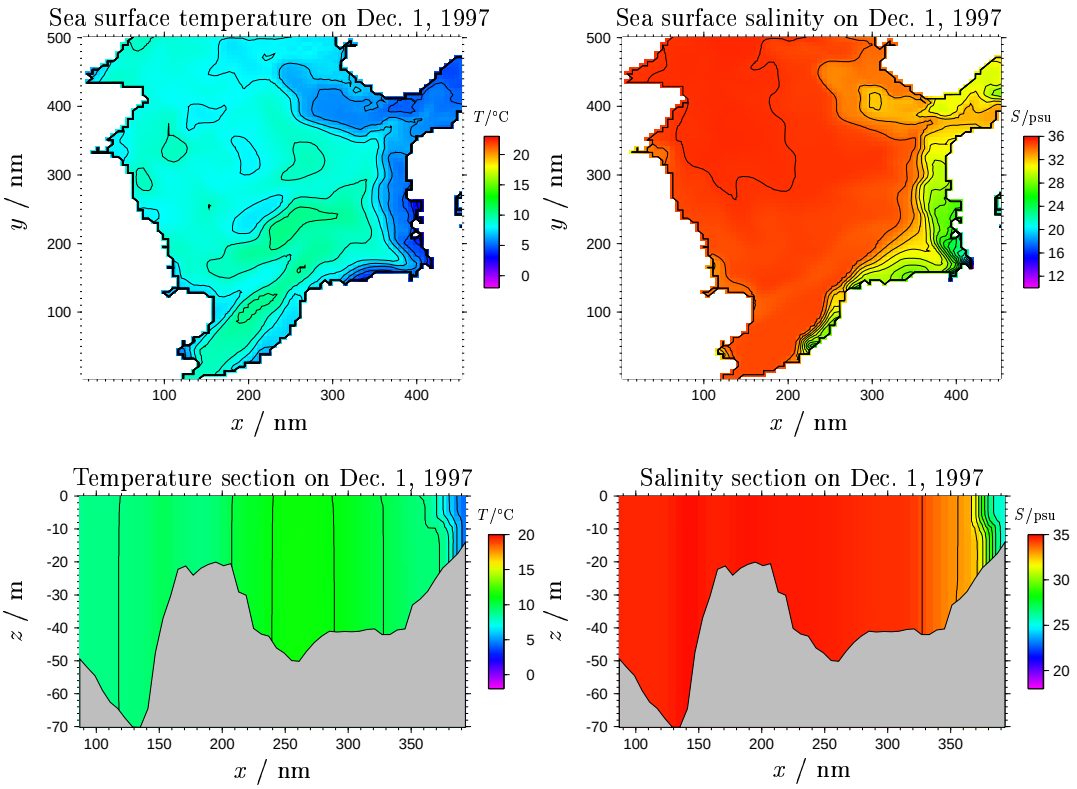

Figure 6.28: North Sea simulation: Sea surface temperature and salinity (upper panels) and temperature and salinity across the West-East Doggerbank section (lower panels) on Dec. 1, 1997.

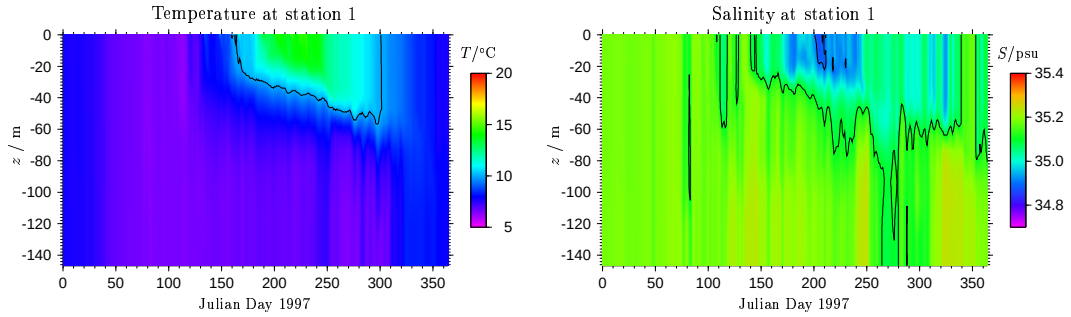

Figure 6.29: Simulated temperature and salinity at station 1 (Northern North Sea).

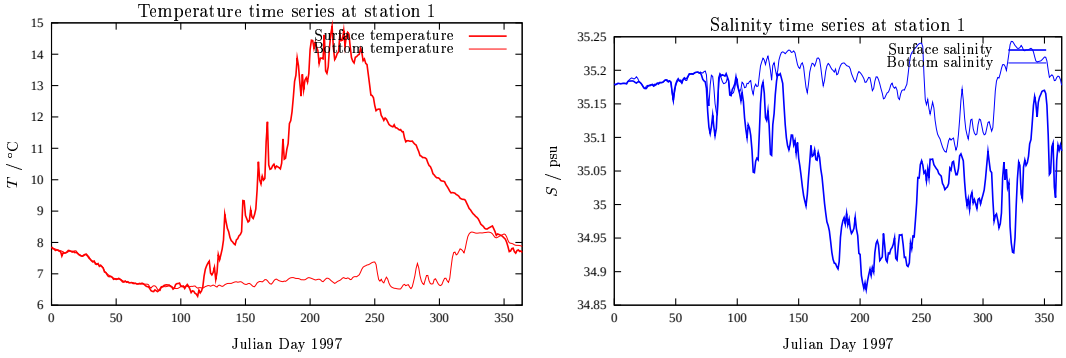

Figure 6.30: Simulated temperature and salinity time series at the surface (bold lines) and at the bed (thin lines) at station 1 (Northern North Sea).

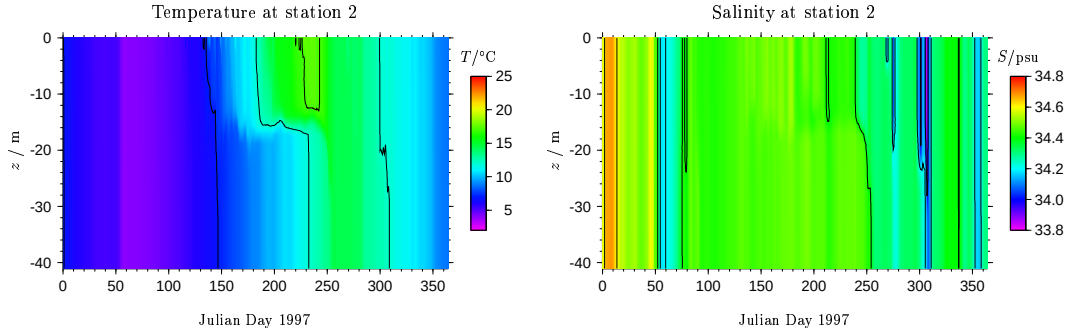

Figure 6.31: Simulated temperature and salinity at station 2 (Southern North Sea).

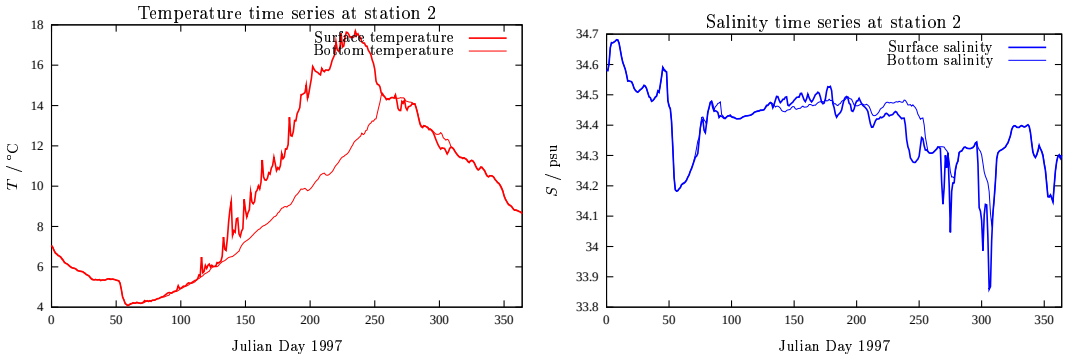

Figure 6.32: Simulated temperature and salinity time series at the surface (bold lines) and at the bed (thin lines) at station 2 (Southern North Sea).

Chapter 7

Appendix

7.1 List of symbols

Here, most of the symbols used in the text are listed, first the Greek and then the Latin characters in alphabetical order. The physical unit is indicated and also the page or equation number of the first occurrence in the text. Order not to flood the text with superscripts or subscripts, some duplications were accepted. Some omissions have been allowed for as well, e.g. the layer averaged velocity u_k is listed, but not the discrete value of it, which would be $u_{i,j,k}$.

Parameter	**Physical meaning**	**Unit/Value**	**Reference**
α	drying parameter	–	(2.1)
α_γ	weighting parameter	–	(3.8)
$\alpha_{i+1/2}$	numerical coefficient	–	(4.58)
β_k	general vertical coordinate	–	(3.5)
$\beta_{i+1/2}$	numerical coefficient	–	(4.58)
Δt	time step	s	(4.1)
Δt_m	micro time step	s	p. 35
Δx	increment in x-direction	m	(4.1)
$\Delta x^c_{i,j}$	Δx on T-points	m	(4.19)
$\Delta x^u_{i,j}$	Δx on U-points	m	(4.19)
$\Delta x^v_{i,j}$	Δx on V-points	m	(4.19)
$\Delta x^+_{i,j}$	Δx on X-points	m	(4.19)

Parameter	Physical meaning	Unit/Value	Reference
Δy	increment in y-direction	m	(4.1)
$\Delta y^c_{i,j}$	Δy on T-points	m	(4.19)
$\Delta y^u_{i,j}$	Δy on U-points	m	(4.19)
$\Delta y^v_{i,j}$	Δy on V-points	m	(4.19)
$\Delta y^+_{i,j}$	Δy on X-points	m	(4.19)
ε	dissipation of TKE	$\mathrm{W\,kg^{-1}}$	(2.38)
ζ	sea surface elevation	m	(2.1)
η_1,η_2	attenuation coefficients	$\mathrm{m^{-1}}$	(2.33)
κ	von Kármán constant	0.4	(2.26)
λ	latitude	–	p. 32
ν	kinematic viscosity	$1.3 \cdot 10^{-6}$ $\mathrm{m^2 s^{-1}}$	(2.1)
ν_t	eddy viscosity for momentum	$\mathrm{m^2 s^{-1}}$	(2.1)
ν'_t	eddy diffusivity for tracers	$\mathrm{m^2 s^{-1}}$	(2.27)
ξ_x	local coordinate in physical space	m	(3.23)
ξ_y	local coordinate in physical space	m	(3.23)
ρ	potential density	$\mathrm{kg\,m^{-3}}$	(2.4)
ρ_0	reference density	$\mathrm{kg\,m^{-3}}$	(2.4)
σ	vertical coordinate	–	p. 24
σ_ε	turb. Schmidt no. for ε	–	(2.39)
σ_k	1. turb. Schmidt no. for k	–	(2.38)
	2. σ-coordinate for layer k	–	(3.3)
τ	turbulent time scale	s	p. 23
τ_b	absolute value of bottom stress	$\mathrm{N\,m^{-2}}$	p. 44
τ^x_b	bottom stress in x-direction	$\mathrm{N\,m^{-2}}$	(2.14)
τ^y_b	bottom stress in y-direction	$\mathrm{N\,m^{-2}}$	(2.15)
τ^x_k	shear stress in x-direction at $z = z_k$	$\mathrm{N\,m^{-2}}$	(3.17)
τ^y_k	shear stress in y-direction at $z = z_k$	$\mathrm{N\,m^{-2}}$	(3.18)
τ^x_s	surface stress in x-direction	$\mathrm{N\,m^{-2}}$	(2.9)
τ^y_s	surface stress in y-direction	$\mathrm{N\,m^{-2}}$	(2.9)
ϕ	longitude	–	(3.25)
$\Phi^+_{i+1/2}$	flux limiter	–	(4.57)
$\Phi^-_{i+1/2}$	flux limiter	–	(4.57)
Ψ	general tracer	variable	(4.52)
Ψ^n_i	discrete value of general tracer	variable	(4.54)
ω	angular velocity	$\mathrm{s^{-1}}$	(4.73)

Parameter	Physical meaning	Unit/Value	Reference
a	attenuation parameter	–	(2.33)
a^u	land mask for U-point	–	p. 41
a^v	land mask for V-point	–	p. 41
a^z	land mask for T-point	–	p. 41
A_h^M	horizontal viscosity	$\mathrm{m^2\,s^{-1}}$	(2.1)
A_k^M	layer averaged horizontal viscosity	$\mathrm{m^2\,s^{-1}}$	(3.15)
A_h^T	horizontal diffusivity	$\mathrm{m^2\,s^{-1}}$	(2.27)
A_k^T	layer averaged horizontal diffusivity	$\mathrm{m^2\,s^{-1}}$	(3.22)
b	buoyancy	$\mathrm{m\,s^{-2}}$	(2.1)
b_k	layer averaged buoyancy	$\mathrm{m\,s^{-2}}$	(3.12)
B	buoyancy production of TKE	$\mathrm{m^2 s^{-3}}$	(2.38)
c	Courant number	–	p. 55
$c_{i+1/2}$	discrete Courant number	–	(4.57)
$c_{1\varepsilon}, \ldots, c_{3\varepsilon}$	emp. coefficients for ε-equation	–	(2.39)
c_μ	stability function for momentum	–	(2.44)
c_μ^0	neutral stability function	–	p. 23
c_μ'	stability function for tracers	–	(2.44)
c_L	parameter for macro length scale	–	(2.43)
c_p'	specific heat capacity of water	$3980\ \mathrm{J\,kg^{-1}K^{-1}}$	(2.31)
c^i	general tracer quantity	variable	(2.27)
c_k^i	layer averaged tracer concentration	variable	(3.12)
$\tilde{c}_k^i$	advective tracer concentration	variable	(3.22)
d_l	lower grid zooming factor	–	(3.5)
d_u	upper grid zooming factor	–	(3.5)
D	water depth	m	(2.5)
D_γ	critical depth for γ-coordinates	m	(3.8)
D_{min}	minimum water depth	m	(2.5)
D_{crit}	critical water depth	m	(2.5)
$E_1, \ldots, E_3$	emp. parameters for kL equation	–	(2.42)
f	Coriolis parameter	$\mathrm{s^{-1}}$	(2.1)
$F_{i+1/2}^n$	flux of Ψ_i^n	variable	(4.54)
F_b	general bottom boundary flux	variable	(4.9)
F_s	general surface boundary flux	variable	(4.8)
F_b^i	bottom boundary flux of c^i	variable	(2.30)
F_s^i	surface boundary flux of c^i	variable	(2.29)

Parameter	Physical meaning	Unit/Value	Reference
g	gravitational acceleration	9.81 $\mathrm{m\,s^{-2}}$	(2.1)
G	set of boundary points	–	p. 15
G^c	set of closed boundary points	–	p. 15
G^o	set of open boundary points	–	p. 15
h_0^b	height of bottom roughness elements	m	(4.26)
h_k	layer thickness	m	(3.2)
H	mean water depth	m	p. 13
i	index in $\mathcal{X}$-direction	–	p. 39
$i_{\max}$	number of increments in $\mathcal{X}$-direction	–	(4.18)
I	solar radiation in water column	$\mathrm{W\,m^{-2}}$	(2.31)
I_0	solar radiation at surface	$\mathrm{W\,m^{-2}}$	(2.33)
j	index in $\mathcal{Y}$-direction	–	p. 39
$j_{\max}$	number of increments in $\mathcal{Y}$-direction	–	(4.18)
k	1. turbulent kinetic energy (TKE)	$\mathrm{J\,kg^{-1}}$	(2.38)
	2. index in vertical direction	–	(3.1)
$k_{\max}$	number of increments in vertical direction	–	(4.18)
L	integral-scale macro length	m	(2.41)
L_2	error measure	variable	(4.67)
L_x	length of domain in x-direction	m	p. 62
L_y	length of domain in y-direction	m	p. 62
L_z	prognostic length scale for kL equation	m	(2.42)
m	1. exponent of ε in generic model	-	p. 23
	2. metric coefficient	-	(3.24)
n	1. exponent of k in generic model	-	p. 23
	2. metric coefficient	-	(3.24)
M	micro time steps per macro time step	–	4.3
N	1. Brunt-Väisälä frequency	$\mathrm{s^{-1}}$	(4.105)
N	2. number of horizontal grid boxes	–	4.64
$N = k_{\max}$	3. number of vertical layers	–	3.1
N_c	number of tracers	–	2.27
p_0	hydrostatic reference pressure	$\mathrm{N\,m^{-2}}$	2.28
p_k	eastward layer-integrated transport	$\mathrm{m^2 s^{-1}}$	3.10
P	shear production of TKE	$\mathrm{m^2 s^{-3}}$	(2.38)
q_k	northward layer-integrated transport	$\mathrm{m^2 s^{-1}}$	3.10
Q^i	source term for c^i	variable	2.27

Parameter	Physical meaning	Unit/Value	Reference
Q	general source term	variable	4.6
Q_k^i	layer averaged source term for c_k^i	variable	3.22
Q_b	long-wave back radiation at surface	$\mathrm{W\,m^{-2}}$	(2.34)
Q_E	evaporation	$\mathrm{kg\,m^{-2}s^{-1}}$	(2.37)
Q_l	latent surface heat flux	$\mathrm{W\,m^{-2}}$	(2.34)
Q_P	precipitation	$\mathrm{kg\,m^{-2}s^{-1}}$	(2.37)
Q_s	sensitive surface heat flux	$\mathrm{W\,m^{-2}}$	(2.34)
Q_{surf}	surface heat flux	$\mathrm{W\,m^{-2}}$	(2.36)
r_E	Earth's radius	6371 km	3.25
$r^+_{i+1/2}$	slope ratio	–	4.58
$r^-_{i+1/2}$	slope ratio	–	4.58
R	vertically integrated drag coefficient	–	2.16
S	salinity	psu	(2.32)
S_l	stability function for kL	–	(2.42)
S_q	stability function for k	–	(2.41)
S_s	sea surface salinity	psu	(2.35)
S_A^x	advective slow term in u-equation	$\mathrm{m^2s^{-2}}$	2.16
S_A^y	advective slow term in v-equation	$\mathrm{m^2s^{-2}}$	2.17
S_B^x	buoyant slow term in u-equation	$\mathrm{m^2s^{-2}}$	2.16
S_B^y	buoyant slow term in v-equation	$\mathrm{m^2s^{-2}}$	2.17
S_D^x	diffusive slow term in u-equation	$\mathrm{m^2s^{-2}}$	2.16
S_D^y	diffusive slow term in v-equation	$\mathrm{m^2s^{-2}}$	2.17
S_F^x	frictional slow term in u-equation	$\mathrm{m^2s^{-2}}$	2.16
S_F^y	frictional slow term in v-equation	$\mathrm{m^2s^{-2}}$	2.17
t	time	s	(2.1)
T	1. potential temperature	°C	(2.31)
	2. total run time	s	p. 62
T_f	freezing point	°C	(2.35)
T_s	sea surface temperature	°C	(2.36)
TV	total variation	variable	(4.65)
TV_0	initial total variation	variable	table 4.1
u	eastward velocity component	$\mathrm{m\,s^{-1}}$	(2.1)
$\vec{u}$	horizontal velocity vector	$\mathrm{m\,s^{-1}}$	p. 15
u_*^b	bottom friction velocity	$\mathrm{m\,s^{-1}}$	(4.26)
u_*^{bx}	x-comp. of bottom friction velocity	$\mathrm{m\,s^{-1}}$	(4.21)

Parameter	Physical meaning	Unit/Value	Reference
u_*^{by}	y-comp. of bottom friction velocity	$\mathrm{m\,s^{-1}}$	(4.22)
u_b	x-component near-bed discrete velocity	$\mathrm{m\,s^{-1}}$	(4.24)
$u_{\max}$	maximum of $u_{i.j.k}$	$\mathrm{m\,s^{-1}}$	(4.2)
$\vec{u}_n$	vector normal to $\vec{u}$	$\mathrm{m\,s^{-1}}$	p. 15
u_k	eastward layer-averaged velocity	$\mathrm{m\,s^{-1}}$	(3.11)
$\tilde{u}_k$	eastward advective velocity for u_k	$\mathrm{m\,s^{-1}}$	3.15
U	vertical integral of u	$\mathrm{m^2 s^{-1}}$	(2.12)
v	northward velocity component	$\mathrm{m\,s^{-1}}$	(2.1)
v_b	y-component near-bed discrete velocity	$\mathrm{m\,s^{-1}}$	(4.25)
v_k	northward layer-averaged velocity	$\mathrm{m\,s^{-1}}$	(3.11)
$\tilde{v}_k$	northward advective velocity for v_k	$\mathrm{m\,s^{-1}}$	3.16
$v_{\max}$	maximum of $v_{i.j.k}$	$\mathrm{m\,s^{-1}}$	(4.2)
V	vertical integral of v	$\mathrm{m^2 s^{-1}}$	(2.12)
w	upward velocity component	$\mathrm{m\,s^{-1}}$	(2.1)
w_k	vertical velocity at $z = z_{k-1/2}$	$\mathrm{m\,s^{-1}}$	(3.21)
$\bar{w}_k$	grid-related vertical velocity	$\mathrm{m\,s^{-1}}$	(3.13)
w_s^i	migration velocity of c^i	$\mathrm{m\,s^{-1}}$	(2.27)
x	eastward coordinate	m	(2.1)
x_0	eastward coordinate of centre point	m	(4.73)
$x_{i,j}$	x-coordinate of X-point	m	fig. 4.3
X	general physical quantity	variable	(4.6)
$\mathcal{X}$	non-dimensional local coordinate	-	(3.23)
y	northward coordinate	m	(2.1)
y_0	northward coordinate of centre point	m	(4.73)
$y_{i,j}$	y-coordinate of Y-point	m	fig. 4.3
$\mathcal{Y}$	non-dimensional local coordinate	-	(3.23)
z	upward coordinate	m	(2.1)
z'	distance from surface or bottom	m	(4.23)
z_0^b	bottom roughness length	m	(2.26)
z_k	vertical coordinate of layer interface	m	(3.1)

Bibliography

Arakawa, A., and V. R. Lamb, Computational design of the basic dynamical processes of the UCLA General Circulation Model, *Meth. Comput. Phys.*, pp. 173–263, 1977.

Backhaus, J. O., A three-dimensional model for the simulation of shelf sea dynamics, *Dt. Hydrogr. Z.*, *38*, 165–187, 1985.

Baumert, H., and G. Radach, Hysteresis of turbulent kinetic energy in nonrotational tidal flows: A model study, *J. Geophys. Res.*, *97*, 3669–3677, 1992.

Baumert, H., G. Bruckner, E. Kleine, R. Kluge, and W. Müller, Abschlußbericht zur G_4-verteidigung, *Tech. rep.*, Karl-Weierstraß-Institut für Mathematik, Akademie der Wissenschaften der DDR, Berlin, 1989.

Beckers, J.-M., La méditerranée occidentale: de la modélisation mathématique à la simulation numérique, Ph.D. thesis, Université de Liège, Belgium, 1995, collection des publications de la Faculté des Sciences Appliquées No. 136.

Beckers, J.-M., and E. Deleersnijder, Stability of a FBTCS scheme applied to the propagation of shallow-water inertia-gravity waves on various space grids, *J. Computat. Phys.*, *108*, 95–104, 1993.

Beckers, J.-M., H. Burchard, J.-M. Campin, E. Deleersnijder, and P.-P. Mathieu, Another reason why simple discretizations of rotated diffusion operators cause problems in ocean models. Comments on the paper *isoneutral diffusion in a z-coordinate ocean model* by Griffies et al., *J. Phys. Oceanogr.*, *28*, 1552–1559, 1998.

Beckers, J.-M., H. Burchard, E. Deleersnijder, and P.-P. Mathieu, On the numerical discretisation of rotated diffusion operators in ocean models, *Monthly Weather Review*, *128*, 2711–2733, 2000.

Blumberg, A. F., and G. L. Mellor, A description of a coastal ocean circulation model, in *Three dimensional ocean models*, edited by N. S. Heaps, pp. 1–16, American Geophysical Union, Washington, D.C., 1987.

Bolding, K., H. Burchard, T. Pohlmann, and A. Stips, Turbulent mixing in the Northern North Sea: a numerical model study, *Cont. Shelf Res.*, 2000, submitted.

Bryan, K., A numerical model for the study of the world ocean, *J. Computat. Phys.*, *4*, 347–376, 1969.

Burchard, H., Turbulenzmodellierung mit Anwendungen auf thermische Deckschichten im Meer und Strömungen in Wattengebieten, Ph.D. thesis, Institut für Meereskunde, Universität Hamburg, 1995, published as: Report 95/E/30, GKSS Research Centre.

Burchard, H., The 3D hydrostatic equations in a generalized vertical coordinate system. Theory and test cases, *Tech. Rep. ICCH R22*, International Research Centre for Computational Hydrodynamics, Danish Hydraulic Institute, Hørsholm, Denmark, 1996.

Burchard, H., Presentation of a new numerical model for turbulent flow in estuaries, in *Hydroinformatics '98*, edited by V. Babovic and L. C. Larsen, pp. 41–48, Balkema, Rotterdam, 1998, Proceedings of the third International Conference on Hydroinformatics, Copenhagen, Denmark, 24-26 August 1998.

Burchard, H., Note on the q^2l equation by Mellor and Yamada [1982], *J. Phys. Oceanogr.*, *31*, 1377–1387, 2001a.

Burchard, H., Simulating the wave-enhanced layer under breaking surface waves with two-equation turbulence models, *J. Phys. Oceanogr.*, *31*, 3133–3145, 2001b.

Burchard, H., Applied turbulence modelling in marine waters, 2001c, Habilitation thesis. Institute for Oceanography, University of Hamburg.

Burchard, H., Energy-conserving discretisation of turbulent shear and buoyancy production, *Ocean Modelling*, 2001d, accepted for publication.

Burchard, H., and H. Baumert, On the performance of a mixed-layer model based on the k-ε turbulence closure, *J. Geophys. Res.*, *100*, 8523–8540, 1995.

Burchard, H., and H. Baumert, The formation of estuarine turbidity maxima due to density effects in the salt wedge. A hydrodynamic process study, *J. Phys. Oceanogr.*, *28*, 309–321, 1998.

Burchard, H., and K. Bolding, Comparative analysis of four second-moment turbulence closure models for the oceanic mixed layer, *J. Phys. Oceanogr.*, *31*, 1943–1968, 2001.

Burchard, H., and E. Deleersnijder, Stability of algebraic non-equilibrium second-order closure models, *Ocean Modelling*, *3*, 33–50, 2001.

Burchard, H., and O. Petersen, Hybridisation between σ and z coordinates for improving the internal pressure gradient calculation in marine models with steep bottom slopes, *Int. J. Numer. Meth. Fluids*, *25*, 1003–1023, 1997.

Burchard, H., and O. Petersen, Models of turbulence in the marine environment – A comparative study of two-equation turbulence models, *J. Mar. Sys.*, *21*, 29–53, 1999.

Burchard, H., K. Bolding, and M. R. Villarreal, GOTM – a general ocean turbulence model. Theory, applications and test cases, *Tech. Rep. EUR 18745 EN*, European Commission, 1999.

Burchard, H., K. Bolding, T. P. Rippeth, A. Stips, J. H. Simpson, and J. Sündermann, Microstructure of turbulence in the Northern North Sea: A comparative study of observations and model simulations, *Journal of Sea Research*, 2001, accepted for publication.

Canuto, V. M., A. Howard, Y. Cheng, and M. S. Dubovikov, Ocean turbulence I: one-point closure model. Momentum and heat vertical diffusivities, *J. Phys. Oceanogr.*, *31*, 1413–1426, 2001.

Casulli, V., and E. Cattani, Stability, accuracy and efficiency of a semi-implicit method for three-dimensional shallow water flow, *Computers Math. Appl.*, *27*, 99–112, 1994.

Casulli, V., and R. T. Cheng, Semi-implicit finite difference methods for three-dimensional shallow water flow, *Int. J. Numer. Meth. Fluids*, *15*, 629–648, 1992.

Chu, P. C., and C. Fan, Sixth-order difference scheme for sigma coordinate ocean models, *J. Phys. Oceanogr.*, *27*, 2064–2071, 1997.

Clark, N. E., L. Eber, R. M. Laurs, J. A. Renner, and J. F. T. Saur, Heat exchange between ocean and atmoshere in the Eastern North Pacific for 1961-1971, *Tech. Rep. NMFS SSRF-682*, NOAA, U.S. Dept. of Commerce, Washington, D.C., 1974.

Cox, M. D., A primitive equation, 3-dimensional model for the ocean, *Tech. Rep. 1*, Geophysical Fluid Dynamics Laboratory, University of Princeton, Princeton, N. J., 1984, 75 pp.

Craig, P. D., Velocity profiles and surface roughness under breaking waves, *J. Geophys. Res.*, *101*, 1265–1277, 1996.

Craig, P. D., and M. L. Banner, Modelling wave-enhanced turbulence in the ocean surface layer, *J. Phys. Oceanogr.*, *24*, 2546–2559, 1994.

de Kok, J. M., A 3D finite difference model for the computation of near- and far-field transport of suspended matter near a river mouth, *Cont. Shelf Res.*, *12*, 625–642, 1992.

Deleersnijder, E., and K. G. Ruddick, A generalized vertical coordinate for 3D marine problems, *Bulletin de la Société Royale des Sciences de Liège*, *61*, 489–502, 1992.

Deleersnijder, E., J.-M. Beckers, J.-M. Campin, M. El Mohajir, T. Fichefet, and P. Luyten, Some mathematical problems associated with the development and use of marine models, in *The mathematics of models for climatology and environment*, edited by J. I. Diaz, vol. 48 of *NATO ASI Series*, pp. 41–86, Springer, Berlin, Heidelberg, 1997.

Delhez, E. J. M., M. Grégoire, J. C. J. Nihoul, and J.-M. Beckers, Dissection of the GHER turbulence closure scheme, *J. Mar. Sys.*, *21*, 379–397, 1999.

Dick, S., Gezeitenströmungen um Sylt. Numerische Untersuchungen zur halbtägigen Hauptmondtide (M_2), *Dt. Hydrogr. Z.*, *40*, 25–44, 1987.

Dick, S., and K. C. Soetje, Ein operationelles ölausbreitungsmodell für die Deutsche Bucht, *Tech. Rep. Dt. Hydrogr. Z., Erg.-H. A, Nr. 16*, Bundesamt für Seeschiffahrt und Hydrographie, 1990.

Duwe, K., Modellierung der Brackwasserdynamik eines Tideästuars am Beispiel der Unterelbe, Ph.D. thesis, Universität Hamburg, 1988, published in: Hydromod Publ. No. 1, Wedel, Hamburg.

Espelid, T. O., J. Berntsen, and K. Barthel, Conservation of energy for schemes applied to the propagation of shallow-water inertia-gravity waves in regions with varying depth, *Int. J. Numer. Meth. Engng*, *49*, 1521–1545, 2000.

Freeman, N. G., A. M. Hale, and M. B. Danard, A modified sigma equations' approach to the numerical modeling of Great Lakes hydrodynamics, *J. Geophys. Res.*, *77*, 1050–1060, 1972.

Gerdes, R., A primitive equation ocean circulation model using a general vertical coordinate transformation. 1. Description and testing of the model, *J. Geophys. Res.*, *98*, 14,683–14,701, 1993.

Goodman, J. B., and R. J. LeVeque, On the accuracy of stable schemes for 2D scalar conservation laws, *Math. Comp.*, *45*, 15–21, 1985.

Griffiths, R. W., and P. F. Linden, The stability of vortices in a rotating, stratified fluid, *J. Fluid Mech.*, *105*, 283–316, 1981.

Haidvogel, D. B., and A. Beckmann, *Numerical Ocean Circulation Modelling*, vol. 2 of *Series on Environmental Science and Management*, Imperial College Press, London, 1999.

Holt, J. T., and I. D. James, An s coordinate density evolving model of the northwest European continental shelf. 1, Model description and density structure, *J. Geophys. Res.*, *106*, 14,015–14,034, 2001.

Janssen, F., C. Schrum, and J. O. Backhaus, A climatological data set of temperature and salinity for the Baltic Sea and the North Sea, *Dt. Hydrogr. Z.*, *Suppl. 9*, 1–245, 1999.

Jerlov, N. G., *Optical oceanography*, Elsevier, 1968.

Kagan, B. A., *Ocean-atmosphere interaction and climate modelling*, Cambridge University Press, Cambridge, 1995.

Kantha, L. H., and C. A. Clayson, *Small-scale processes in geophysical fluid flows*, vol. 67 of *International Geophysics Series*, Academic Press, 2000a.

Kantha, L. H., and C. A. Clayson, *Numerical models of oceans and oceanic processes*, vol. 66 of *International Geophysics Series*, Academic Press, 2000b.

Kliem, N., and J. D. Pietrzak, On the pressure gradient error in sigma coordinate ocean models: A comparison with a laboratory experiment, *J. Geophys. Res.*, *104*, 29,781–29,800, 1999.

Kondo, J., Air-sea bulk transfer coefficients in diabatic conditions, *Bound. Layer Meteor.*, *9*, 91–112, 1975.

Krone, R. B., Flume studies of the transport of sediment in estuarial shoaling processes, *Tech. rep.*, Hydraulic Eng. Lab. US Army Corps of Eng., 1962.

Lander, J. W. M., P. A. Blokland, and J. M. de Kok, The three-dimensional shallow water model TRIWAQ with a flexible vertical grid definition, *Tech. Rep. RIKZ/OS-96.104x, SIMONA report 96-01*, National Institute for Coastal and Marine Management / RIKZ, The Hague, The Netherlands, 1994.

Large, W. G., J. C. McWilliams, and S. C. Doney, Oceanic vertical mixing : a review and a model with nonlocal boundary layer parameterisation, *Rev. Geophys.*, *32*, 363–403, 1994.

Launder, B. E., and D. B. Spalding, *Mathematical models of turbulence*, Academic Press, New York, 1972.

Launder, B. E., G. J. Reece, and W. Rodi, Progress in the development of a reynolds-stress turbulence closure, *J. Fluid Mech.*, *68*, 537–566, 1975.

Leonard, B. P., A stable and accurate convective modelling procedure based on quadratic upstream interpolation, *Comput. Meth. Appl. Mech. Eng.*, *19*, 59–98, 1979.

Leonard, B. P., The ULTIMATE conservative difference scheme applied to unsteady one-dimensional advection, *Comput. Meth. Appl. Mech. Eng.*, *88*, 17–74, 1991.

Leonard, B. P., M. K. MacVean, and A. P. Lock, The flux integral method for multidimensional convection and diffusion, *App. Math. Modelling*, *19*, 333–342, 1995.

LeVeque, R. J., *Numerical methods for conservation laws*, Birkhäuser, Basel, Boston, Berlin, 1992.

Luyten, P. J., E. Deleersnijder, J. Ozer, and K. G. Ruddick, Presentation of a family of turbulence closure models for stratified shallow water flows and preliminary application to the Rhine outflow region, *Cont. Shelf Res.*, *16*, 101–130, 1996.

Luyten, P. J., J. E. Jones, R. Proctor, A. Tabor, P. Tett, and K. Wild-Allen, COHERENS – A coupled hydrodynamical-ecological model for regional and shelf seas: User documentation, *Tech. rep.*, Management Unit of the Mathematical Models of the North Sea, Brussels, 1999, 914 pp.

Madala, R. V., and S. A. Piacsek, A semi-implicit numerical model for baroclinic oceans, *J. Computat. Phys.*, *23*, 167–178, 1977.

Martins, F., R. Neves, and P. Leitão, A three-dimensional hydrodynamic model with generic vertical coordinate, in *Hydroinformatics '98*, edited by V. Babovic and L. C. Larsen, pp. 1403–1410, Balkema, Rotterdam, 1998, Proceedings of the third International Conference on Hydroinformatics, Copenhagen, Denmark, 24-26 August 1998.

Martinsen, E. A., and H. Engedahl, Implementation and testing of a lateral boundary scheme as an open boundary condition in a barotropic ocean model, *Coastal Engineering*, *11*, 603–627, 1987.

Mathieu, P.-P., E. Deleersnijder, B. Cushman-Roisin, J.-M. Beckers, and K. Bolding, The role of topography in small well-mixed bays, with application to the lagoon of Mururoa, *Cont. Shelf Res.*, 2001, accepted for publication.

McCalpin, J. D., A comparison of second-order and fourth order pressure gradient algorithms in a σ-co-ordinate ocean model, *Int. J. Numer. Meth. Fluids*, pp. 361–383, 1994.

Mellor, G. L., and T. Yamada, A hierarchy of turbulence closure models for planetary boundary layers, *Journal of Atmospheric Sciences*, *31*, 1791–1806, 1974.

Mellor, G. L., and T. Yamada, Development of a turbulence closure model for geophysical fluid problems, *Rev. Geophys.*, *20*, 851–875, 1982.

Mellor, G. L., T. Ezer, and L.-Y. Oey, The pressure gradient conundrum of sigma coordinate ocean models, *Journal of Atmospheric and Oceanic Technology*, *11*, 1126–1134, 1994.

Patankar, S. V., *Numerical Heat Transfer and Fluid Flow*, McGraw-Hill, New York, 1980.

Paulson, C. A., and J. J. Simpson, Irradiance measurements in the upper ocean, *J. Phys. Oceanogr.*, *7*, 952–956, 1977.

Payne, R. E., Albedo of the sea surface, *Journal of Atmospheric Sciences*, *9*, 959–970, 1972.

Pedlosky, J., *Geophysical fluid mechanics*, 2. ed., Springer, New York, 1987.

Perels, P. A. J., and M. Karelse, A two-dimensional, laterally averaged model for salt intrusion in estuaries, *Tech. Rep. 262*, Waterloopkundig Laboratorium. Delft Hydraulics Laboratory, 1982.

Phillips, N. A., A coordinate system having some special advantages for numerical forecasting, *J. Meteorol.*, *14*, 184–185, 1957.

Pietrzak, J., The use of TVD limiters for forward-in-time upstream-biased advection schemes in ocean modeling, *Monthly Weather Review*, *126*, 812–830, 1998.

Pohlmann, T., Predicting the thermocline in a circulation model of the North Sea – Part I: Model description, calibration and verification, *Cont. Shelf Res.*, *16*, 131–146, 1996.

Ribberink, J., and A. Al-Salem, Time-dependent sediment transport phenomena in an oscillatory boundary-layer flow under sheet-flow conditions, *Tech. Rep. H840.20, Part IV*, Delft Hydraulics, Delft, 1992.

Rodi, W., Turbulence models and their application in hydraulics, *Tech. rep.*, Int. Assoc. for Hydraul. Res., Delft, The Netherlands, 1980.

Roe, P. L., Some contributions to the modeling of discontinuous flows, *Lect. Notes Appl. Math.*, *22*, 163–193, 1985.

Rosati, A., and K. Miyakoda, A general circulation model for upper ocean simulation, *J. Phys. Oceanogr.*, *18*, 1601–1626, 1988.

Samarskij, A. A., *Theorie der Differenzenverfahren*, Akademische Verlagsgesellschaft Geest and Portig, Leipzig, 1984.

Savioli, J., and P. Justesen, Sediment in oscillatory flows over a plane bed, *Journal of Hydraulic Research*, *35*, 177–190, 1997.

Schneggenburger, C., H. Günther, and W. Rosenthal, Spectral wave modelling with non-linear dissipation: validation and applications in a coastal tidal environment, *Coastal Engineering*, *41*, 201–235, 2000.

Schumann, U., and T. Gerz, Turbulent mixing in stably stratified shear flows, *J. Appl. Meteorol.*, *34*, 33–48, 1995.

Simpson, J. H., H. Burchard, N. R. Fisher, and T. P. Rippeth, Modelling the cycle of tidal dissipation in a region of tidal straining, *Cont. Shelf Res.*, 2001, accepted for publication.

Song, Y., A general pressure gradient formulation for ocean models. Part I: Scheme design and diagnostic analysis, *Monthly Weather Review*, *126*, 3213–3230, 1998.

Song, Y., and D. B. Haidvogel, A semi-implicit ocean circulation model using a generalised topography-following coordinate, *J. Computat. Phys.*, *115*, 228–244, 1994.

Stelling, G. S., and J. A. T. M. van Kester, On the approximation of horizontal gradients in sigma co-ordinates for bathymetry with steep bottom slopes, *Int. J. Numer. Meth. Fluids*, *18*, 915–935, 1994.

Stips, A., H. Burchard, K. Bolding, and W. Eifler, Measurements and modelling of convective turbulence in Lake Lago Maggiore, Italy, *Ocean Dynamics*, 2001, submitted.

Strang, G., On the construction and comparison of difference schemes, *SIAM J. Num. Anal.*, *5*, 506–517, 1968.

Tartinville, B., E. Deleersnijder, P. Lazure, R. Proctor, K. G. Ruddick, and R. E. Uittenbogaard, A coastal ocean model comparison study for a three-dimensional idealised test case, *App. Math. Modelling*, *22*, 165–182, 1998.

Umlauf, L., and H. Burchard, A generic length-scale equation for geophysical turbulence models, *J. Phys. Oceanogr.*, 2001, submitted.

van Leer, B., Toward the ultimate conservative difference scheme. V: A second order sequel to Godunov's method, *J. Computat. Phys.*, *32*, 101–136, 1979.

Wang, Y., Comparing different numerical treatments of advection terms for wind-induced circulations in Lake Constance, in *Continuum mechanics and applications in geophysics and the environment*, edited by B. Straughan, R. Greve, H. Ehrentraut, and Y. Wang, pp. 368–392, Springer, Heidelberg, Berlin, 2001.

Weiergang, J., and M. Jønsson (Eds.), *DYNOCS technical data report*, Danish Hydraulic Institute, Hørsholm, Denmark, 1996.

Zalezak, S. T., Fully multidimensional flux-corrected transport algorithms for fluids, *J. Computat. Phys.*, *31*, 335–362, 1979.

Zalezak, S. T., A preliminary comparison of modern shock-capturing schemes: linear advection, in *Advances in computer methods for partial differential equations*, edited by R. V. aand R. S. Stepleman, pp. 15–22, Publ. IMACS, 1987.